Solute Transport Characteristics in Heterogeneous Porous Media

倉澤，智樹

(Degree)
博士（農学）

(Date of Degree)
2022-03-25

(Date of Publication)
2023-03-01

(Resource Type)
doctoral thesis

(Report Number)
甲第8365号

(URL)
https://hdl.handle.net/20.500.14094/D1008365

Solute Transport Characteristics in Heterogeneous Porous Media

不均質多孔質媒体内における溶質輸送特性

倉澤 智樹
Tomoki KURASAWA
Graduate School of Agricultural Science
Kobe University

A thesis submitted for the degree of
Doctor of Philosophy in Agricultural Science

January 2022

Acknowledgements

Undertaking this PhD has been a truly life-changing and exciting experience that would not have been possible without the support and guidance from many people to whom I wish to express my sincere appreciation.

Without any doubt, I would like to first acknowledge my supervisor, Dr. Kazuya Inoue, for allowing me to join the Laboratory of Hydraulic Structures and Geoenvironmental Engineering and for providing me with support and insight. He taught me not only technical skills, but also personal skills. My research would not have been possible without him. I would also like to express my gratitude to my PhD committee, Professors Dr. Toshinori Kawabata and Dr. Haruya Tanakamaru, for the valuable time they spent reading my thesis and for their thoughtful questions, insightful ideas, and constructive comments. Special thanks go to Dr. Mariko Suzuki for providing technical assistance and encouragement and for showing me how to design and implement a field tracer test. I would like to extend my appreciation to Dr. Yutaka Sawada for providing valuable research advice for improving this thesis and for his continuous encouragement. I also owe special thanks to Dr. Tsutomu Tanaka, who cosupervised me during my bachelor's and master's projects and taught me the fundamentals of geotechnical engineering.

Next, I would like to thank Yoshitaro Takahashi, who worked with me on the laboratory-scale tracer experiments and was always there to support me. Of course, I would also like to thank all other colleagues, namely, Tatsuya Kitajima, Hiroki Takada, Eri Hiyoshi, Ayumi Kawada, Miki Suzuki, Hibiki Amo, Yosuke Kinoshita, Shin Nambu, Hirohito Saito, Mio Sakai, Masato Kita, Kento Koide, Itsuki Maeno, Tomofumi Oshita, Kazutaka Tomita, Kento Daimon, Tomoka Inaguchi, Maho Masumoto, Yuriko Takeki, Takahiro Tanigawa, Nagi Honda, Kentaro Ishimoto, Momoko Makino, Koki Matsumoto, Ai Takano, and Yui Takeuchi. Without the occasional coffee break and sparring session, I would not have completed this research.

I also wish to thank the people I had the pleasure to work with and learn from before returning to academia. My experience as an engineer helped me significantly

during my PhD and sparked my interest in research. And of course, this work would not have been possible without my friends with whom I shared many great times and who were always there to distract me.

I would also like to thank my parents, who have supported me throughout all stages of my life and provided me with nothing but endless support and care. Thanks to my two older brothers, Toshihiro and Eisuke, for always being there for me. Lastly and most importantly, I would like to express my deep appreciation to my beloved wife Tomoyo for her tremendous support, inspiration, and encouragement that helped me complete this thesis.

Contents

List of Figures

List of Tables

1 Introduction

Contents

1.1 Background

1.1.1 Groundwater and Contamination

Groundwater is the most abundant source of fresh water on earth and is crucial to life. It is stored in pores and cracks underground after percolating from the earth's surface or being trapped due to sedimentation or volcanic activity (Velis et al., 2017). Groundwater accounts for almost the total volume of usable freshwater resources. Specifically, the distribution of freshwater is as follows: groundwater, 95%; lakes, swamps, reservoirs, and river channels, 3.5%; and soil moisture, 1.5% (Freeze and Cherry, 1979). As one of the most important resources in the world, groundwater supplies the water necessary for agriculture, industry, animal husbandry, and human communities.

Approximately $2,500$ years ago, a number of methods for utilizing groundwater were invented in Persia, including a water management system called a *qanat*, which

was subsequently adopted in China, Arabia, and the Mediterranean coast and is known by local names such as *foggara*, *qareez*, and *falaj* (Stiros, 2006). Its function was to exploit an aquifer penetrated by a main well and supply water to villages in the desert at distances of 2 to 80 km. Groundwater has played an important role in the water supply for human activities not only in dry regions, but also in island and plateau regions, where there may an insufficient amount of freshwater in surface water, such as rivers and lakes. Based on recent estimates at the country level, the world's aggregated groundwater abstraction in 2010 was estimated to be approximately $1,000$ km^3 per year, of which approximately 67% was used for irrigation, 22% was used for domestic purposes, and 11% was used for industry. Two-thirds of this amount was abstracted in Asia, with India, China, Pakistan, Iran, and Bangladesh as the main consumers. The global groundwater abstraction rate has at least tripled over the last 50 years and continues to increase at an annual rate between 1% and 2% (Gun, 2012).

During recent decades, much of the focus of groundwater investigation in industrialized countries has shifted from problems of groundwater supply to considerations of groundwater quality. Love Canal in Niagara Falls, NY, USA was among the earliest and most significant hazardous water sites for soils and aquifers in the world. In the 1970s, chemical odors and other signs of contamination originating from the landfill were detected. Several state and federal actions led to the relocation of families living next to the canal between 1978 and 1980, and later to voluntary relocation farther from the canal, with the eventual establishment of an Emergency Declaration Area (Fletcher, 2002). The occurrence of groundwater contamination and the quality of groundwater have become major topics since the discovery of numerous hazardous-waste sites in the late 1970s, and the 1980s have been called the "hazardous-waste decade".

However, the problem of groundwater degradation is more difficult to overcome than the problem of surface water degradation. The U.S. Environmental Protection Agency (1977) reported that almost every known instance of aquifer contamination was discovered only after a water supply well was affected. Therefore, by the time subsurface pollution is identified, it is often too late to apply remedial measures. Moreover, river water has a turnover time on the order of two weeks, whereas groundwater moves much

more slowly (Freeze and Cherry, 1979). Therefore, long periods of groundwater flow are often required for pollutants to be flushed from contaminated aquifers.

1.1.2 Groundwater and Agriculture

It is well known that agriculture has direct and indirect effects on the rate and composition of groundwater recharge and aquifer biogeochemistry (Böhlke, 2002). In particular, studies have indicated that agricultural practices have resulted in nitrate (NO_3^-) contamination of groundwater, with high concentrations in shallow aquifers. The correlation between agricultural land use and high nitrate concentrations in groundwater has been documented since at least the 1970s (Hallberg, 1987; Hamilton and Helsel, 1995; Spalding and Exner, 1993). High nitrate concentrations in drinking water often induce birth defects and cancer, which have been the subject of epidemiological studies (Johnson et al., 2010). Nitrate concentrations above the maximum contaminant level (10 mgNL^{-1}) specified by the World Health Organization are relatively common in some regions, particularly in emerging and developing countries (Gu et al., 2013).

Seawater intrusion also poses a significant threat to the livelihood of populations in coastal zones who are dependent on freshwater extracted from aquifers near the sea or ocean. It is now widely recognized that the effects of climate change, such as sea-level rise and precipitation variations that alter recharge rates, are important climate factors that affect seawater intrusion in coastal aquifers. The preservation of groundwater quality in coastal areas has motivated the deployment of various engineering applications affecting the hydrodynamics of aquifers through physical alteration of the aquifers and/or groundwater recharge (Abdoulhalik and Ahmed, 2017). Among these engineering applications, artificial subsurface barriers (i.e., subsurface dams) have been constructed in Japan to preserve irrigation water and prevent the intrusion of seawater, particularly on small islands and in archipelagos (Luyun et al., 2009). There are currently more than 10 subsurface dams in Japan, which play an essential role in agricultural activities. However, physical changes in an aquifer due to the construction of dams can lead to groundwater quality degradation. This is due to the retention of contaminants in the storage area, which occurs because the barriers induces stagnant zones in the aquifer. For example, Yoshimoto et al.

(2013) reported that high nitrate concentrations (above 10 mgNL^{-1}) occurred in the storage area of a subsurface dam.

1.1.3 Solute Transport Models

While the problem of achieving acceptable surface water quality is generally focused on reducing known emissions of pollutants to surface water systems, the problem of achieving acceptable groundwater quality is to identify the areas and mechanisms by which pollutants enter groundwater systems and to develop reliable predictions of the transport of contaminants in these systems (Freeze and Cherry, 1979). In this thesis, we focus on the transport of dissolved contaminants. Solute transport in soil and groundwater is affected by a large number of physical, chemical, and microbial processes as well as the properties of the aquifer. Ignoring chemical and microbial processes, solute transport is generally described by the advection–dispersion equation (ADE) (Bear, 1972), which was the earliest transport model of contaminants in groundwater. For one-dimensional flow, the ADE is expressed as follows:

$$\frac{\partial C}{\partial t} = D\frac{\partial^2 C}{\partial x^2} - v\frac{\partial C}{\partial x}, \tag{1.1}$$

where C is the solute concentration, $D = \alpha v$ is the dispersion coefficient, α is the dispersivity, v is the average groundwater velocity, x is the distance, and t is the time. For laboratory columns packed with homogeneous soil, it is generally accepted that solute contaminants can be well described by the ADE (Harleman and Rumer, 1963; Klotz et al., 1980; Liang et al., 2018; Qian et al., 2015; Xu and Eckstein, 1997). The ADE is used to this day as the principal means of measuring and quantifying transport in groundwater.

However, there are several cases where the ADE fails to capture contaminant migration in the field. This is because in the natural subsurface, solid materials with different properties are unevenly distributed in various spatial patterns, resulting in anomalous transport. Therefore, alternative models, such as the mobile–immobile model (van Genuchten and Wierenga, 1977), convective lognormal transfer function model (Vanderborght et al., 1996; R. Zhang et al., 1994), spatial fractional ADE (Benson et al., 2000), and continuous-time random walk (Berkowitz et al., 2006), have been

proposed to represent solute transport in heterogeneous aquifers. Nevertheless, due to the simplicity of the ADE, it is still commonly used in many practical transport problems (Liang et al., 2018).

1.2 Research Objectives and Outline

As mentioned in Section 1.1, spatial variations in subsurface properties, such as hydraulic conductivity and porosity, have a profound impact on solute transport. However, accurately determining the relationship between solute transport and spatial heterogeneity remains a challenge. The goal of this PhD project is to improve the fundamental understanding of solute transport in heterogeneous aquifers and to quantify transport parameters, including dispersivity, groundwater flow velocity, and porosity. Figure 1.1 presents the structure and objectives of this thesis.

Chapter 2 presents laboratory-scale experiments for a simple aquifer model, namely, a step-function model, where the heterogeneity of hydraulic conductivity consists of a succession of two porous materials. In particular, this chapter focuses on how and to what extent a stratified structure controls the strength of solute dispersion and spreading. A quantitative visualization technique is employed to quantify and characterize the solute dispersion process.

Chapters 3 and 4 evaluate the effect of upscaling the hydraulic conductivity field on solute dispersion in porous media. Accurate modeling of solute transport is crucial to understand the behavior of dissolved contaminants in groundwater systems. However, numerical models cannot resolve all scales of spatial hydraulic conductivity fluctuations, as computational power and characterization techniques are limited. Therefore, a method that transfers small-scale information to the computational scale (i.e., a coarser scale), referred to as upscaling, is employed in practice. This technique leads to simplification of the physical problem and can affect solute transport. Chapter 3 presents a combined experimental and numerical investigation to examine the effect of upscaling on solute dispersion in stratified formations. In addition, Chapter 4 presents laboratory-scale experiments to evaluate the relationship between upscaling and solute dispersion for a two-dimensional randomly heterogeneous aquifer.

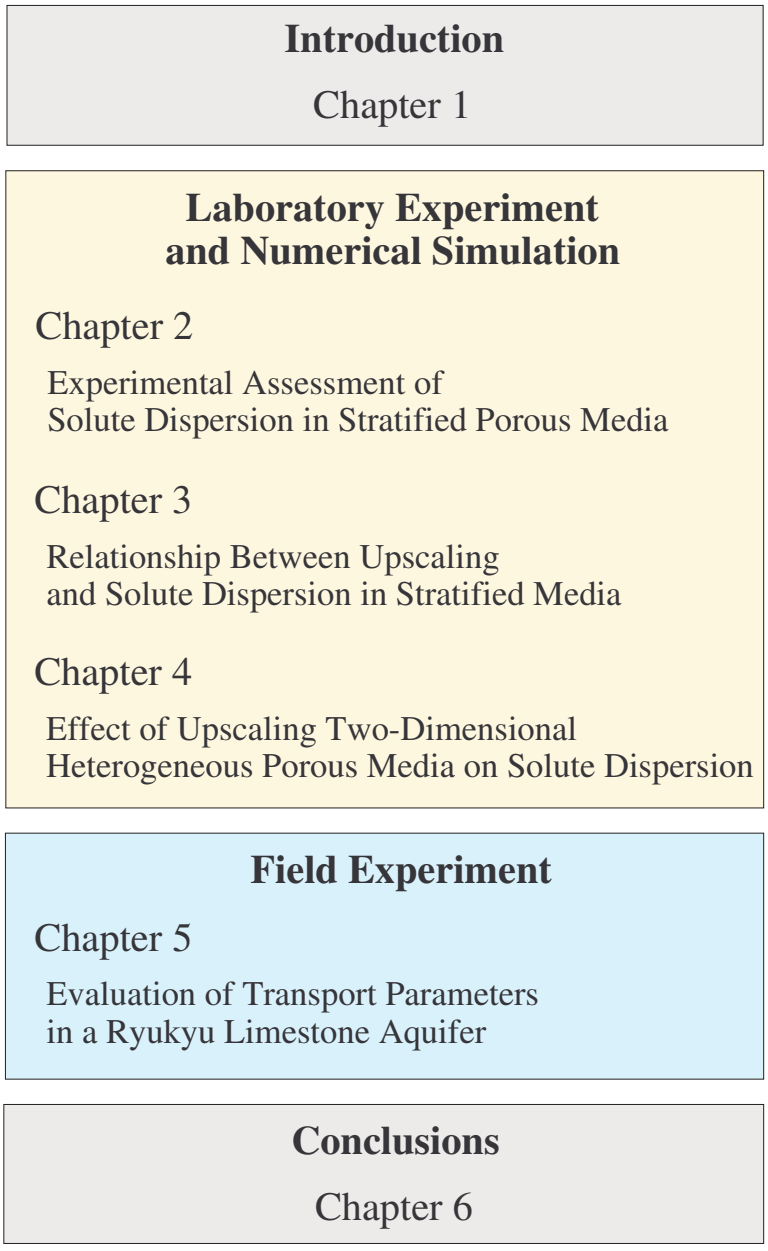

Figure 1.1: Thesis structure and objectives.

Chapter 5 presents single-borehole dilution tests (SBDTs), which are methods for evaluating transport parameters, such as groundwater velocity and dispersivity, using wells or boreholes based on tracer injection into the saturated zone and observation of the concentration over depth and time. In this chapter, we estimate the horizontal groundwater velocity and dispersivity of a Ryukyu limestone aquifer in Japan, where the construction of a subsurface dam is planned. As mentioned in Section 1.1, a previous study reported that high nitrate concentrations occurred in the storage area of a subsurface dam. Thus, it is important to determine the solute transport characteristics of aquifers. Moreover, we evaluate the porosity of the Ryukyu limestone aquifer, which is important to determine the water storage capacity of the subsurface dam. Chapter 6 summarizes the main achievements of this thesis and provides suggestions for future work.

2

Experimental Assessment of Solute Dispersion in Stratified Porous Media

Contents

2.1 Introduction

Natural soils and aquifers often possess complex spatial patterns of hydraulic conductivity (Nakagawa et al., 2012; Zinn et al., 2004), leading to dispersive mixing of solutes. Solute dispersion is a key factor in understanding the transport of solute contaminants in groundwater; therefore, it is important to quantify the effect of

a heterogeneous structure on the dispersion process. Studies using mathematical, numerical, geostatistical, and stochastic methods have investigated the relationship between a heterogeneous structure and dispersion parameters, such as the dispersivity and dispersion coefficient (Beaudoin and Dreuzy, 2013; Dagan, 1984; Fernàndez-Garcia and Gómez-Hernández, 2007; Gelhar and Axness, 1983; Zinn et al., 2004). In particular, solute dispersion in stratified porous media has been frequently studied (Bolster et al., 2011; Gelhar et al., 1979; Güven et al., 1984; Mercado, 1967; Zavala-Sanchez et al., 2009) because natural sandy aquifers often exhibit geological stratification characterized by a much larger horizontal than vertical correlation length. These studies provide the foundation for quantifying the dispersivity and dispersion coefficient in stratified media.

In contrast to the large number of theoretical and numerical studies, field tracer experiments are scarce, which may be due to the difficulty of conducting field tests on a routine basis. As an alternative, laboratory tracer experiments have been widely used to understand the influence of various factors on solute transport in porous media (Chao et al., 2000; Danquigny et al., 2004; Fernàndez-Garcia et al., 2002; Heidari and Li, 2014; Silliman and Simpson, 1987; Ye et al., 2015; C. Zhang et al., 2019). These experiments have an advantage in that the physical and chemical properties of the porous media are well defined. In several studies, laboratory experiments were coupled with image analysis techniques that made it possible to estimate the solute concentration in the test aquifer without the use of invasive instruments (Citarella et al., 2015; Jaeger et al., 2009; McNeil et al., 2006; Ursino et al., 2001; Zinn et al., 2004). A number of laboratory experiments on homogeneous two- and three-dimensional random hydraulic conductivity fields have also been conducted (Chao et al., 2000; Fernàndez-Garcia et al., 2002; Fernàndez-Garcia, Rajaram, et al., 2005; Inoue et al., 2016a; Levy and Berkowitz, 2003); however, laboratory experiments on stratified formations are much scarcer (Inoue et al., 2016b). Although Inoue et al. (2016b) investigated the scale dependence of longitudinal dispersivity in stratified porous formations and the relationship between the dispersivity and the degree of heterogeneity, they did not evaluate the effect of the stratified structure (i.e., the contrast between the layer thickness and hydraulic conductivity) on solute dispersion.

The objective of this chapter is to examine how a stratified structure, particularly the contrast between the layer thickness and hydraulic conductivity, affects solute dispersion. We consider one of the simplest models of a stratified formation, namely, a step-function model, where the heterogeneity consists of a succession of two porous materials in serial order. For this model, two-dimensional laboratory tracer experiments are conducted, and an image analysis technique is used to analyze the solute dispersion processes. Furthermore, because the behavior of the forward and backward tails of solute plumes is of particular importance due to their potential for groundwater contamination, we also present an approach to quantify the behavior of forward and backward plume tails.

2.2 Material and Methods

2.2.1 Experimental Apparatus

Laboratory experiments were conducted in a sandbox with internal dimensions of 200 cm × 80 cm × 3 cm (length × height × width). The design of the sandbox is illustrated in Figure 2.1. Constant head spill reservoirs connected to the upstream and downstream ends of the sandbox were used to control the flow through the outer boundaries of the sand pack. At the front side of the sandbox, a window with a 3-cm-thick glass pane allowed for visual observation. At the rear side of the sandbox, an acrylic plate enabled the introduction of 10 pressure measurement ports and eight solute injection ports (labeled a–h in Figure 2.1). The upstream and downstream ends of the sandbox were separated from the porous medium by thin meshes with a hydraulic conductivity larger than that of the porous materials.

2.2.2 Porous Media

In the experiments, three different types of sorted silica sand (S1, S2, and S3) with different grain sizes were employed. The hydraulic conductivity of each type of sand was determined by the following steps. First, a one-dimensional column was packed with each type of sand. Under steady-state conditions, the flow rate and hydraulic gradient were measured, and Darcy's law was used to calculate the hydraulic conductivity. The relevant properties of the different types of sand are provided in Table 2.1.

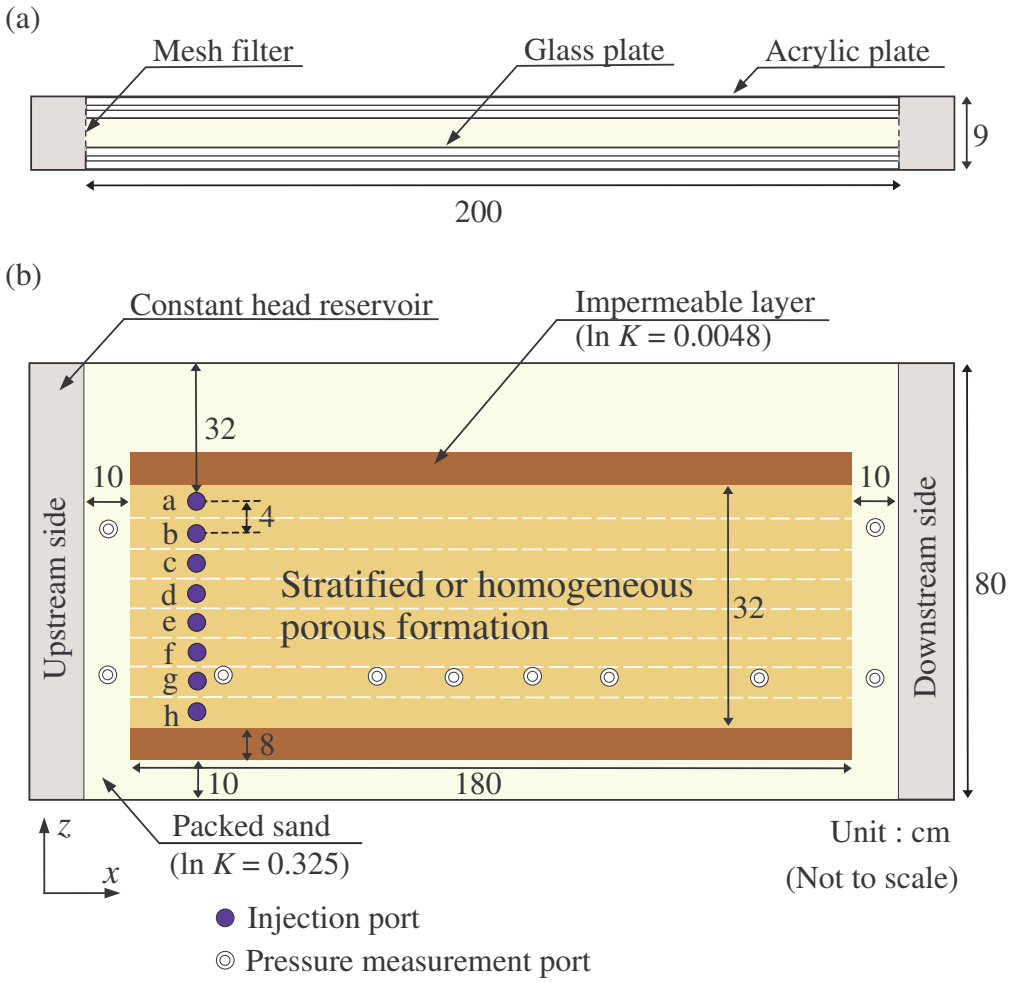

Figure 2.1: Design of the sandbox. (a) Top view and (b) front view displaying the injection and pressure measurement ports. ln K denotes the natural logarithm of hydraulic conductivity.

Table 2.1: Properties of test sands.

Sand type	Hydraulic conductivity (cm/s)	Porosity (–)
S1	0.0341	0.437
S2	0.0996	0.437
S3	0.195	0.437

Table 2.2: Summary of experimental cases.

Schematic[a]	Cases	Thickness of layers (cm)	K contrast C (–)	Heterogeneity $\sigma^2_{\ln K}$ (–)
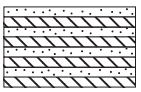	A-4	4	1.96	0.113
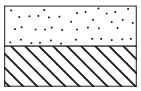	A-16	16	1.96	0.113
	B-4	4	5.72	0.762

[a] S1 (K = 0.0341 cm/s)
S2 (K = 0.0996 cm/s)
S3 (K = 0.195 cm/s)

Three stratified structures were constructed in the sandbox, referred to as cases A-4, A-16, and B-4 (Table 2.2). These stratified cases are step-function models. As illustrated in Table 2.2, A-4 had eight 4-cm-thick layers, including four high-conductivity layers (composed of S3 sand) and four low-conductivity layers (composed of S2 sand), while A-16 had two 16-cm-thick layers, including one high-conductivity layer (S3) and one low-conductivity layer (S2). B-4 had eight 4-cm-thick layers, including four high-conductivity layers (S3) and four low-conductivity layers (S1). It should be noted that although A-4 and B-4 had the same thickness and number of layers, there were differences in the hydraulic conductivity contrast and heterogeneity of these two cases. A-4 and A-16 had the same hydraulic conductivity contrast and heterogeneity; however, there were differences in the thickness and number of layers. Thus, mass transfer between high- and low-conductivity layers due to transverse dispersion occurred less in A-16 than in A-4. The hydraulic conductivity contrast C and heterogeneity $\sigma^2_{\ln K}$ (variance of $\ln K$) were calculated by

$$C = \frac{K_h}{K_l}, \tag{2.1}$$

$$\sigma^2_{\ln K} = \frac{1}{n}\left(\sum_{i=1}^{n}(\ln K_i)^2 - n(\ln M)^2\right), \tag{2.2}$$

where K_h and K_l are the hydraulic conductivities of the high- and low-conductivity layers of a stratified medium, n is the number of layers, K_i is the hydraulic conductivity of layer i, and M is the geometric mean of the hydraulic conductivity.

The hydraulic conductivity contrast and the heterogeneity of each case are also presented in Table 2.2. Variations in hydraulic conductivity differ significantly in different natural aquifers ($\sigma^2_{\ln K} = 0.14 - 4.5$) (Boggs et al., 1992; Mackay et al., 1986; Sudicky, 1986). In this study, the $\sigma^2_{\ln K}$ values of the stratified formations were relatively small ($\sigma^2_{\ln K} = 0.113 - 0.762$).

To verify the reliability of the experimental device, experiments on the homogeneous packing of S3 were also conducted using the sandbox illustrated in Figure 2.1 and a one-dimensional column that had a 5-cm internal diameter and a length $L = 30$ cm, and the longitudinal dispersivities obtained from these devices were compared.

Sand packing was performed under saturated conditions, with the sand being poured through at least 2 cm of water to avoid air entrapment. The sand was packed in 2-cm or 4-cm layers using narrow metal dividers to establish sharp contacts between regions of different sand. The dividers were gradually removed as the packing proceeded.

2.2.3 Experimental Procedure and Image Acquisition

The dye Brilliant Blue FCF, which is a safe, nontoxic compound (Flury and Flühler, 1994), was chosen as a tracer for image analysis. After establishing steady-state flow conditions, a dilute Brilliant Blue FCF solution with a concentration of 0.2 mg/L was injected. The eight injection ports (a–h in Figure 2.1) along the transverse line were used to test the spatial heterogeneity of the entire stratified medium. A concentration of 0.2 mg/L was chosen so as to minimize the effect of density while providing a sufficiently broad range over which meaningful concentration measurements could be performed. For all cases (i.e., A-4, A-16, and B-4), light sources and a digital camera were placed in front of the sandbox filled with silica sand. During the experiments, the digital camera captured a series of red, green, and blue (RGB) images of the solute plume (Figure 2.2(a)). All images were 800 × 600 pixels (length × height) with a resolution of approximately 4 pixels/cm.

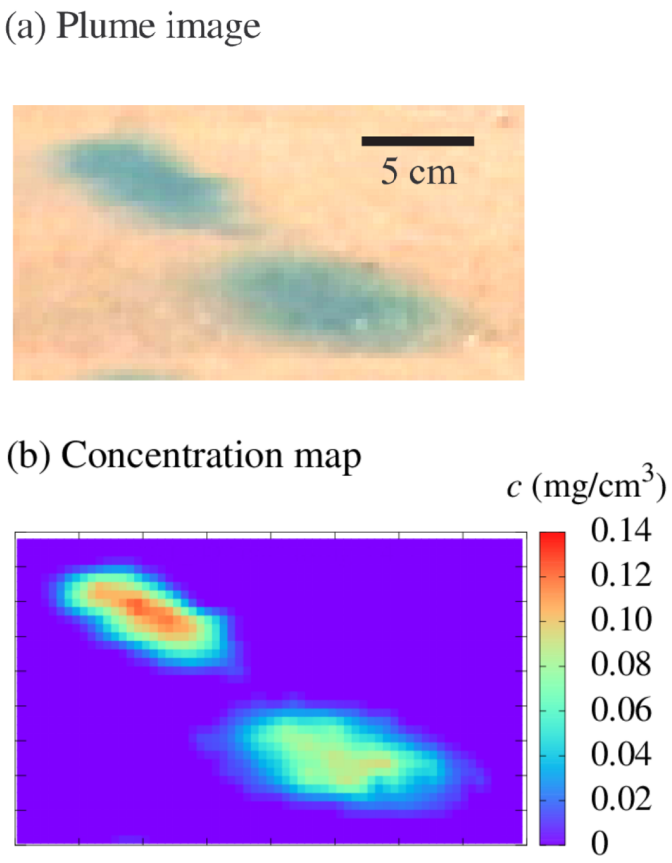

Figure 2.2: Snapshot of solute plume. (a) Plume image and (b) concentration map.

2.2.4 Image Analysis

In each image, each pixel displays a color based on its RGB combination. Thus, it is possible to divide the three color channels to perform a transformation on each image, resulting in three different grayscale images. In this manner, each pixel can assume integer values from 0 (black) to 255 (white), thereby enabling measurement of the pixel intensity of the entire image in each channel. In this study, the three color channels were separated, and only red values were taken into consideration. The dye concentration was correlated with the red color intensity using a calibration procedure consisting of the following steps: (i) injecting a solute plume at a known concentration in the porous medium; (ii) acquiring an image; (iii) restarting from step (i) with a new solution concentration. This procedure was performed for different concentrations to obtain adequate calibration curves. The red value of the dye is related to the size of the sand grain and the lighting conditions as well as the dye concentration.

Therefore, for each experimental case, each sand type was characterized by a unique calibration curve, as illustrated in Figure 2.3, and these curves were used to determine the solute concentration maps (Figure 2.2(b)).

2.2.5 Evaluation of Dispersivities from Spatial Moments

Spatial moment analysis has been widely used to quantify solute spreading in transport problems (Adams and Gelhar, 1992; Freyberg, 1986; Inoue et al., 2016b). In two-dimensional experiments, the ijth spatial moment of a concentration distribution, M_{ij}, is defined by

$$M_{ij}(t) = \int_{-\infty}^{\infty}\int_{-\infty}^{\infty} c(x,z,t)x^i z^j dxdz, \tag{2.3}$$

where $c(x,z,t)$ is the solute concentration, t is the time, x and z are spatial Cartesian coordinates (horizontal and vertical, respectively), and i and j are nonnegative integers. The centers of mass of the solute plume in the x- and z-directions are calculated by

$$x_G(t) = \frac{M_{10}(t)}{M_{00}(t)}, \tag{2.4}$$

$$z_G(t) = \frac{M_{01}(t)}{M_{00}(t)}, \tag{2.5}$$

where x_G and z_G are the centers of mass of the tracer plume in the x- and z-directions, respectively. Using equations (2.4) and (2.5), the second moment about the center of mass defines a spatial covariance tensor (Freyberg, 1986; Inoue et al., 2016b):

$$\begin{aligned}\sigma_{ij}(t) &= \begin{pmatrix}\sigma_{xx}(t) & \sigma_{xz}(t)\\ \sigma_{zx}(t) & \sigma_{zz}(t)\end{pmatrix}\\ &= \begin{pmatrix}\dfrac{M_{20}(t)}{M_{00}(t)} - (x_G(t))^2 & \dfrac{M_{11}(t)}{M_{00}(t)} - x_G(t)z_G(t)\\ \dfrac{M_{11}(t)}{M_{00}(t)} - z_G(t)x_G(t) & \dfrac{M_{02}(t)}{M_{00}(t)} - (z_G(t))^2\end{pmatrix},\end{aligned} \tag{2.6}$$

where σ_{ij} is the second moment about the center of mass. The longitudinal and transverse macrodispersivities are defined as (Bear, 1972)

$$A_L(\xi_c,t) = \frac{1}{2}\frac{\sigma_{xx}(t)}{\xi_c(t)}, \tag{2.7}$$

$$A_T(\xi_c,t) = \frac{1}{2}\frac{\sigma_{zz}(t)}{\xi_c(t)}, \tag{2.8}$$

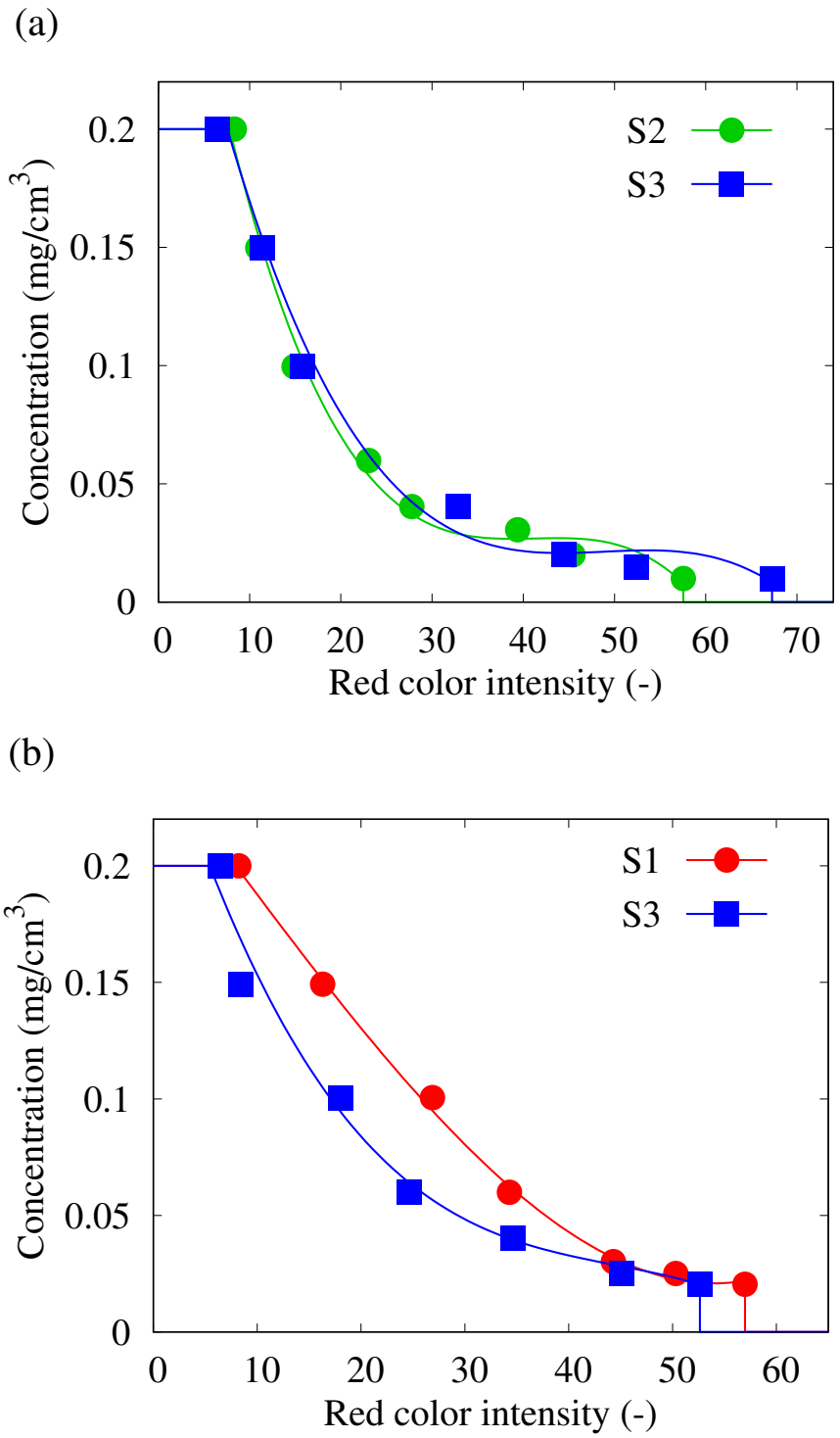

Figure 2.3: Calibration curves for cases (a) A-16 and (b) B-4. Case A-16 has two layers composed of S3 and S2 sands, whereas case B-4 has eight layers composed of S3 and S1 sands.

where A_L and A_T are the longitudinal and transverse macrodispersivities, respectively, and ξ_c is the travel distance of the center of mass of the tracer plume in the mean flow direction (x-direction).

2.3 Results and Discussion

2.3.1 Longitudinal Macrodispersivity

The longitudinal dispersivities for homogeneous packing (S3) of the sandbox (see Figure 2.1) were in the range 0.075–0.13 cm. This result is in good agreement with the value ($A_L = 0.072$ cm) for the one-dimensional column, indicating the reliability of the experimental device. For the stratified cases, the longitudinal macrodispersivity as a function of the travel distance of the center of mass is presented in Figure 2.4(a) together with the analytical solution provided by Mercado (1967). The analysis of horizontal displacement through a stratified aquifer by Mercado (1967) illustrates the effect of variation of the hydraulic conductivity in the vertical direction. Mercado's analytical solution of the longitudinal macrodispersivity is given as (Gelhar et al., 1979; Mercado, 1967)

$$A_L = \frac{1}{2}\left(\frac{\sigma_K}{\bar{K}}\right)\bar{x}, \tag{2.9}$$

where σ_K is the standard deviation of the hydraulic conductivity, $\bar{K}$ is the average hydraulic conductivity, and $\bar{x}$ is the mean travel distance in the x-direction. Note that the dispersivity calculated by Mercado's solution is proportional to the variance of the hydraulic conductivity and increases indefinitely with travel distance. Cases A-4 and A-16 had the same longitudinal dispersivity computed by equation (2.9) because they had the same values of σ_K and $\bar{K}$.

As seen in Figure 2.4(a), the longitudinal macrodispersivity increased with the travel distance in the three stratified cases. This is consistent with previous studies (Gelhar et al., 1992), which reported that longitudinal macrodispersivities in heterogeneous porous media exhibit scale-dependent behavior. The scale dependence of A_L also provides evidence that the scale dependence of longitudinal macrodispersivity can be observed under two-dimensional controlled laboratory conditions. Cases A-4 and A-16 had the same hydraulic conductivity contrast and heterogeneity; however, the

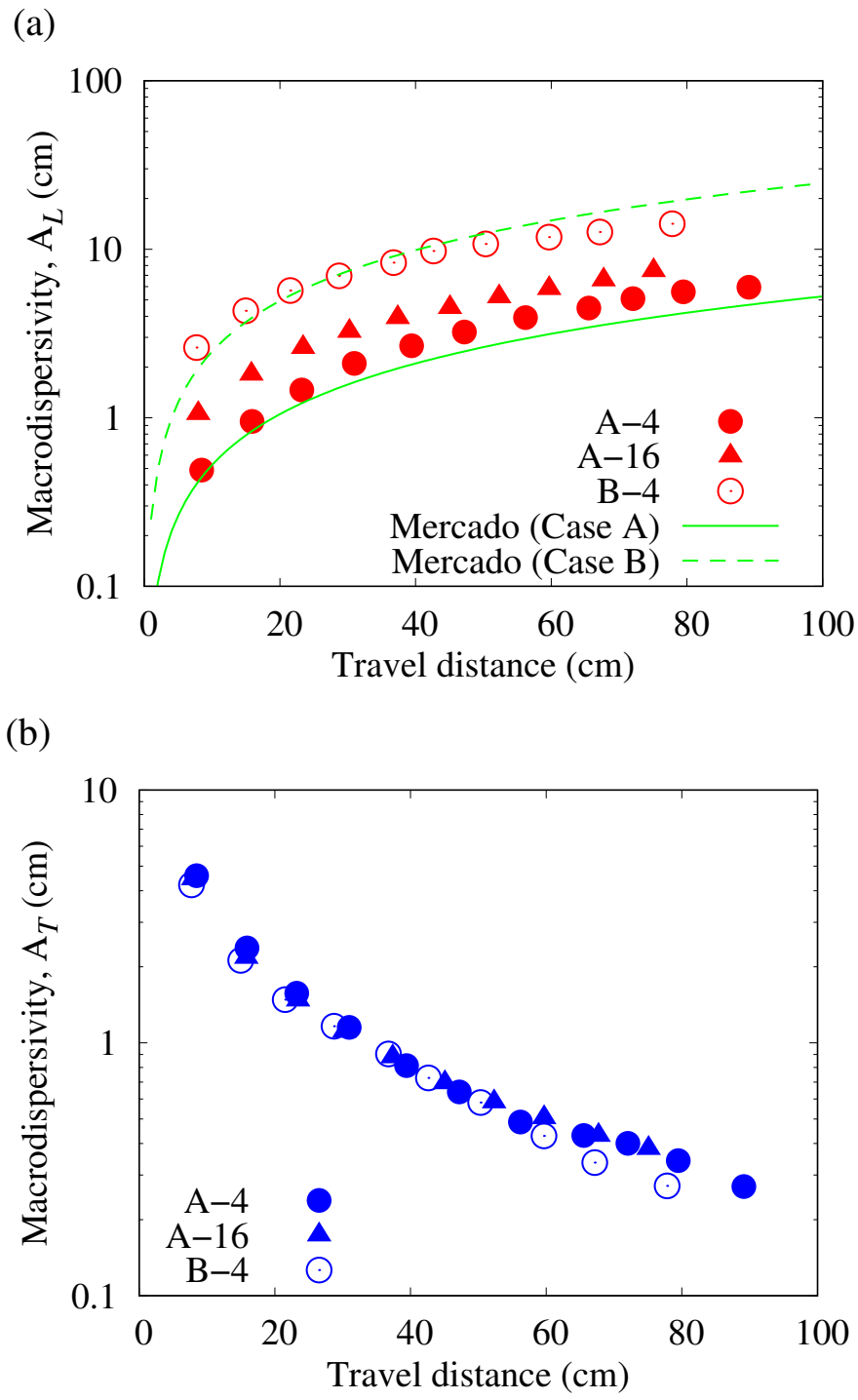

Figure 2.4: (a) Longitudinal and (b) transverse dispersivities as a function of the travel distance of the center of solute mass. Solid symbols represent cases A-4 (circles) and A-16 (triangles), while open symbols represent case B-4 (circles). Solid and dashed lines correspond to the dispersivity calculated by equation (2.9) for cases A and B, respectively.

longitudinal macrodispersivity estimates for A-16 were slightly higher than those for A-4. This suggests that the mass transfer driven by transverse dispersion between high- and low-conductivity layers was larger for A-4 than for A-16 due to the relatively small layer thickness, leading to relatively small longitudinal (x-direction) spreading of the tracer plume. Pickens and Grisak (1981) reached a similar conclusion from their review of previous field tests and from experimental longitudinal macrodispersivity results. Although cases A-4 and B-4 had the same layer thickness, their longitudinal macrodispersivities exhibited different scale-dependent behavior. This discrepancy can be attributed to the difference in heterogeneity (i.e., hydraulic conductivity contrast) in the two cases.

As illustrated in Figure 2.4(a), the longitudinal macrodispersivities are in reasonable agreement with the analytical solution for all stratified cases, which demonstrates the validity of our experiment. As mentioned above, the dispersivity estimated from Mercado's solution increases indefinitely with travel distance, whereas longitudinal macrodispersivity generally approaches a constant value at large distances (Fernàndez-Garcia, Illangasekare, et al., 2005). Although the experimental dispersivities A_L agree with Mercado's solution at the travel distance in our experiments, they may diverge at relatively large scales. Further experimental studies for larger scales are thus necessary to evaluate the practicability of Mercado's analytical solution.

2.3.2 Transverse Macrodispersivity

Figure 2.4(b) displays the transverse macrodispersivity as a function of travel distance. For all cases, this parameter decreases with increasing travel distance. To explain this behavior, Figure 2.5 displays σ_{zz} as a function of travel distance.

For all cases, σ_{zz} remained approximately constant. This is because σ_{zz}, which is the mean square displacement in the transverse direction, is dependent on the initial source size in the transverse direction (i.e., eight-point injection). In the stratified cases, the hydraulic conductivity of the porous media differed only in the vertical direction (i.e., z-direction) and did not significantly change the solute distribution in the z-direction. As a result, the behavior of σ_{zz} led to the aforementioned behavior of A_T, which was computed by equation (2.8).

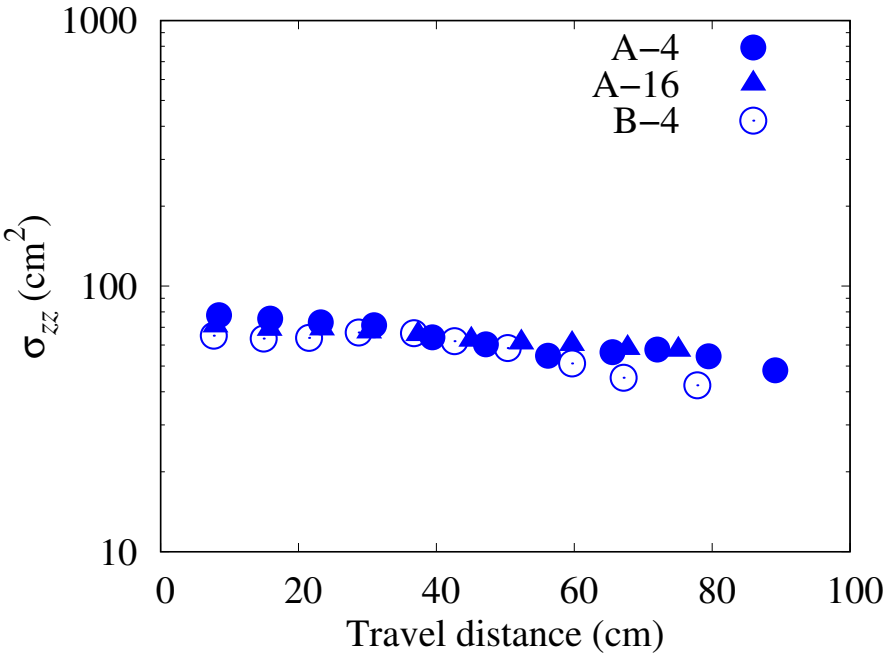

Figure 2.5: Mean square displacement in the transverse direction, σ_{zz}, as a function of the travel distance of the center of mass for cases A-4, A16, and B-4.

2.3.3 Comparison of Dispersivities Estimated in This Study and Earlier Works

To place this study in the context of other research and understand the influence of various factors (i.e., heterogeneity, scale, flow configuration, and spatial variability of the hydraulic conductivity) on the dispersivity, Table 2.3 presents a summary of the dispersivities and factors in this study and earlier laboratory-scale experiments in heterogeneous porous media. In this study, the heterogeneity values are relatively low, while the scale (i.e., travel distance) values are in the middle of the range. Compared with Inoue et al. (2016b), the A_L values in our study are larger overall, which is mostly due to the larger travel distances. Moreover, for similar heterogeneity values and scales, the A_L values of stratified porous media tend to be larger than those of randomly heterogeneous porous media. This suggests that if both the heterogeneity and scale for stratified and randomly heterogeneous porous media are similar, the longitudinal macrodispersivity is larger in stratified media than in randomly heterogeneous porous media.

Table 2.3: Summary of longitudinal and transverse dispersivities obtained from laboratory-scale tracer experiments in heterogeneous porous media.

Longitudinal macrodispersivity A_L (cm)	Transverse macrodispersivity A_T (cm)	Heterogeneity $\sigma^2_{\ln K}$ $(-)$	Scale[a] (cm)	Flow	Spatial variability of K	Reference
6.52–14.2	0.270–0.382	0.113–0.762	75.1–89.1	Uniform	Stratified	This study
0.187–0.594	—	1.81	25.4–43.2	Radial	2D random	Chao et al. (2000)
12	—	1.81	219.6	Uniform	2D random	Chao et al. (2000)
0.14–6.76	—	1.47	21–100	Radial	2D random	Fernàndez-Garcia et al. (2002)
0.92–6.4	0.063–1.4	0.36–3.6	26.5–47.8	Uniform	Stratified	Inoue et al. (2016b)
4.6	0.019	0.24	380	Uniform	2D random	McNeil et al. (2006)

a: Scale represents the travel distance of the solute plume.

Consistent with previous studies (Gelhar et al., 1992), in all studies in Table 2.3, the transverse macrodispersivity is 1–2 orders of magnitude smaller than the longitudinal macrodispersivity. Table 2.3 also demonstrates that the transverse macrodispersivity varies over several orders of magnitude. Compared with the longitudinal macrodispersivity data, the transverse macrodispersivity data are more limited and do not reveal any significant trends (Gelhar et al., 1992). In particular, and as mentioned previously, although transverse macrodispersivity estimates depend on the initial source size, the overall effect of the source size on the transverse macrodispersivity is not yet clear based on the studies summarized in Table 2.3. Thus, the effect of the source size on the transverse macrodispersivity requires further clarification.

2.3.4 Forward and Backward Tails

The behavior of the forward and backward tails of a solute plume is of particular importance because of the potential for groundwater contamination. To quantify this behavior, we defined the travel distances x_{05} and x_{95} corresponding to the 5th and 95th percentiles, respectively, of the cumulative concentrations in the x-direction. Figure 2.6 illustrates x_{05} and x_{95}, which represent the travel distances of the fastest (forward) and slowest (backward) portions of a tracer plume. In addition, Figure 2.7 displays x_{05} and x_{95} as a function of x_G. Figure 2.7 indicates that the distance between x_{05} and x_{95} increased with centroid position x_G in the three stratified cases. To further quantify this behavior, x_{05-95}, which is the distance between x_{05} and x_{95}, was calculated as follows:

$$x_{05-95}(t) = |x_{05} - x_{95}|. \tag{2.10}$$

Figure 2.8 displays x_{05-95} as a function of displacement distance and demonstrates that x_{05-95} increased linearly with travel distance. This indicates that for step-function models, forward and backward tails spread out linearly in the longitudinal direction.

2.4 Conclusions

The purpose of the experiments described in this chapter was to evaluate the effect of a stratified structure on solute dispersion. Laboratory-scale tracer experiments were conducted for three stratified porous media, where the heterogeneity consisted

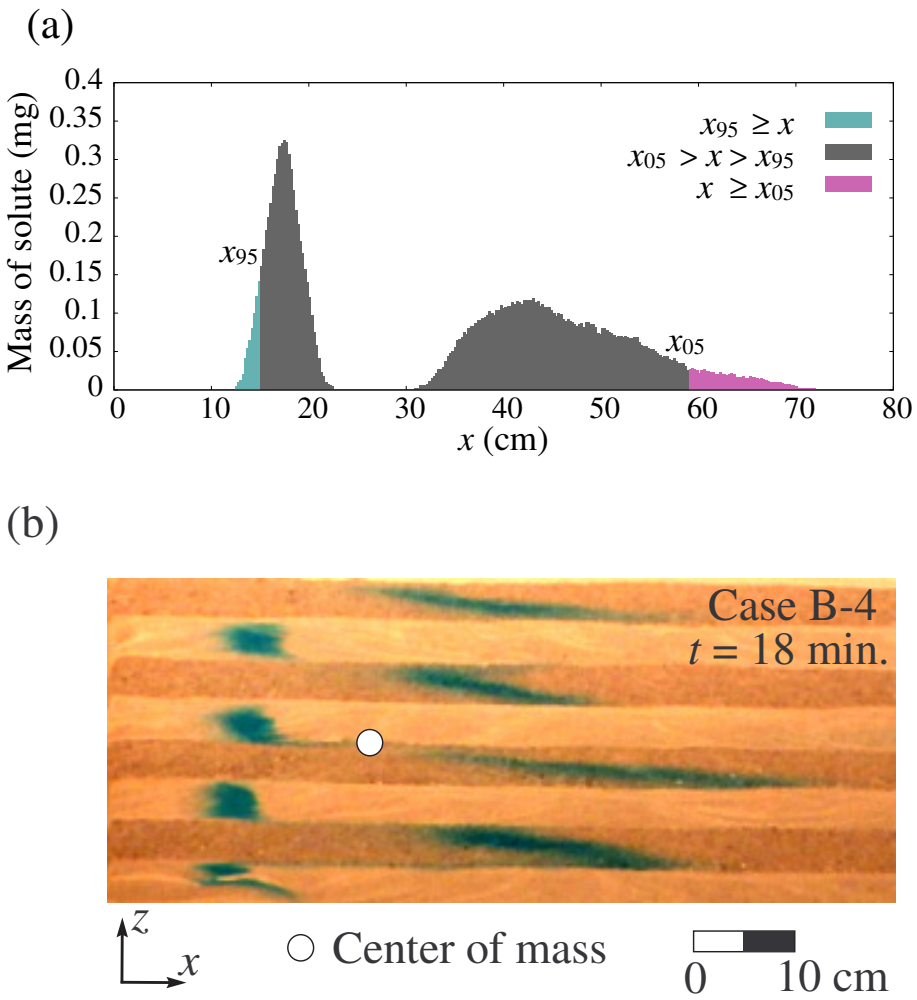

Figure 2.6: Illustration of forward and backward tails. (a) Example of the concentration profiles of a solute plume in the x-direction; (b) snapshot of the solute distribution. x_{05} and x_{95} are the travel distances corresponding to the 5th and 95th percentiles, respectively, of the cumulative concentrations in the x-direction.

of a succession of two porous materials in serial order (i.e., step-function model). An image analysis technique was used to analyze the solute dispersion processes and the behavior of the forward and backward tails. The main conclusions of these experiments are summarized as follows:

1. The longitudinal macrodispersivity increased with travel distance in the stratified porous media. This result provides evidence that the scale dependence of longitudinal macrodispersivity in heterogeneous porous media can be observed in a two-dimensional laboratory sandbox.

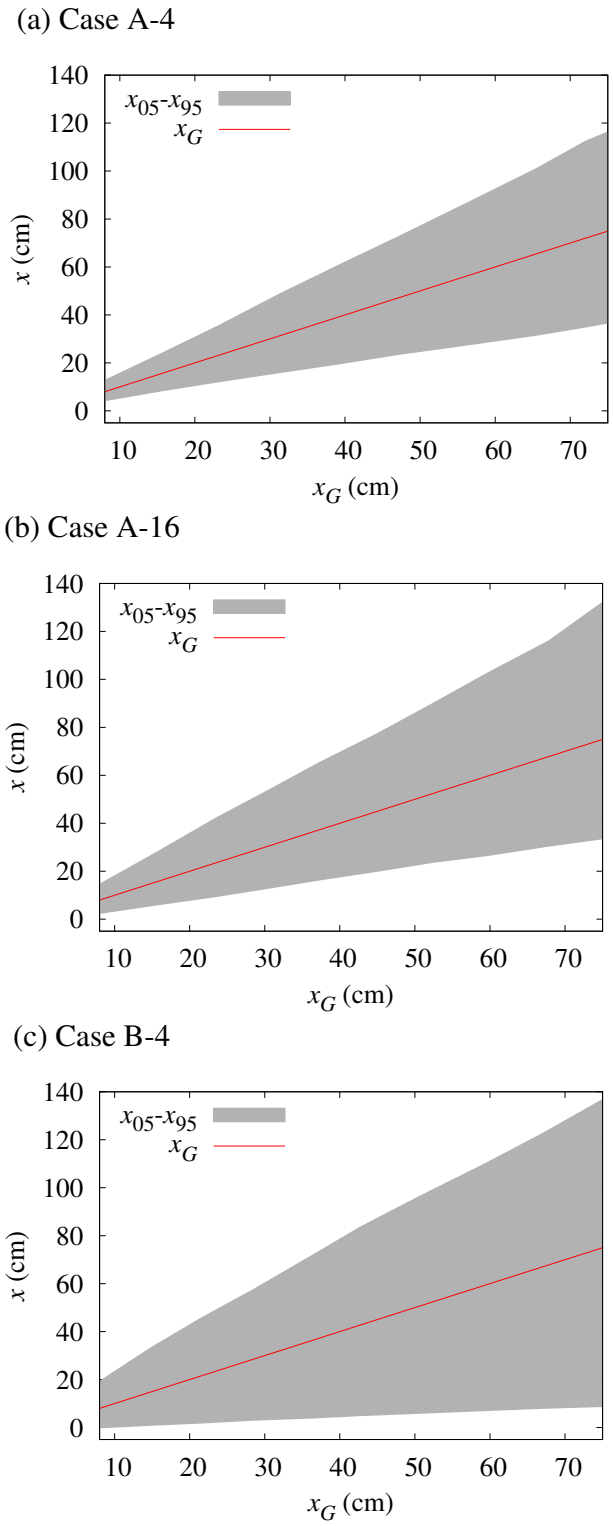

Figure 2.7: x_{05} and x_{95} as a function of x_G for cases (a) A-4, (b) A-16, and (c) B-4. x_{05} and x_{95} are the travel distances corresponding to the 5th and 95th percentiles, respectively, of the cumulative concentrations in the x-direction. The red lines represent the travel distance of the center of mass.

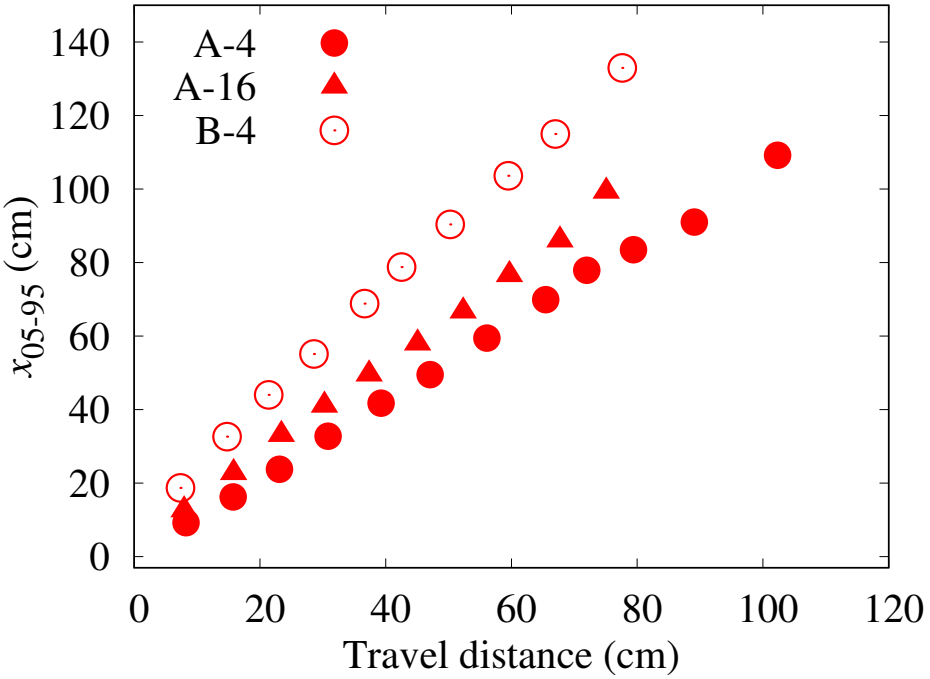

Figure 2.8: Distance between x_{05} and x_{95} versus the travel distance of the center of mass. x_{05} and x_{95} correspond to the 5th and 95th percentiles, respectively, of the cumulative concentrations.

2. The longitudinal macrodispersivity estimates were in reasonable agreement with the analytical solution for stratified porous media, demonstrating the validity of our experiments.

3. For all stratified cases, the transverse macrodispersivity exhibited a similar decreasing trend with travel distance. This is because the transverse macrodispersivity depends on the initial source size in the transverse direction.

4. The summary of longitudinal and transverse dispersivities estimated from this study and previous studies indicates that when both the heterogeneity and scale for stratified and randomly heterogeneous porous media are similar, the longitudinal dispersivity is larger in stratified media than in randomly heterogeneous media.

5. We defined the travel distances x_{05} and x_{95} corresponding to the 5th and 95th percentiles of the cumulative concentrations in the longitudinal direction, which reflected the travel distances of the fastest and slowest portions of a tracer plume,

respectively. We found that in the step-function models, forward and backward tails spread out linearly in the longitudinal direction.

3

Relationship Between Upscaling and Solute Dispersion in Stratified Media

Contents

3.1 Introduction

Modeling the transport (i.e., advection and dispersion) of dissolved contaminants in groundwater is necessary to facilitate geoenvironmental risk evaluation as well as management and remediation. At the field scale, aquifer properties, including the hydraulic conductivity, vary by many orders of magnitude across multiple length scales. It is well known that spatial fluctuations of the hydraulic conductivity (due to geological heterogeneity) have an important role in the spreading of a solute plume (Beaudoin and Dreuzy, 2013; Fiori et al., 2010; Inoue et al., 2016a). Thus, an accurate description of the hydraulic conductivity distribution is crucial for modeling transport in groundwater. However, numerical models generally cannot resolve all scales of spatial fluctuations (Dentz et al., 2011). This is mainly due to limitations in computational power and characterization techniques. Therefore, it is necessary to convert detailed information to a coarser scale that is better suited for numerical modeling. For this purpose, upscaling, which is a method of transferring small-scale information to the computational scale (i.e., a coarser scale), is used in practice.

Upscaling flow and solute transport in heterogeneous porous media has been studied for several decades. However, in contrast to the numerous studies on upscaling flow (Desbarats, 1992; Indelman and Dagan, 1993; Jensen, 1991; Sánchez-Vila et al., 1995; Wen and Gómez-Hernández, 1996), studies on upscaling solute transport are scarce. Several studies reported that the smoothing of the velocity field due to upscaling induced a loss in the spreading of the solute plume (Dagan, 1994; Fernàndez-Garcia and Gómez-Hernández, 2007). However, Inoue et al. (2011) reported that in stratified porous media, upscaling of the hydraulic conductivity distribution had no effect on the strength of the dispersion process. Therefore, the impact of upscaling the hydraulic conductivity on solute dispersion remains unclear.

The objective of this chapter is to understand the relationship between solute dispersion and the upscaling of stratified media. The investigation was performed using a combination of a laboratory experiment and numerical simulations. The experimental setup focused on reproducing a naturally stratified formation that mimics the physical heterogeneity of real aquifers known in the literature (Uffink, 1990). First, we conducted a solute transport experiment in the stratified formation, and the experimental data

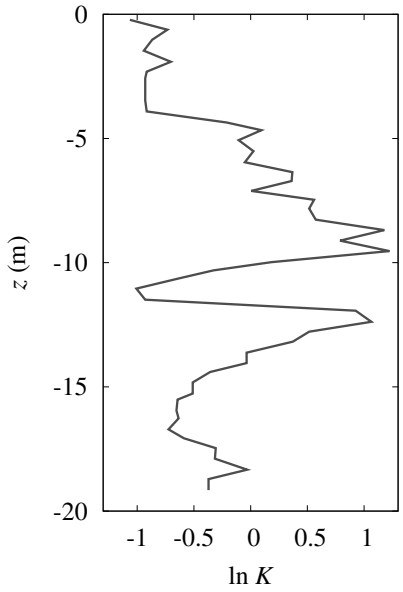

Figure 3.1: Vertical variation of the hydraulic conductivity reported by Uffink (1990). K denotes hydraulic conductivity (m/day)

.

were utilized to validate a numerical model. To evaluate the effect of upscaling, we then performed numerical simulations of solute transport in the upscaled stratified models.

3.2 Stratified Porous Model

3.2.1 Original Model

The target study site was located in The Hague, the Netherlands, where a tracer test was conducted in a confined aquifer (Uffink, 1990). The confined aquifer had a total thickness of approximately 20 m and consisted of sands of several geological formations. The vertical variation of hydraulic conductivity reported by Uffink (1990) is presented in Figure 3.1. We assumed that the aquifer was perfectly stratified.

To reproduce this aquifer in a laboratory-scale experimental tank, modification of the physical model illustrated in Figure 3.1 was performed in the following steps:

1. The vertical scale was set to approximately 1/29; thus, the modified aquifer had a total thickness of 70 cm without changing the vertical variation of $\ln K$.

2. In Figure 3.1, $\ln K$ ranges from 1 to -1. To conduct the experiment within the limits of validity of Darcy's law, we reduced the average of $\ln K$ by approximately

-2.

3. In the experiment, the test aquifer was constructed from 13 well-characterized silica sands. Because only 13 silica sands were used in the aquifer, the reduced $\ln K$ values were binned into 13 classes corresponding to the sands. The layer thickness was set to 2 cm, and the number of layers was 35.

Figure 3.2(a) presents the modified stratified model, hereafter referred to as the Reference field. The origin of the z-axis was set to the bottom of the flow tank as explained below, resulting in the bottom of the Reference field being equal to $z = 5$. We verified the accuracy of the numerical simulation by comparing the computed degree of dispersion to the experimental data for the Reference field.

3.2.2 Upscaling of Reference Field

To obtain the upscaled models, we used the geometric averaging technique, which is a common method for upscaling hydraulic conductivities. The hydraulic conductivity was upscaled in the section between $z = 7$ and $z = 71$ (including 32 layers). The Reference field was upscaled to three different resolutions referred to as Upscale A, Upscale B, and Upscale C, corresponding to upscaling the small-scale information (32 layers) to coarser layers (16, 8, and 4 layers, respectively). Thus, the hydraulic conductivity of the jth layer for each upscaled model was calculated as follows:

$$K_j^A = \exp\left(\frac{1}{2}\sum_{i=2j-1}^{2j} \ln K_i^R\right), \tag{3.1}$$

$$K_j^B = \exp\left(\frac{1}{4}\sum_{i=4j-3}^{4j} \ln K_i^R\right), \tag{3.2}$$

$$K_j^C = \exp\left(\frac{1}{8}\sum_{i=8j-7}^{8j} \ln K_i^R\right), \tag{3.3}$$

where K_i^R is the hydraulic conductivity (cm/s) of the ith layer for the Reference field, and K_j^A, K_j^B, and K_j^C are the hydraulic conductivity (cm/s) of the jth layer for Upscale A, Upscale B, and Upscale C, respectively. The vertical variations in hydraulic conductivity for the three upscaled models are presented in Figures 3.2(b)–(d), which indicate that information was lost after increasing the layer thickness in the Reference

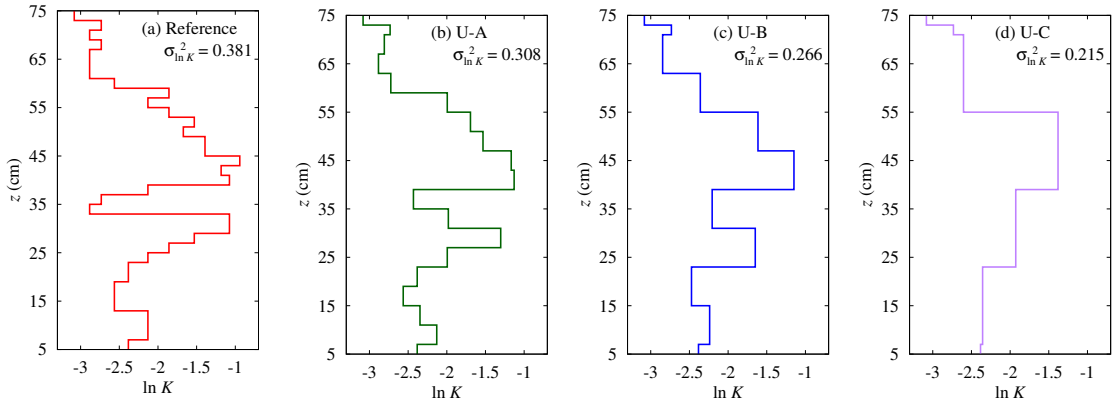

Figure 3.2: Vertical variations in hydraulic conductivity for (a) Reference field, (b) Upscale A, (c) Upscale B, and (d) Upscale C. $\sigma^2_{\ln K}$ denotes the variance of $\ln K$.

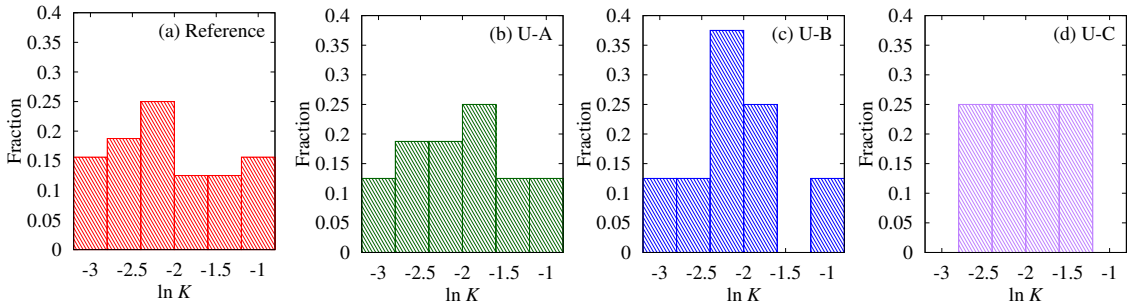

Figure 3.3: Histograms of hydraulic conductivity for (a) Reference field, (b) Upscale A, (c) Upscale B, and (d) Upscale C.

field. Histograms of the hydraulic conductivity in the section between $z = 7$ and $z = 71$ for all models are displayed in Figure 3.3. Note that extreme values of $\ln K$, such as $\ln K < -3$ or $\ln K > -1$, did not exist in Upscale C (as illustrated in Figure 3.3(d)) because the stratified model was smoothed out by upscaling.

To quantify the degree of heterogeneity for the stratified models, the variance of $\ln K$ was calculated as

$$\sigma^2_{\ln K} = \frac{1}{n}\left(\sum_{i=1}^{n}(\ln K_i)^2 - n(\ln M)^2\right), \tag{3.4}$$

where $\sigma^2_{\ln K}$ is the variance of $\ln K$, which is related to the degree of solute dispersion (Beaudoin and Dreuzy, 2013; Gelhar et al., 1979; Gelhar and Axness, 1983); n is the number of layers; and M is the geometric mean of hydraulic conductivity in the stratified model. Figure 3.2 also displays $\sigma^2_{\ln K}$ for each model. Comparing the

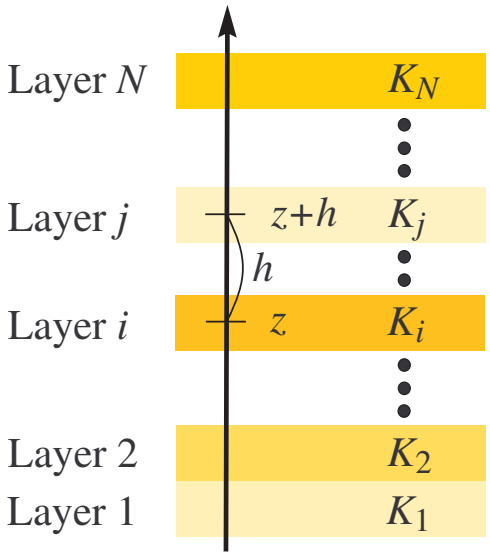

Figure 3.4: Schematic diagram of the calculation method for the experimental semivariogram.

values of $\sigma^2_{\ln K}$ reveals that the smoothing effect of upscaling reduced the degree of heterogeneity of the models.

3.2.3 Geostatistical Analysis

It is known that the degree of solute dispersion is highly dependent on the spatial correlation of hydraulic conductivity (i.e., correlation length) as well as the degree of heterogeneity (Gelhar and Axness, 1983). Therefore, we evaluated the correlation structure for the stratified models (only in the section between $z = 7$ and $z = 71$) using geostatistical analysis. In general, the variability of hydraulic conductivity exhibits a correlation structure, and geostatistical analysis enables quantification of the spatial correlation. A useful tool for the analysis is the experimental semivariogram, which is calculated as the mean square difference between the sample values at specified separation distances (Hess et al., 1992; Sudicky, 1986):

$$\gamma(h) = \frac{1}{2n(h)} \sum_{i=1}^{n(h)} \Big(\ln K(z+h) - \ln K(z) \Big)^2, \tag{3.5}$$

where $\gamma(h)$ is the variogram statistic, $n(h)$ is the number of data pairs separated by h, and h is the separation distance between observations. Figure 3.4 presents a schematic diagram of the calculation method for the experimental semivariogram.

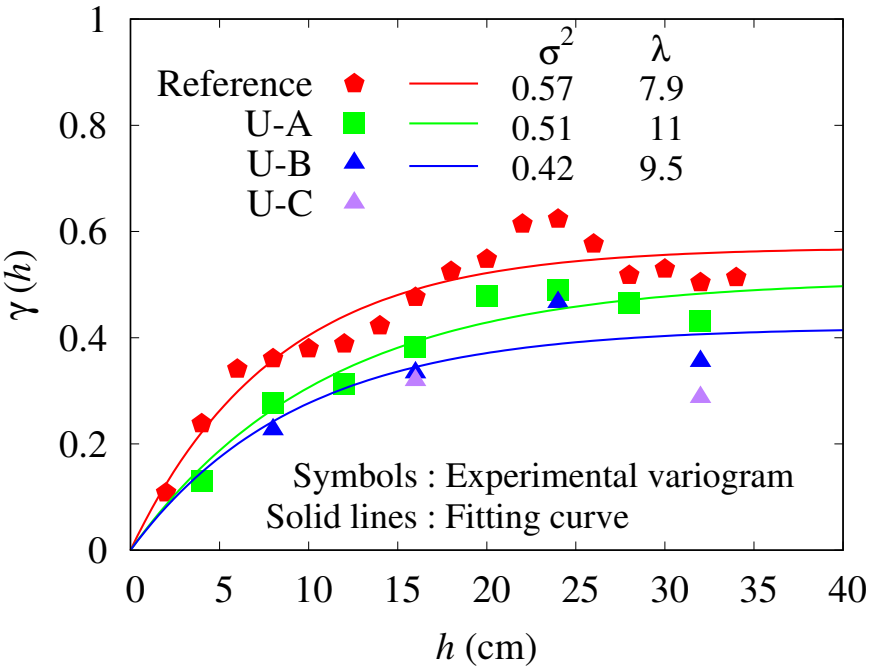

Figure 3.5: Calculated variograms and fitting curves for the stratified models.

The following standardized exponential model was selected to represent the general trend of the discontinuous variograms:

$$\gamma(h) = \sigma^2\left(1 - \exp\left(\frac{-h}{\lambda}\right)\right), \tag{3.6}$$

where σ^2 is the variogram sill, and λ is the correlation length. Exponential models were fitted to the experimental variograms by minimizing the sum of squares of the difference between the exponential model and experimental variogram; thus, the two unknown parameters (i.e., σ^2 and λ) were computed. Because Upscale C had only three data pairs, it was excluded and not used for fitting. The calculated variograms and fitting curves are presented in Figure 3.5 together with the computed parameters, including σ^2 and λ. It can be seen that the variogram sill values tended to decrease monotonically with the layer thickness of the stratified model, while the correlation length was not dependent on layer coarsening. Therefore, the results of the geostatistical analysis indicate that the correlation structure of hydraulic conductivity for a stratified model is not significantly affected by layer coarsening due to upscaling.

3.3 Laboratory-Scale Tracer Experiment

3.3.1 Experimental Setup

To construct the Reference field in the laboratory, 13 uniform silica sands of different mean grain sizes were used. The hydraulic conductivity of each sand was estimated by a one-dimensional column experiment under steady-state flow conditions and with a porosity of 0.473. The experiments were conducted in a laboratory flow tank with internal dimensions of 80 cm × 200 cm × 3 cm (length × width × depth). Figure 3.6 presents a schematic diagram of the flow tank. The tank was composed of a stainless steel exterior frame and two transparent sheets. The x-axis of the coordinate system was parallel to the bottom of the flow tank (i.e., $x = 0$ was at the row of injection ports), while the z-axis was orthogonal to it (i.e., $z = 0$ was at the bottom of the tank). Constant head spill reservoirs connected to the upstream and downstream ends of the flow tank were used to control the flow through the outer boundaries of the porous media (right-hand side in Figure 3.6). The porous media and side reservoirs were separated by fine mesh screens, and 11 holes sealed with a silicone rubber septum were prepared for tracer injection.

3.3.2 Experimental Procedure

A wet packing procedure was used to prevent air bubbles from being trapped in the porous media, which can lead to pore clogging and changes in permeability. Packing was performed layer by layer to establish different zones with a porosity of 0.473. The Reference field (70 cm × 180 cm × 3 cm) was embedded in the flow tank. To prevent sand from escaping, coarse sand ($\ln K = -1.18$) areas were located on the upstream and downstream sides of the embedded Reference field area. The area of the Reference field was also sandwiched between fine sand ($\ln K = -5.74$). Separation between regions of sand of different grain sizes was achieved using thin metal dividers. The dividers were removed as the packing proceeded.

After packing, by using the constant head spill reservoirs, we achieved a constant flow rate under a hydraulic gradient of 0.075. Once steady flow conditions were established, a solution of Brilliant Blue FCF with a volume of 220 cm^3 and a concentration of 0.2 mg/cm^3 was injected using the 11 injection ports along the z-axis (see Figure 3.6).

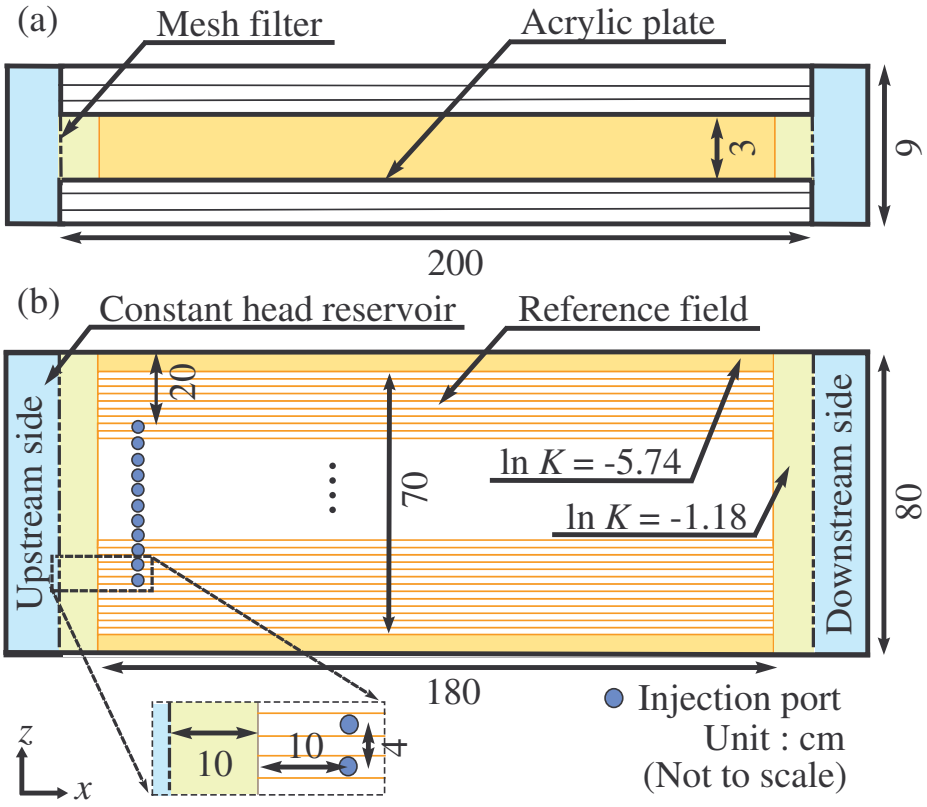

Figure 3.6: Schematic diagram of flow tank. (a) Top view and (b) front view.

A digital camera was used to continuously record the red, green, and blue (RGB) color images of the tracer experiment. Two light sources were placed at a distance of 100 cm from the flow tank.

3.3.3 Image Analysis and Spatial Moment Approach

Using the RGB color image at each time and the spatial moment approach, we quantified the solute transport processes. By the same methodology as described in Section 2.2.4, each color image was converted to a tracer concentration value (i.e., concentration map) using calibration curves. Figure 3.7 presents the calibration curves obtained for three different sands. The pixel intensity (i.e., red value) is related to the size of the sand grain; however, calibration curves for similar grain sizes exhibit similar trends. Thus, the calibration curves of $\ln K = -0.0942$, -2.13 and -4.19 were assigned to large, intermediate, and small grain sizes, respectively. To estimate the strength of the

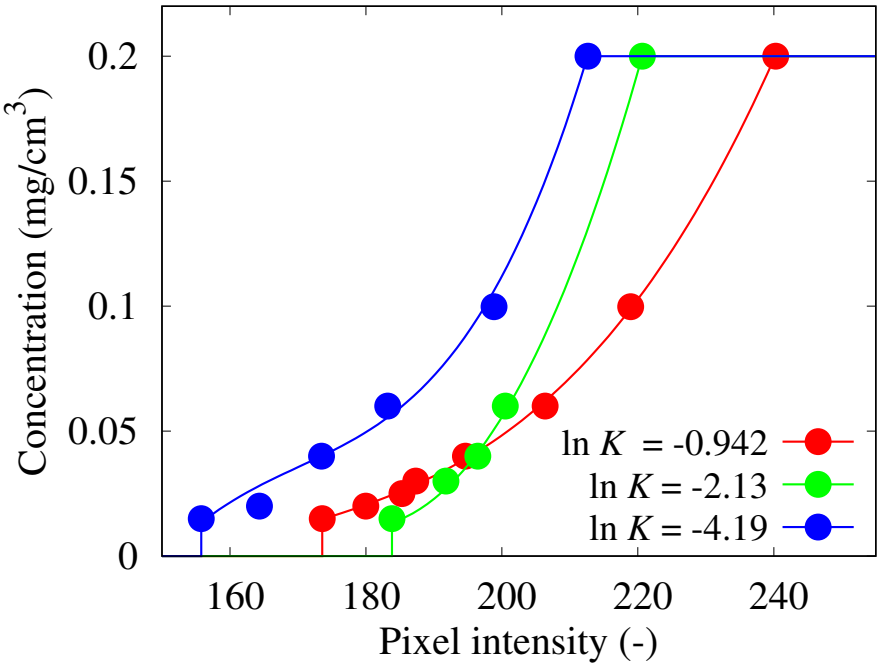

Figure 3.7: Calibration curves of concentration versus pixel intensity (i.e., red value) for representative sands ($\ln K = -0.0942$, -2.13, and -4.19).

dispersion process (i.e., the longitudinal and transverse macrodispersivities), we used the same methodology as in Section 2.2.5; thus, we employed the spatial moment approach.

3.4 Numerical Simulation

3.4.1 Flow and Transport Models

To evaluate the effect of upscaling on solute dispersion, we performed flow and transport simulations. The flow was calculated according to the governing steady-state flow equation in saturated porous media obtained by combining Darcy's law and the continuity equation (see Appendix A):

$$\nabla \cdot (K(\mathbf{x}) \nabla h) = 0, \tag{3.7}$$

where h is the piezometric head, $\mathbf{x} = (x_1, x_2)$ is the position vector, and $K(\mathbf{x})$ is the hydraulic conductivity tensor. Here, x_1 and x_2 denote the positions in the x- and z-directions, respectively. The hydraulic conductivity tensor was assumed to be isotropic and was therefore characterized by a scalar value. The flow was driven by a

mean hydraulic gradient oriented parallel to the x-direction. The boundary conditions were no-flux at boundaries parallel to the mean flow. Therefore, as in the experiment, the hydraulic gradient forced the flow from left to right. Neglecting the temporal and spatial changes in porosity n, the pore velocity vector $\mathbf{v}$ was calculated as follows:

$$\mathbf{v} = -(K(\mathbf{x})\nabla h)/n, \tag{3.8}$$

To model solute movement through porous media, we employed the random walk particle tracking (RWPT) method. RWPT simulates solute transport by partitioning the solute mass into a large number of representative particles. The displacement of a particle is expressed in its traditional form given by the Itô–Taylor integration scheme:

$$\mathbf{X}_p(t + \Delta t) = \mathbf{X}_p(t) + \frac{(\mathbf{v} + \nabla \cdot \mathbf{D})\Delta t}{R} + \mathbf{B}\boldsymbol{\Xi}\sqrt{\Delta t}, \tag{3.9}$$

where $\mathbf{X}_p$ is the position of the particle, Δt is the time interval, R is the retardation factor, and $\boldsymbol{\Xi}$ is a vector of independent, normally distributed random variables with zero mean and unit variance. In addition, $\mathbf{D}$ is the dispersion coefficient tensor given by

$$D_{ij} = \alpha_T|\mathbf{v}|\delta_{ij} + \frac{(\alpha_L - \alpha_T)v_i v_j}{|\mathbf{v}|}, \tag{3.10}$$

where v_i is the ith component of the pore velocity, δ_{ij} is the Kronecker delta, and $\mathbf{B}$ is the displacement matrix, which is a tensor defining the strength of dispersion. For isotropic porous media, the two-dimensional form of $\mathbf{B}$ can be expressed as

$$\mathbf{B} = \begin{pmatrix} \dfrac{v_1}{|\mathbf{v}|}\sqrt{\dfrac{2\alpha_L|\mathbf{v}|}{R}} & -\dfrac{v_2}{|\mathbf{v}|}\sqrt{\dfrac{2\alpha_T|\mathbf{v}|}{R}} \\ \dfrac{v_2}{|\mathbf{v}|}\sqrt{\dfrac{2\alpha_L|\mathbf{v}|}{R}} & \dfrac{v_1}{|\mathbf{v}|}\sqrt{\dfrac{2\alpha_T|\mathbf{v}|}{R}} \end{pmatrix}, \tag{3.11}$$

where α_L and α_T are the local longitudinal and transverse dispersivities, respectively. To simulate solute transport under the experimental conditions, we assumed a line source at $x = 0$. The initial number of particles was 5.0×10^4 (Inoue et al., 2017). The parameter values for RWPT are listed in Table 3.1.

Table 3.1: Parameter values for the numerical simulation by random walk particle tracking (RWPT).

Parameter	Description	Value
α_L	Local longitudinal dispersivity	2 cm
α_T	Local transverse dispersivity	0.5 cm
R	Retardation factor	1.0
Δt	Time interval	1.0 s
N	Number of particles	5.0×10^4

3.4.2 Spatial Moment Approach of RWPT

The spatial moments were calculated from snapshots of solute particles at given times as follows (Fernàndez-Garcia, Illangasekare, et al., 2005):

$$X_{G,i} = \frac{1}{m(t)} \sum_{k=1}^{NP_t} \frac{m_p^k X_{p,i}^k(t)}{R(\mathbf{X}_p^k(t))}, \tag{3.12}$$

$$m(t) = \sum_{k=1}^{NP_t} \frac{m_p^k}{R(\mathbf{X}_p^k(t))}, \tag{3.13}$$

$$S_{ij}(t) = \frac{1}{m(t)} \sum_{k=1}^{NP_t} \frac{m_p^k X_{p,i}^k(t) X_{p,j}^k(t)}{R(\mathbf{X}_p^k(t))} - X_{G,i}(t) X_{G,j}(t) \qquad i,j = 1,2, \tag{3.14}$$

where $X_{p,i}^k$ is the i-component of the kth particle location, $X_{G,i}$ is the center of mass, m_p^k is the mass assigned to the kth particle, $m(t)$ is the total liquid-phase solute mass, S_{ij} denotes the liquid-phase second spatial moments, and NP_t is the number of particles in the system at time t. The macrodispersivities were calculated from the spatial moments as (Fernàndez-Garcia, Illangasekare, et al., 2005)

$$A_L(\xi_G(t)) = \frac{S_{11}(t)}{2\xi_G(t)}, \tag{3.15}$$

$$A_T(\xi_G(t)) = \frac{S_{22}(t)}{2\xi_G(t)}, \tag{3.16}$$

where $\xi_G(t)$ is the travel distance of the center of mass of the tracer plume in the mean flow direction at time t.

3.5 Results and Discussion

3.5.1 Comparison Between Experiment and Numerical Simulation

Figure 3.8 presents images obtained from the tracer experiment for the Reference field, while Figure 3.9 presents the distributions of the solute particles obtained by RWPT. Of the total 5.0×10^4 particles, a random subset of 5.0×10^2 particles capable of capturing the full extent of the plume is plotted. The simulated spatial profiles (Figure 3.9) are in qualitative agreement with the images (Figure 3.8).

Figure 3.10 compares the macrodispersivities obtained in the tracer experiment and the numerical simulation by RWPT. An increase in longitudinal macrodispersivity with displacement distance can be observed for both the experiment and RWPT. This scale dependence of longitudinal macrodispersivity is well known and has been reported in previous studies (Fernàndez-Garcia, Illangasekare, et al., 2005; Gelhar and Axness, 1983; Gelhar et al., 1992). However, in contrast to the longitudinal macrodispersivity, the transverse macrodispersivity exhibits a tendency to decrease with displacement distance, which agrees with the results in Section 2.3.2. As a result, the macrodispersivities from the experiment and numerical simulation are in reasonably good agreement, thus indicating that the numerical model (i.e., RWPT) is a sufficiently accurate predictive tool.

3.5.2 Impact of Upscaling on Macrodispersivities

The longitudinal and transverse macrodispersivities for the Reference field and the upscaled models were calculated using numerical simulation by RWPT and are depicted in Figure 3.11. The use of a coarse layer in the upscaled models led to underestimation of the longitudinal macrodispersivity, whereas the transverse macrodispersivity did not change with the layer thickness. Although velocity fluctuations along the x-axis (i.e., longitudinal direction) were largely mitigated by upscaling the Reference field, fluctuations along the z-axis (i.e., transverse direction) were not affected by upscaling since they were extremely small for the stratified porous media.

Figure 3.12 displays the relationship between the computed longitudinal macrodispersivities and the variance of $\ln K$, which is widely recognized as an important factor

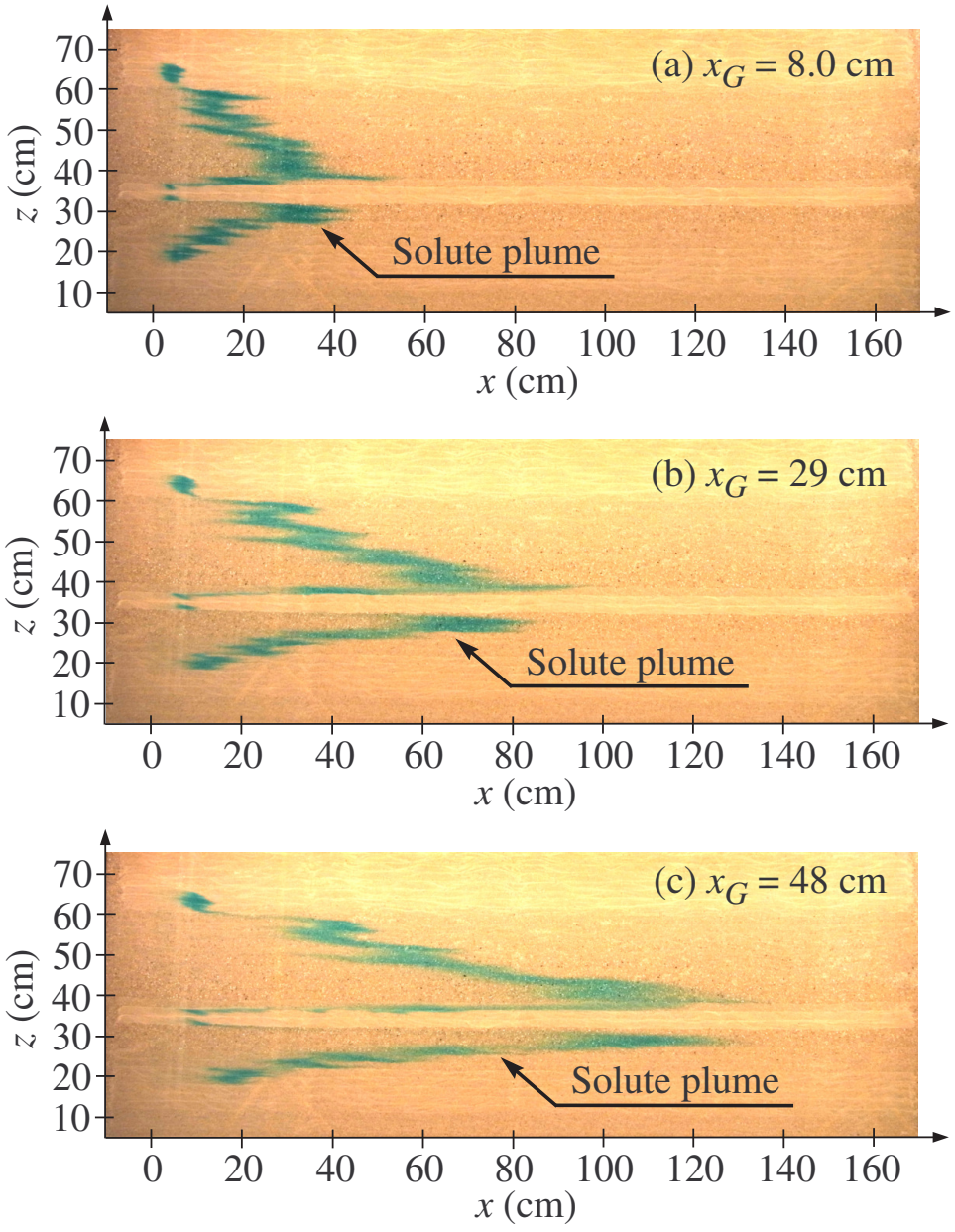

Figure 3.8: Images obtained from the tracer experiment for the Reference field. (a) $x_G = 8.0$ cm, (b) $x_G = 29$ cm, (c) $x_G = 48$ cm.

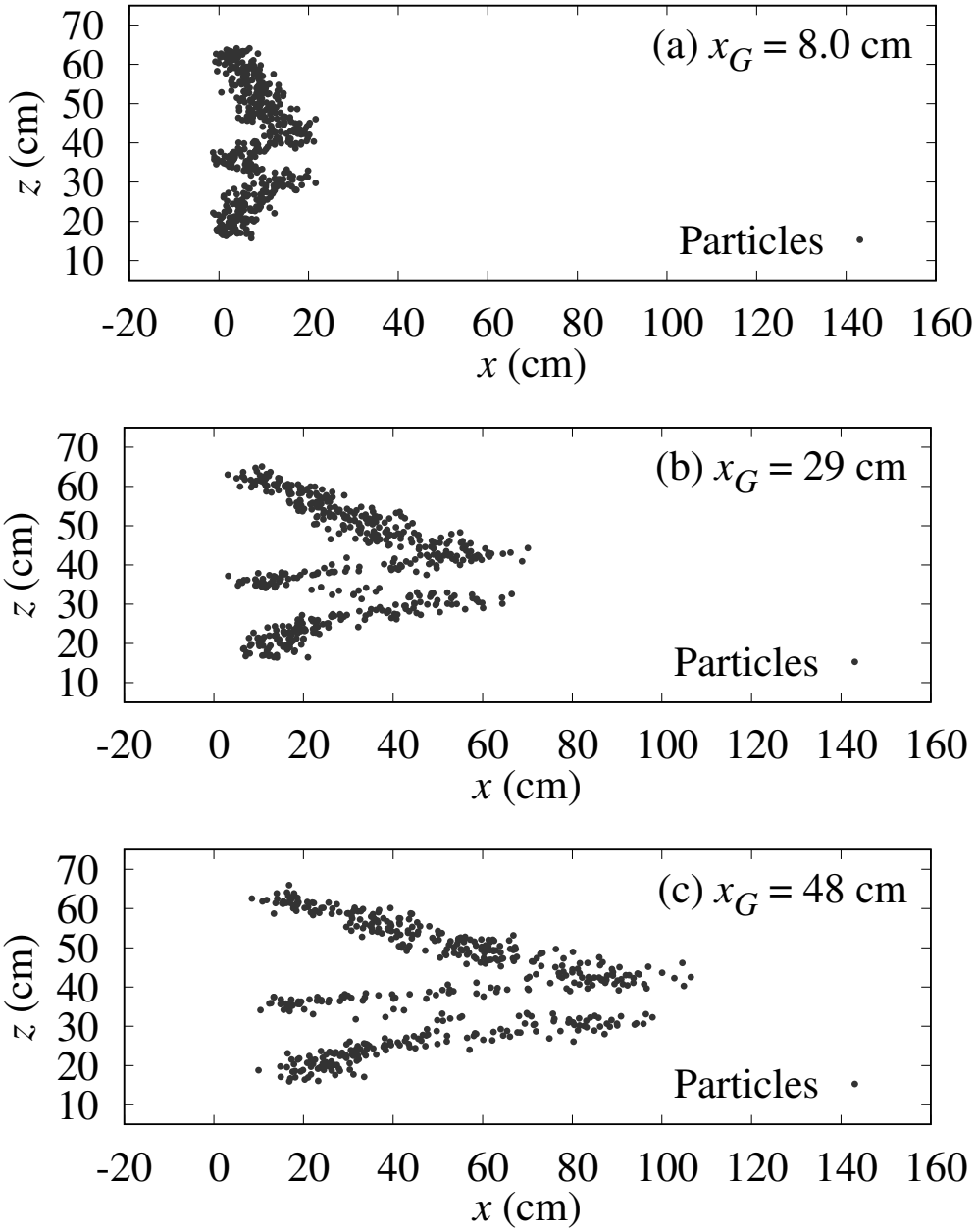

Figure 3.9: Distributions of solute particles obtained by random walk particle tracking for the Reference field. (a) $x_G = 8.0$ cm, (b) $x_G = 29$ cm, (c) $x_G = 48$ cm. Only a selected subset of 5.0×10^2 particles is presented in each dot.

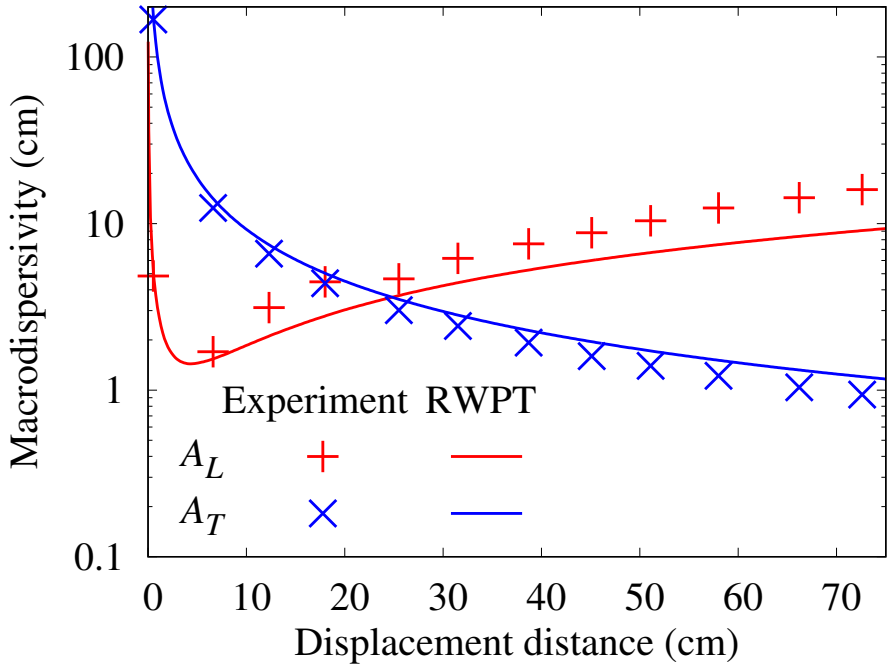

Figure 3.10: Comparison of macrodispersivities obtained in the tracer experiment and numerical simulation by random walk particle tracking (RWPT).

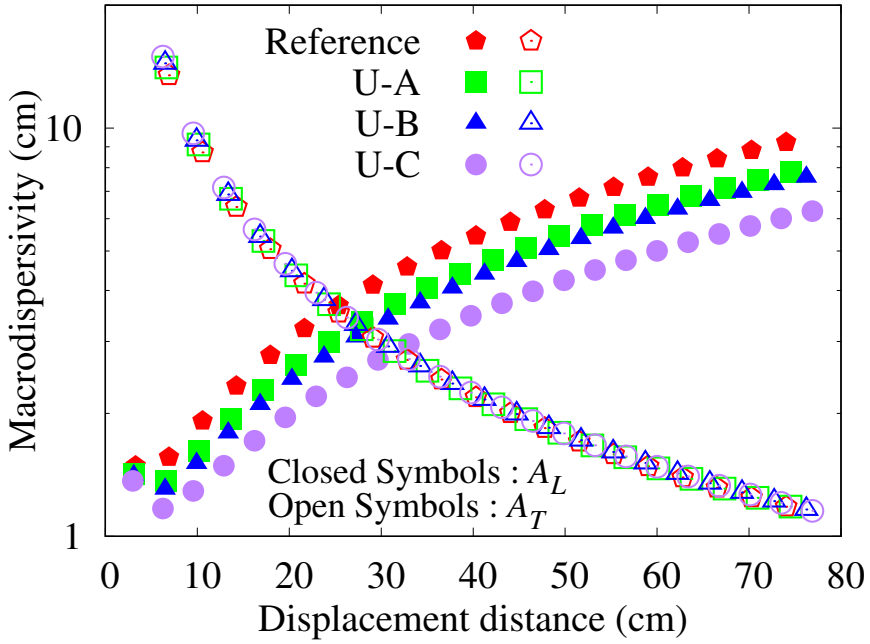

Figure 3.11: Comparison between macrodispersivities for the Reference field and upscaled models.

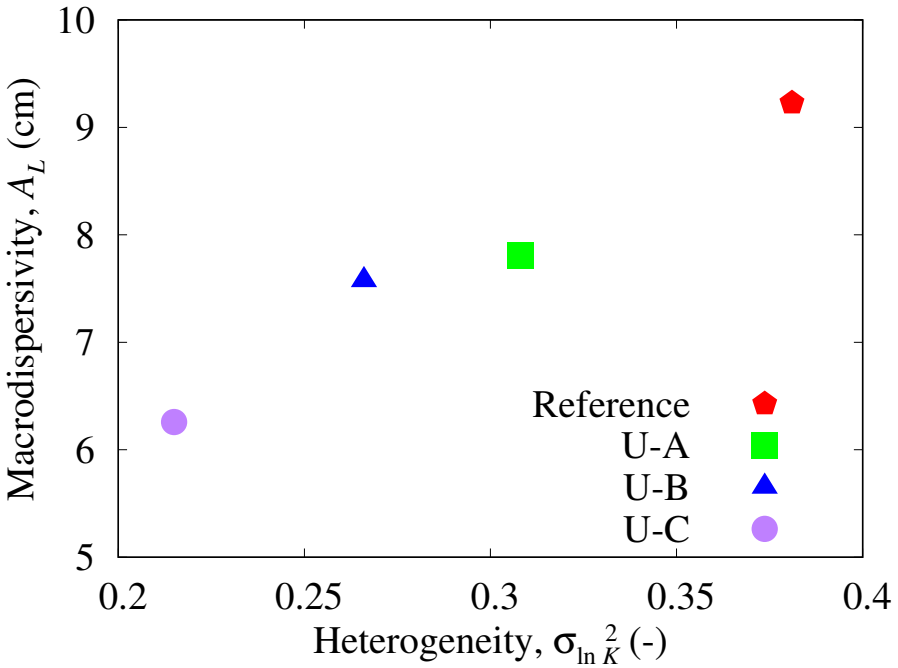

Figure 3.12: Relationship between longitudinal macrodispersivity and heterogeneity (variance of $\ln K$).

controlling the strength of solute dispersion. The longitudinal macrodispersivity values corresponding to the maximal displacement distance are plotted, and linear growth of A_L with the variance of $\ln K$ (i.e., strength of heterogeneity) can be observed, except for Upscale B. This indicates that the variance of $\ln K$ (i.e., strength of heterogeneity) is highly correlated with the longitudinal macrodispersivity. However, the A_L value for Upscale B is slightly larger than expected from the previously discussed linear relationship between A_L and the variance of $\ln K$. In addition to the variance of $\ln K$, the spatial correlation of hydraulic conductivity is also recognized as an important factor controlling the degree of the solute dispersion. However, as can be seen in Figure 3.5, the changes in the correlation length by upscaling are not large. These results suggest that evaluating the changes in structure characteristics by upscaling only in terms of heterogeneity and correlation length is not sufficient to understand the effect of upscaling. The following section explores the effect of other factors by analyzing solute transport processes.

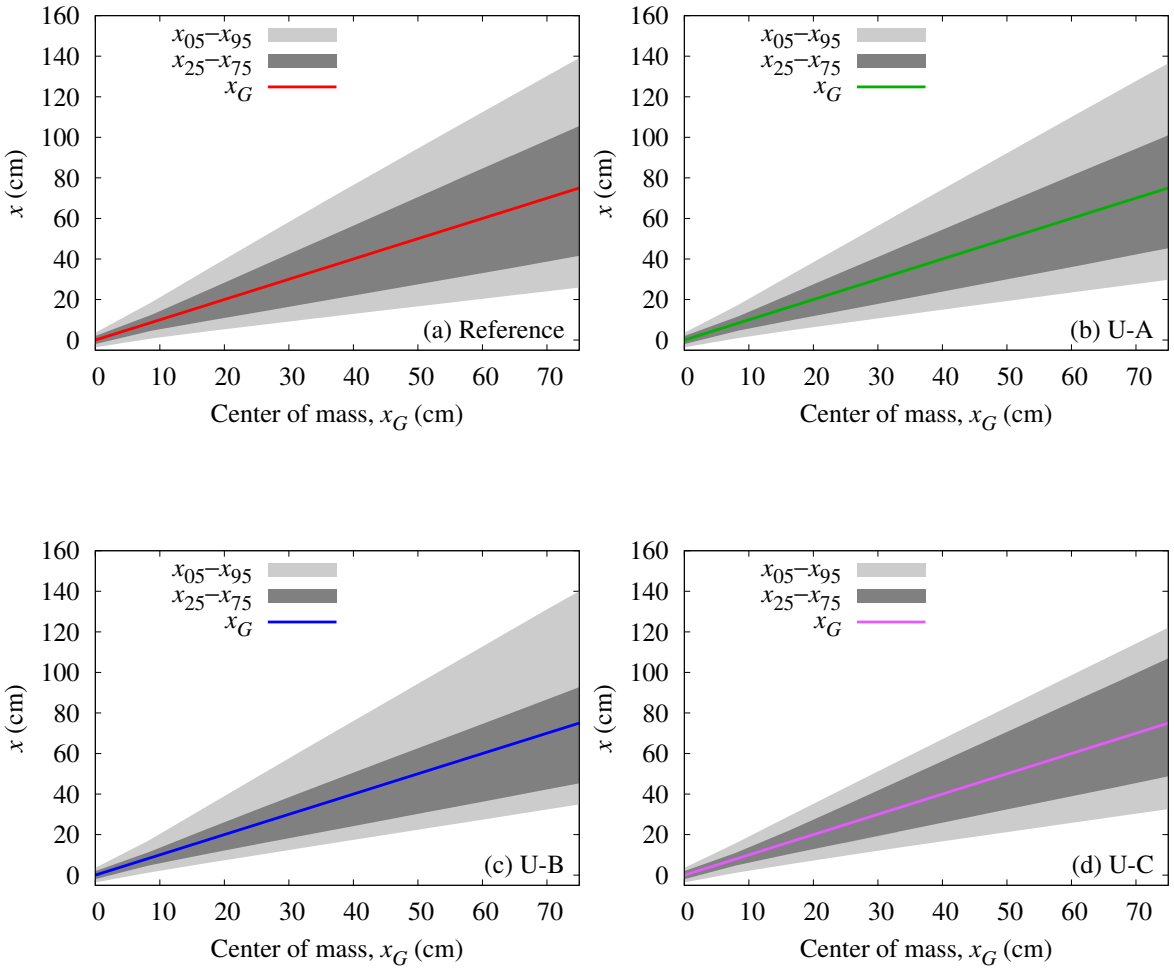

Figure 3.13: Travel distances x_{05}, x_{25}, x_{75}, and x_{95} of solute particles. (a) Reference field, (b) Upscale A, (c) Upscale B, (d) Upscale C. Solid lines represent the travel distance of the center of mass, while light and dark gray regions denote x_{05}–x_{95} and x_{25}–x_{75}, respectively.

3.5.3 Evaluation of Solute Dispersion Processes in Terms of Forward and Backward Tails

To further quantify the solute dispersion processes, we used the definition of the forward and backward tails of a solute plume that was provided in Chapter 2. We defined the travel distances x_{05}, x_{25}, x_{75}, and x_{95} corresponding to the 5th, 25th, 75th, and 95th percentiles, respectively, of the cumulative concentrations in the x-direction. Figure 3.13 presents the results of these travel distances, where light and dark gray regions denote x_{05}–x_{95} and x_{25}–x_{75}, respectively. The width of the light gray region (i.e., x_{05}–x_{95}) tended to decrease with layer thickness, except for Upscale B. This demonstrates that upscaling led to underestimation of the spread of the solute plume, which is

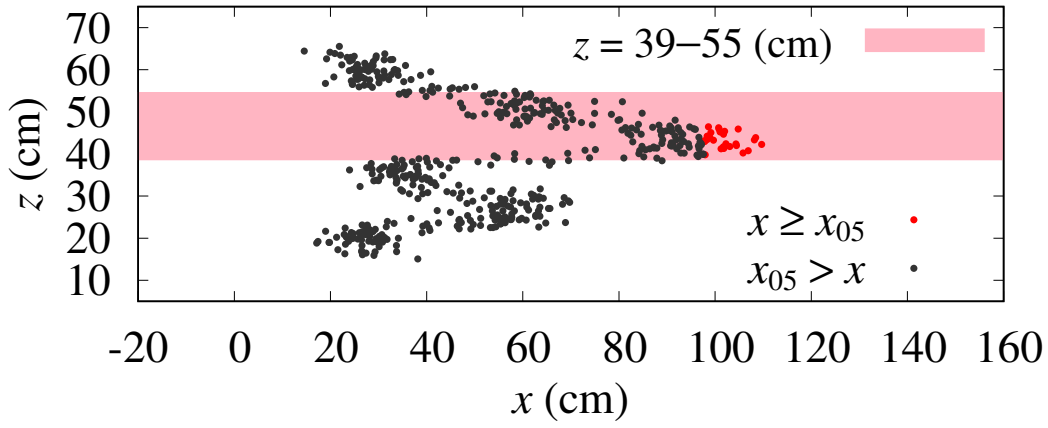

Figure 3.14: Distributions of solute particles obtained by random walk particle tracking for Upscale B at $x_G = 50$ cm. Only a select subset of 5.0×10^2 particles is presented in each dot. The red dots represent solute particles that exceed x_{05}.

consistent with the dependence of the longitudinal dispersivity on the layer thickness (see Figures 3.11 and 3.12). However, the width of the upper light gray zone (i.e., x_{05}–x_{25}) was broader for Upscale B than for the Reference field, Upscale A, and Upscale C, which demonstrates that the front of the solute plume was relatively fast for Upscale B.

To further analyze this observation, Figure 3.14 depicts the distribution of solute particles for Upscale B at $x_G = 50$ cm. The red dots denote solute particles that exceed x_{05}, and the red region represents layers of relatively high hydraulic conductivity ($z = 39$–55). As illustrated in Figure 3.14, all red dots are within the red region. As can be seen in Figure 3.2(a), there was a continuous high-K layer within the region of $z = 39$–55 for the Reference field. Therefore, for $z = 39$–55, the difference between the hydraulic conductivity of the Reference field and Upscale B was not significant. However, Upscale B had a larger layer thickness than the Reference field. Once solute particles entered a thick high-K layer, they continuously experienced higher flow velocity in the x-direction, which explains the fast transport of the forward tail for Upscale B. Thus, it was found that the strength of solute spreading (i.e., dispersion) is affected by changes in the characteristics of particle transitions between layers with different hydraulic conductivities, corresponding to increasing layer thickness by upscaling.

As can be seen in Figure 3.3(c), there was a layer with a relatively low hydraulic conductivity ($\ln K$ of less than -3) for Upscale B; however, Figure 3.13(c) indicates

that it did not significantly influence the extent of the backward tail. The low-conductivity layer was located above the position of the initial solute injection and did not contribute to solute spreading.

To accurately evaluate the extent of solute spreading, we calculated the distance between the forward and backward tails defined by

$$\Delta x_{05-95} = |x_{05}(x) - x_{95}(x)|, \tag{3.17}$$

$$\Delta x_{25-75} = |x_{25}(x) - x_{75}(x)|, \tag{3.18}$$

where x_{05-95} and x_{25-75} represent the distances between the forward and backward tails. In addition, to assess the extent of solute spreading in the z-direction (i.e., transverse direction), we also defined z_α, which is the vertical position corresponding to α of the cumulative frequency distribution on the z-axis, and calculated the distances z_{05-95} and z_{25-75} in the same manner as in equations (3.17) and (3.18):

$$\Delta z_{05-95} = |z_{05}(x) - z_{95}(x)|, \tag{3.19}$$

$$\Delta z_{25-75} = |z_{25}(x) - z_{75}(x)|. \tag{3.20}$$

Figure 3.15 presents the results of x_{05-95} and x_{25-75} versus the center of mass of solute plume (x_G). Similar to the results of longitudinal dispersivity (Figure 3.11), x_{05-95} exhibited a tendency to decrease with layer thickness. This result suggests that estimates of longitudinal macrodispersivity are greatly affected by the fastest and slowest portions of the solute plume. However, x_{25-75} did not depend on the layer thickness. Thus, the farther the solute plume is from the center of mass, the larger the effect of upscaling is.

Figure 3.16 presents the results of z_{05-95} and z_{25-75} versus the center of mass (z_G). This figure indicates that z_{05-95} and z_{25-75} did not change with upscaling. Therefore, in agreement with the results of transverse macrodispersivity (see Figure 3.11), z_{05-95} and z_{25-75}, which represent transverse spreading of the solute plume, were not dependent on upscaling or the layer thickness.

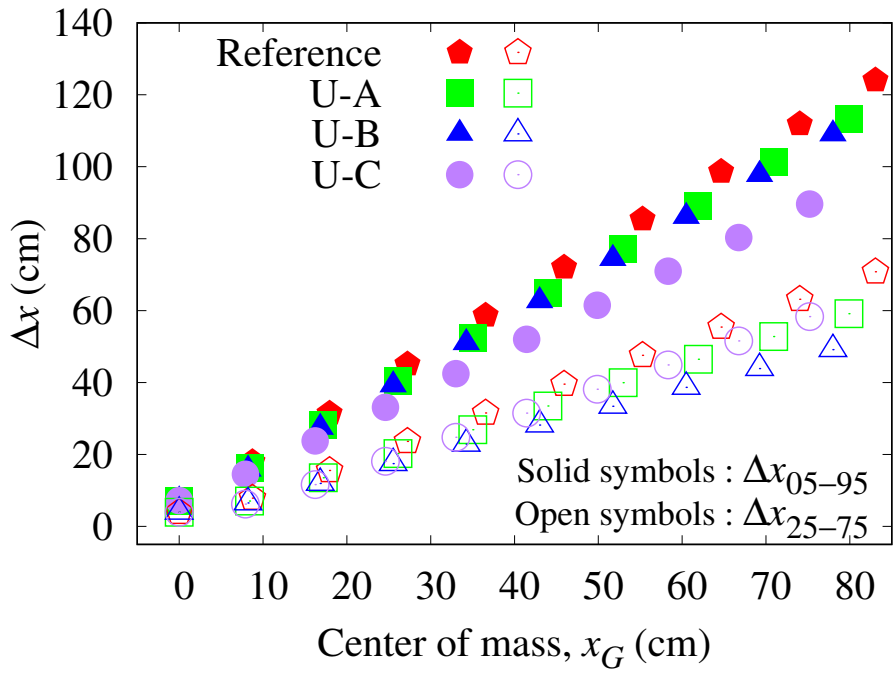

Figure 3.15: x_{05-95} and x_{25-75} versus center of mass (x_G). Solid and open symbols represent x_{05-95} and x_{25-75}, respectively.

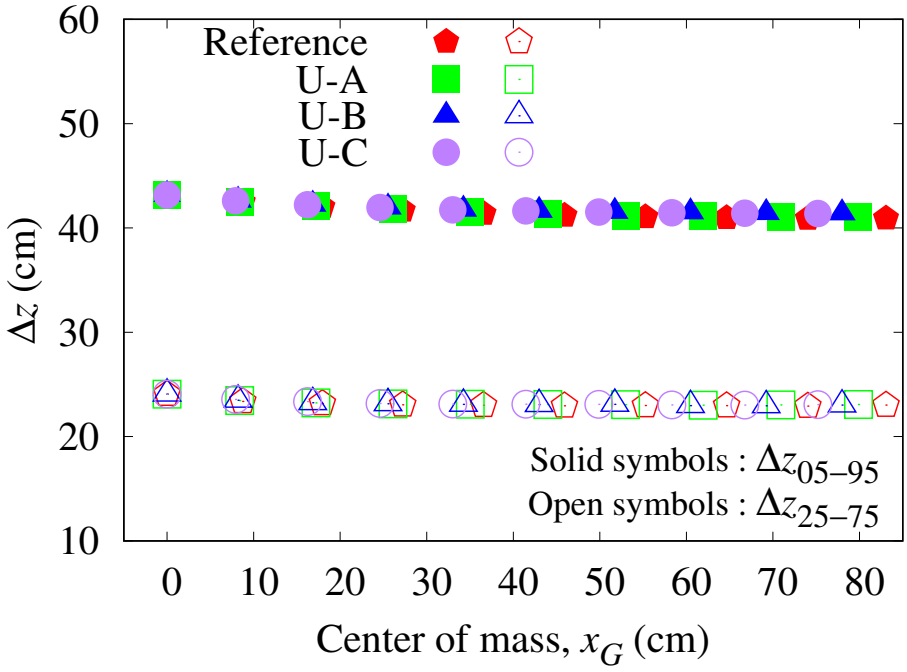

Figure 3.16: z_{05-95} and z_{25-75} versus center of mass (z_G). Solid and open symbols represent z_{05-95} and z_{25-75}, respectively.

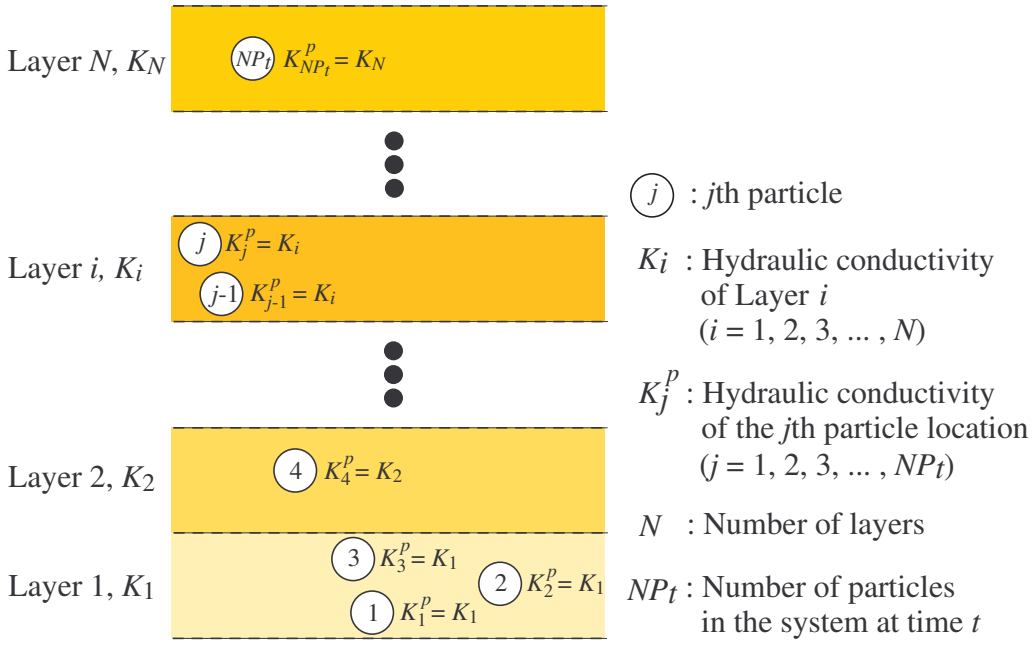

Figure 3.17: Schematic diagram of effective heterogeneity.

3.5.4 Effective Heterogeneity

As discussed in the previous section, changes in the characteristics of particle transitions between layers as well as the decrease in the variance of $\ln K$ by upscaling are correlated with the strength of longitudinal dispersion. When there is a difference between the hydraulic conductivities (i.e., velocity along the x-axis) of neighboring layers, it is more likely for solute particles to travel from a low-conductivity layer to a high-conductivity layer. Therefore, as time passes (i.e., the displacement distance increases), solute particles may be biased toward high-conductivity layers and experience less variable flow, resulting in a lower rate of solute spreading. To evaluate how particles are spatially distributed, we defined the effective heterogeneity $\sigma^2_{\ln K,ef}$ with the following equation:

$$\sigma^2_{\ln K,ef} = \frac{1}{NP_t}\left(\sum_{j=1}^{NP_t}(\ln K^p_j)^2 - NP_t(\ln M^p)^2\right), \tag{3.21}$$

where K^p_j is the hydraulic conductivity at the location of the jth particle, and M^p is the geometric mean of K^p_j. Figure 3.17 presents a schematic diagram of the effective heterogeneity. As seen in equation (3.21), effective heterogeneity is a measure of heterogeneity corresponding to the position of the solute particles.

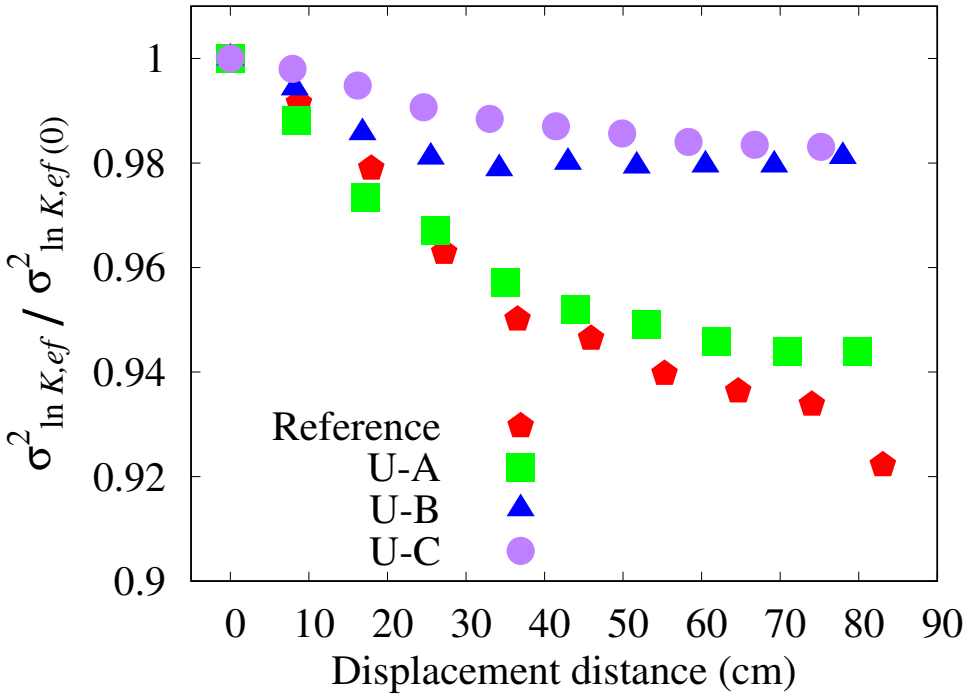

Figure 3.18: Effective heterogeneity versus displacement distance. $\sigma^2_{\ln K,ef(0)}$ denotes the estimates of effective heterogeneity at time $t = 0$.

Figure 3.18 displays the relationship between the effective heterogeneity and the displacement distance. To calculate the effective heterogeneity, the positions of the solute particles obtained from numerical simulation by RWPT were utilized. Here, $\sigma^2_{\ln K,ef(0)}$ denotes the estimates at time $t = 0$. For all models, the effective heterogeneity presented in Figure 3.18 exhibited a decreasing trend with displacement distance. This signifies that solute particles were biased toward high-conductivity layers at later times (i.e., larger distances). The effective heterogeneity also tended to increase with increasing layer thickness due to upscaling. This result is mainly attributed to the fact that upscaling leads to reduced travel between different conductivity layers. Furthermore, a much more rapid decrease in effective heterogeneity was observed for Upscale A than for Upscale B, which indicates that solute particles experienced a larger number of intrinsic heterogeneities for Upscale B than for Upscale A. That is why the estimate of longitudinal macrodispersivity for Upscale B was unexpectedly large, as illustrated in Figure 3.12. Therefore, to evaluate the effect of upscaling on

solute dispersion, we suggest that the increase in layer thickness as well as changes in the heterogeneity and correlation length is taken into consideration.

3.6 Conclusions

In this chapter, we evaluated how the strength of solute dispersion is affected by upscaling for stratified porous media. A combined experimental and numerical investigation was conducted to address this question. The results led to several conclusions as follows:

1. The smoothing effect of upscaling reduced the degree of heterogeneity, while the correlation length was not dependent on layer coarsening (i.e., upscaling).

2. For the Reference field, the longitudinal and transverse macrodispersivities obtained from numerical simulation by random walk particle tracking (RWPT) were in good agreement with those obtained from the experiment, which demonstrated the validity of the numerical simulation.

3. Use of a coarse layer in the upscaled models led to underestimation of the longitudinal macrodispersivity; in contrast, the transverse macrodispersivity did not change with upscaling.

4. The strength of longitudinal dispersion was affected by the increase in layer thickness as well as by changes in the heterogeneity and correlation length by upscaling.

4

Effect of Upscaling Two-Dimensional Heterogeneous Porous Media on Solute Dispersion

Contents

4.1 Introduction

Chapter 3 studied the effect of upscaling the hydraulic conductivity distribution on solute dispersion for stratified porous media, where the hydraulic conductivity varies

only in the vertical direction. In practice, natural sandy aquifers often exhibit geological stratification (Pickens and Grisak, 1981; Zavala-Sanchez et al., 2009); therefore, it is worthwhile to evaluate the effect of upscaling for such porous formations. However, natural soils and aquifers generally have a more complex structure; namely, they exhibit both vertical and horizontal fluctuations in hydraulic conductivity (Adams and Gelhar, 1992; Hess et al., 1992; Sudicky, 1986). Therefore, researchers have investigated the relationship between solute dispersion and upscaling for two- and three-dimensional heterogeneous porous media (Fernàndez-Garcia and Gómez-Hernández, 2007). However, the effect of upscaling has not yet been experimentally proven.

In this chapter, we present laboratory tracer experiments that evaluate the effect of upscaling on solute dispersion in two-dimensional randomly heterogeneous media. As in the previous chapters, an image analysis technique is employed for direct mapping of the solute concentration in porous media, and the strength of solute dispersion is evaluated.

4.2 Intermediate-Scale Laboratory Tracer Test

4.2.1 Soil Materials

To construct heterogeneous porous media in the laboratory, we first prepared silica sands of different grain sizes, namely, five sizes with diameters of 0.011, 0.030, 0.048, 0.081, and 0.145 cm. By blending the sands, 18 unique materials were developed. The hydraulic conductivity K of each sand was determined from constant head column experiments, resulting in $-4.19 < \ln K < -0.94$.

4.2.2 Flow Tank

We conducted experiments in a flow tank with internal dimensions of 100 cm $\times$ 100 cm $\times$ 3 cm (length $\times$ height $\times$ width). The flow tank was composed of a standard stainless steel exterior frame and two thick transparent plates. The two plates were placed in parallel to each other and enabled the visualization of solute transport. A schematic diagram of the flow tank is presented in Figure 4.1. The left and right reservoirs maintained the water levels, while the stainless steel mesh was used to separate both reservoirs from the central sand box region. The water levels in the flow tank were

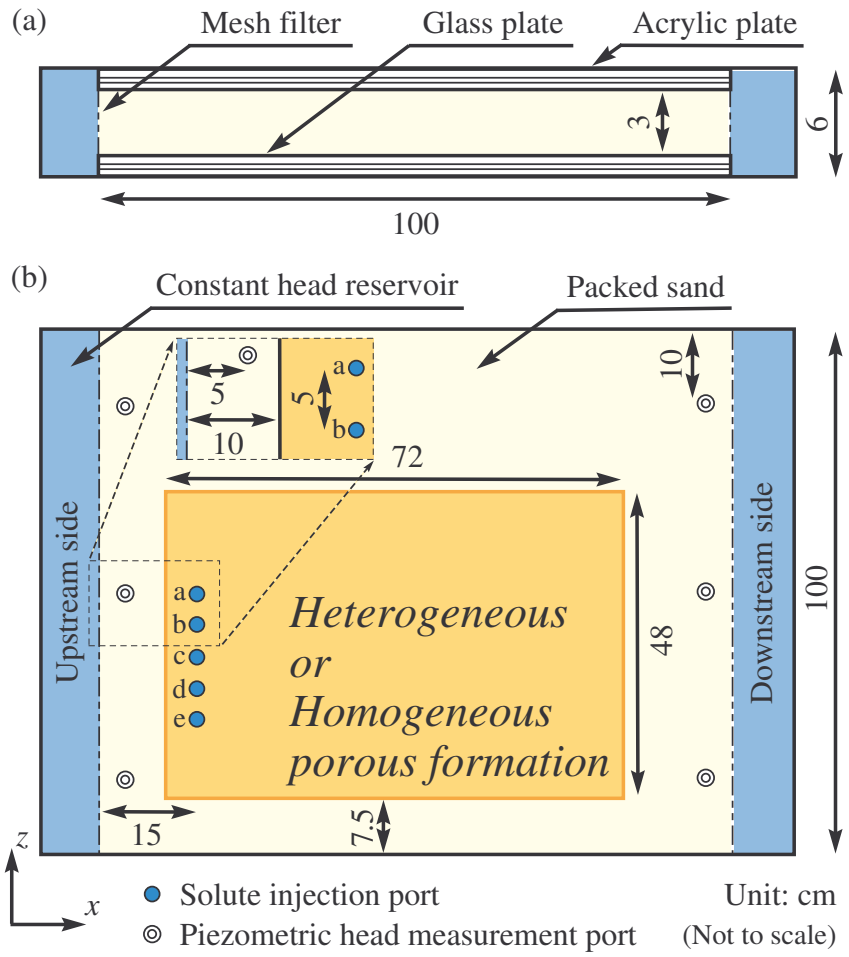

Figure 4.1: Schematic diagram of the flow tank. (a) Top view and (b) front view displaying the injection and pressure measurement ports.

monitored using six piezometers connected to the back of the tank. Five holes of 12 mm in diameter sealed with a silicone septum were prepared for tracer injection.

4.2.3 Reference Field

As a representative distribution of hydraulic conductivity describing a real aquifer, we generated a reference $\ln K$ field (hereinafter referred to as the Reference field), which was formed by 24×16 grid cells. The Reference field followed a log-normal probability density function and exhibited a weakly stationary, spatially correlated structure expressed by an exponential covariance function, which can be written as

$$\gamma(h) = \sigma^2 \left(1 - \exp\left(\frac{-h}{\lambda}\right)\right), \tag{4.1}$$

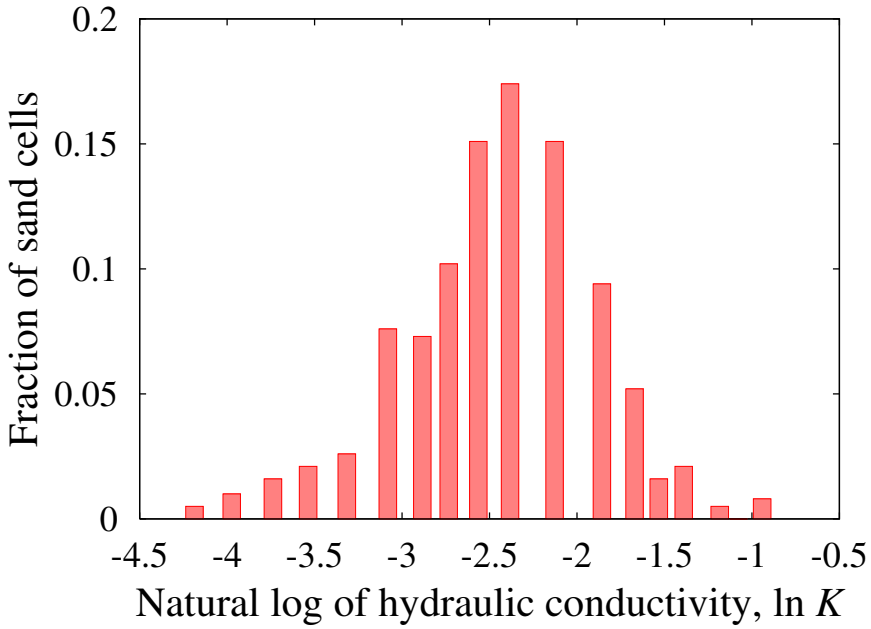

Figure 4.2: Histogram of hydraulic conductivity for the Reference field.

where γ is the variogram, σ^2 is the variogram sill value, λ is the correlation length, and h is the separation distance between observations. The resolution was of two grid cells within a correlation scale in the horizontal and vertical directions, and and the dimension of each cell was set to 3 cm $\times$ 3 cm.

Since 18 different sands were used in packing, the computer-generated values were binned into 18 classes corresponding to the sands used in packing. Figures 4.2 and 4.3(a) present the histogram and spatial distribution of hydraulic conductivity for the Reference field after binning into 18 classes. As can be seen in Figure 4.2, the Reference field exhibited an approximately log-normal distribution. Each cell was also numbered, as illustrated in Figure 4.4. The variance of $\ln K$ (i.e., the heterogeneity), which is highly correlated with the strength of solute dispersion (Beaudoin and Dreuzy, 2013; Gelhar et al., 1979; Gelhar and Axness, 1983), was calculated as follows:

$$\sigma^2_{\ln K} = \frac{1}{mn}\left(\sum_{i=1}^{m}\sum_{j=1}^{n}(\ln K_{i,j})^2 - mn(\ln M)^2\right), \tag{4.2}$$

where $\sigma^2_{\ln K}$ is the variance of $\ln K$, m and n are the number of cells in the x (horizontal) and z (vertical) directions, respectively, $K_{i,j}$ is the hydraulic conductivity of (i, j), and M is the geometric mean of the hydraulic conductivity.

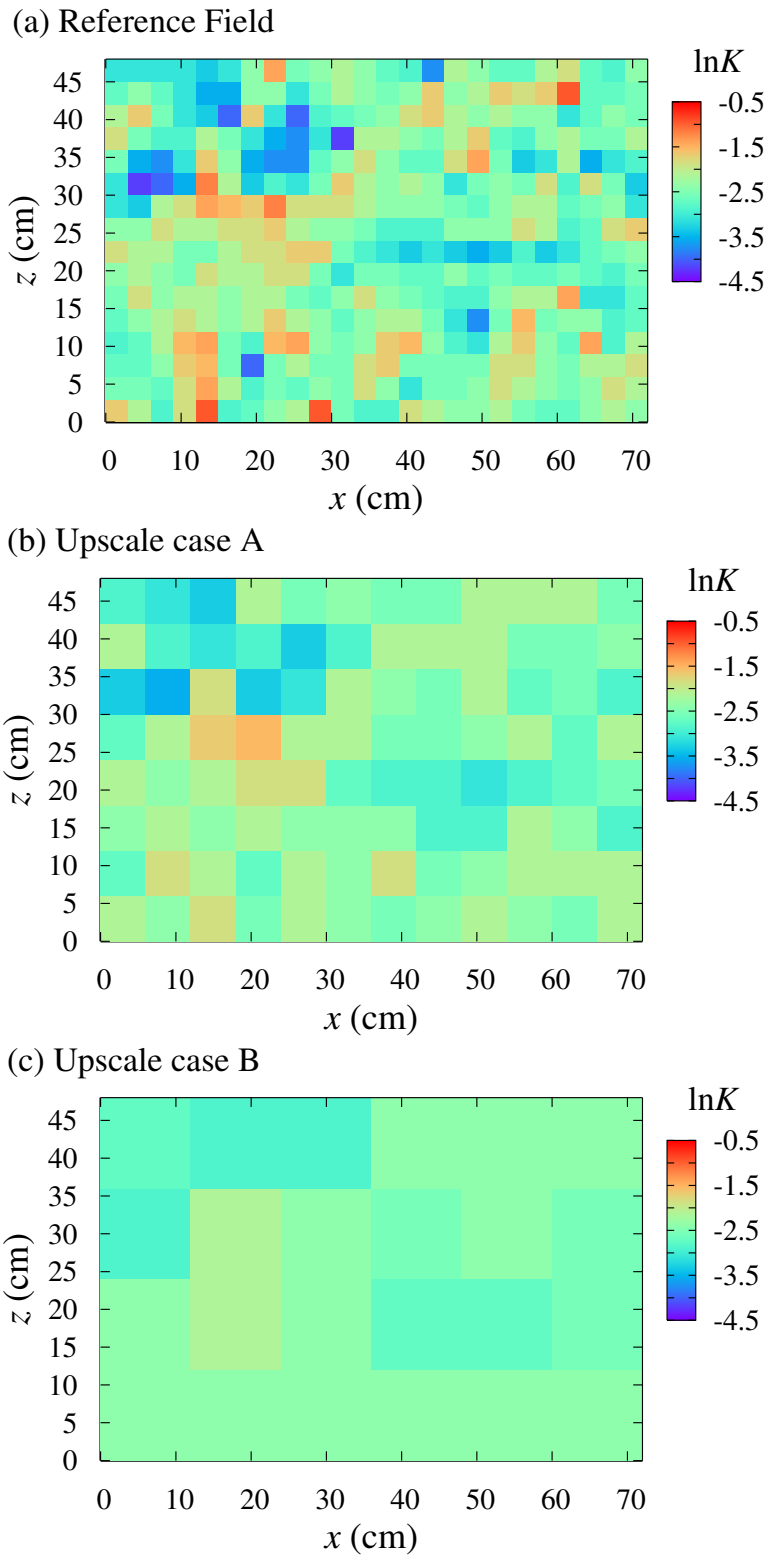

Figure 4.3: Hydraulic conductivity distributions. (a) Reference field, (b) Upscale A, (c) Upscale B.

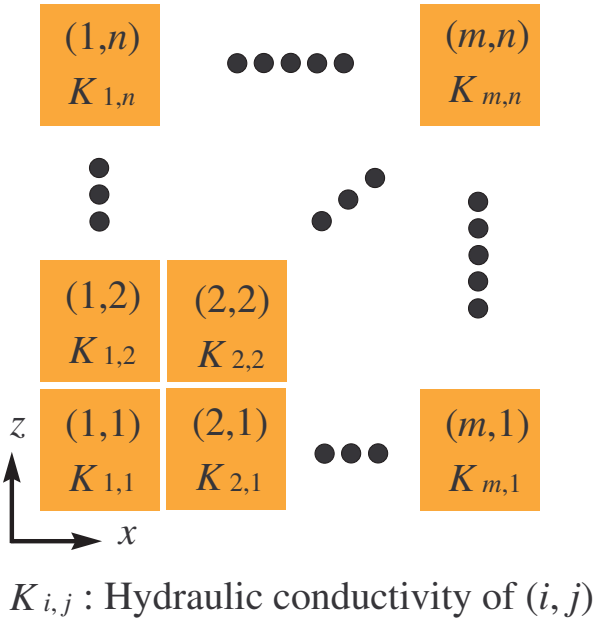

Figure 4.4: Cell numbering.

4.2.4 Upscaling of Hydraulic Conductivity

To evaluate the effect of upscaling on solute dispersion, the Reference field was upscaled to three different resolutions, referred to as Upscale A, Upscale B, and the Homogeneous case, corresponding to upscaling the small-scale K information (24×16 cells) to a regular computational grid of 12×8 blocks, 6×4 blocks, and 1×1 block, respectively. Here, as in Chapter 3, we used the geometric averaging technique to upscale the Reference field. Thus, the hydraulic conductivities of cell (i, j) for Upscale A and Upscale B were calculated as follows:

$$K^A_{i,j} = \exp \frac{1}{4}\left(\ln K_{2i-1,2j-1} + \ln K_{2i-1,2j} + \ln K_{2i,2j-1} + \ln K_{2i,2j}\right), \tag{4.3}$$

$$K^B_{i,j} = \exp \frac{1}{4}\left(\ln K^A_{2i-1,2j-1} + \ln K^A_{2i-1,2j} + \ln K^A_{2i,2j-1} + \ln K^A_{2i,2j}\right), \tag{4.4}$$

where $K^A_{i,j}$ and $K^B_{i,j}$ are the hydraulic conductivities of cell (i, j) for Upscale A and Upscale B, respectively. Figures 4.3(b) and (c) display the hydraulic conductivity distributions of Upscale A and Upscale B, which had $\sigma^2_{\ln K}$ values of 0.159 and 0.0741, respectively. We also considered the Homogeneous case, which represented the maximum level of upscaling. Table 4.1 presents a summary of the experimental cases.

Table 4.1: Summary of experimental cases.

	Number of cells	Grid spacing	Heterogeneity
Reference field	24×16	3×3 cm	0.307
Upscale A	12×8	6×6 cm	0.159
Upscale B	6×4	12×12 cm	0.0741
Homogeneous	1×1	72×48 cm	0.0

4.2.5 Experimental Procedure

In the heterogeneous systems (i.e., Reference field, Upscale A, and Upscale B), the generated packing structures (see Figure 4.3) were transferred to transparent sheets to scale and were attached to the wall of the flow tank to be used as templates for packing. Sand was then added to the flow tank according to the template under fully saturated conditions to avoid trapping air. Thin metal dividers were used to separate blocks of different types of sand and were removed as the packing proceeded. In the space outside the study area, which had dimensions of 72 cm $\times$ 48 cm $\times$ 3 cm (see Figure 4.1), sand with $\ln K = -1.18$ was added. After packing, a procedure similar to that described in Section 2.2.3 was followed to conduct the tracer experiments. However, there was a difference in the tracer injection methods. In this chapter, for each experimental case, we considered two injection methods: (i) a point source and (ii) a line source. For the point source, the tracer Brilliant Blue FCF was injected into one of the five injection ports (see Figure 4.1), whereas for the line source, it was simultaneously injected into all ports.

The same methodology as described in Sections 2.2.3 and 2.2.4 was used to perform visualization of solute transport in the tracer experiment performed for the Reference field, Upscale A, Upscale B, and the Homogeneous case, and to estimate the longitudinal and transverse macrodispersivities. Figure 4.5 presents the calibration curves for several silica sands (i.e., silica sands of $\ln K = -4.19$, -2.56, and -1.18). In addition, Figure 4.6 compares the plume image and concentration distribution from the line source at time $t = 720$ s for Upscale A. The concentration distribution agrees qualitatively with the images, with the formation of concentration gradients shaped by the spatial zonation.

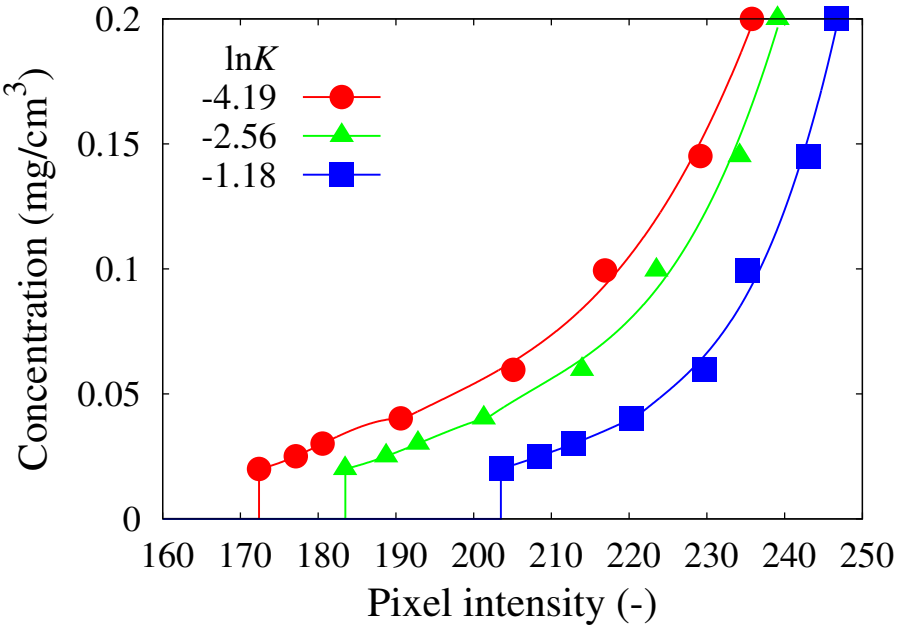

Figure 4.5: Calibration curves for several silica sands ($\ln K = -4.19$, -2.56, and -1.18).

4.3 Results and Discussion

4.3.1 Longitudinal Macrodispersivity

Figure 4.7 presents the longitudinal macrodispersivities obtained from the line source as a function of displacement distance for different degrees of upscaling. It can be seen that A_L decreased with a decreasing resolution of hydraulic conductivity (i.e., upscaling). For longitudinal macrodispersivity values corresponding to the maximal displacement distance, the estimate of the Reference field was approximately twice as large as that of Upscale A and approximately 10 times as large as that of Upscale B. To further analyze this result, Figure 4.8 displays the images for the Reference field and the three upscaled models at a displacement distance of approximately 33 cm. For the Reference field, the tracer plume was irregular in shape and appeared to follow preferential pathlines, resulting in enhanced solute spreading in the longitudinal direction. However, solute spreading in the x-direction and the degree of irregularity of the plume shape decreased with upscaling. In particular, whereas the solute plumes for the Reference field and Upscale A exhibited strong tailing, tailing was not observed for Upscale B and the Homogeneous case. This result explains the large discrepancy between the A_L

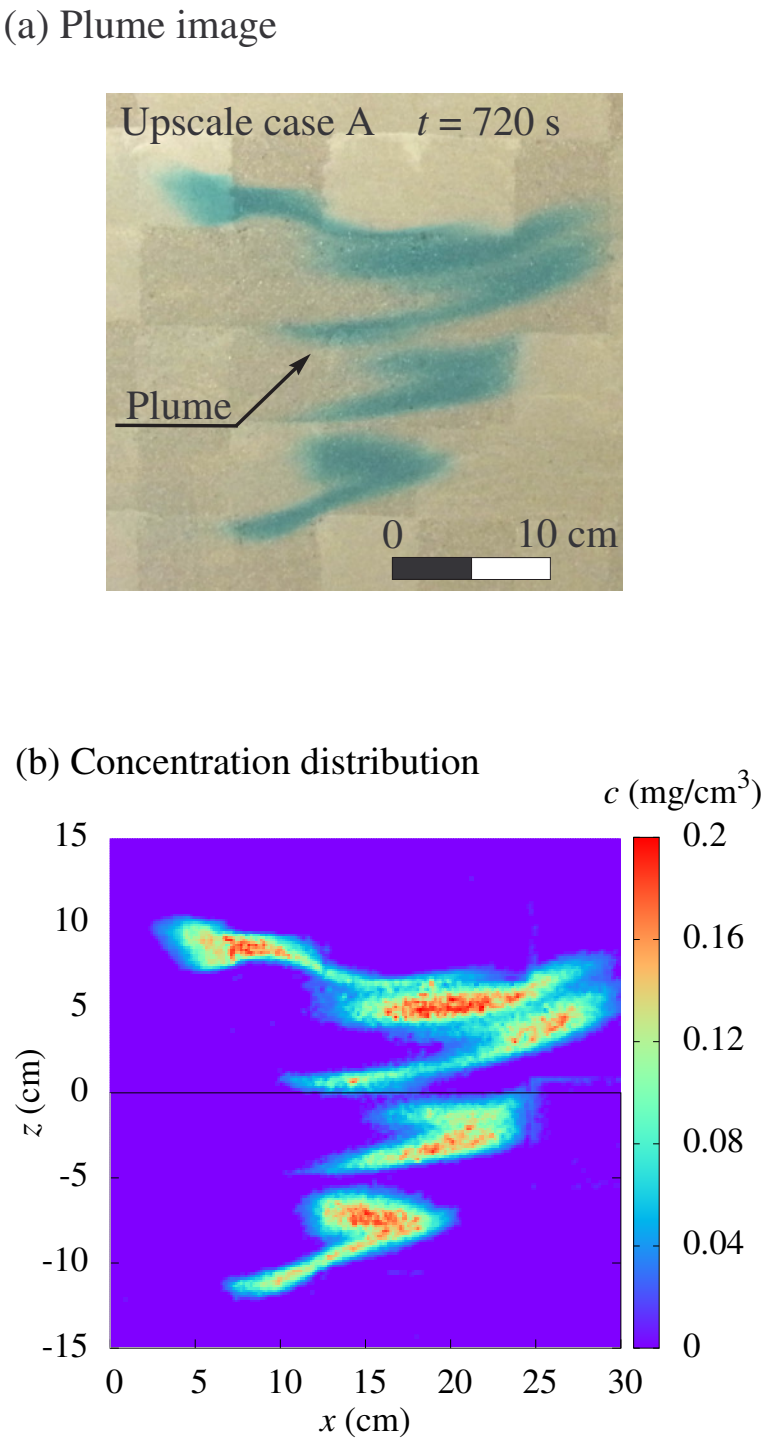

Figure 4.6: Comparison of image and concentration distribution from a line source. (a) Plume image and (b) concentration distribution.

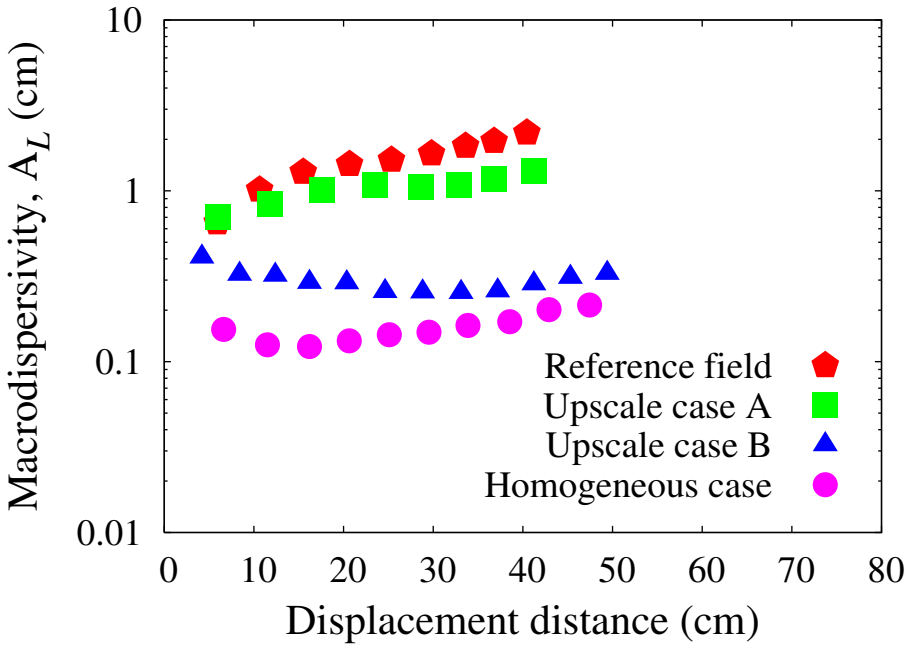

Figure 4.7: Longitudinal macrodispersivities obtained from the line source as a function of displacement distance for the Reference field and the upscaled models.

values for Upscale A and Upscale B. Thus, smoothing of the distribution of hydraulic conductivity due to upscaling reduces the longitudinal macrodispersivity.

For the point source from injection port c, images at a displacement distance of approximately 20 cm and the results of longitudinal macrodispersivity are presented in Figures 4.9 and 4.10, respectively. An interesting observation in Figure 4.10 is that the A_L values fluctuated with the displacement distance except for in the Homogeneous case. Compared with the solute plume from the line source, the solute plume from the point source was more affected by local heterogeneity, resulting in fluctuations in A_L. Since the loss of small-scale information by upscaling led to less local heterogeneity, for low-resolution cases (i.e., Upscale B and the Homogeneous case), fluctuations in A_L were smaller than those in high-resolution cases (i.e., Reference field and Upscale A).

4.3.2 Transverse Macrodispersivity

Figure 4.11 presents the transverse macrodispersivities obtained from the line and point sources as a function of the displacement distance for the Reference field and upscaled models. For the line source, in all of cases, the A_T values exhibited a similar trend of decreasing with the displacement distance. To explain this behavior, Figure 4.12

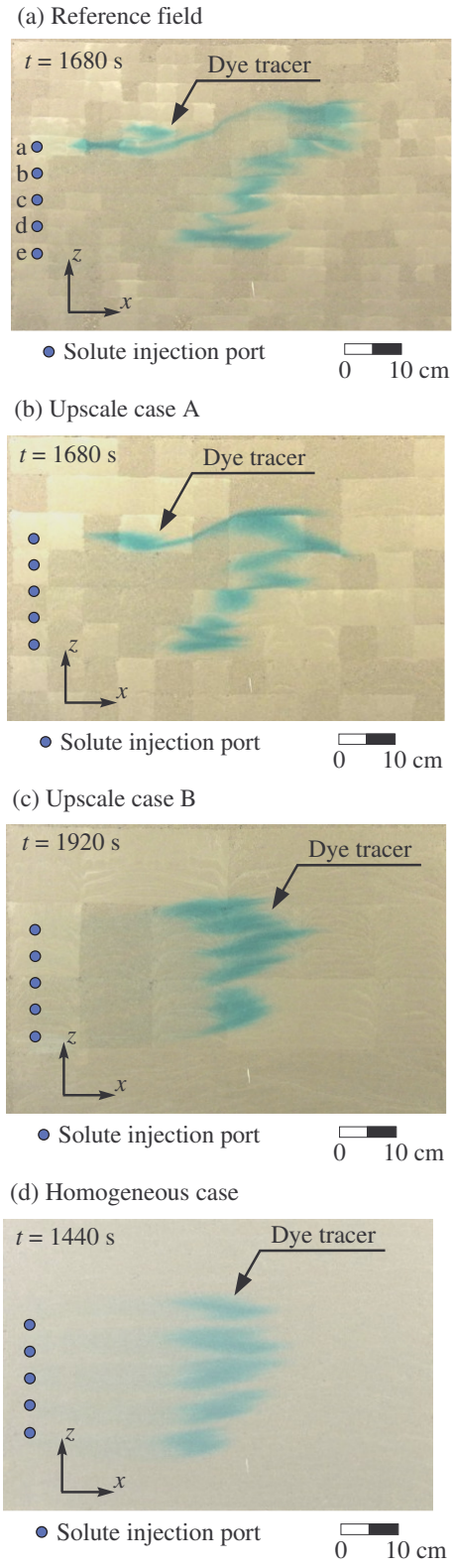

Figure 4.8: Images for the Reference field and three upscaled models from a line source at a displacement distance of approximately 33 cm. (a) Reference field, (b) Upscale A, (c) Upscale B, and (d) Homogeneous case.

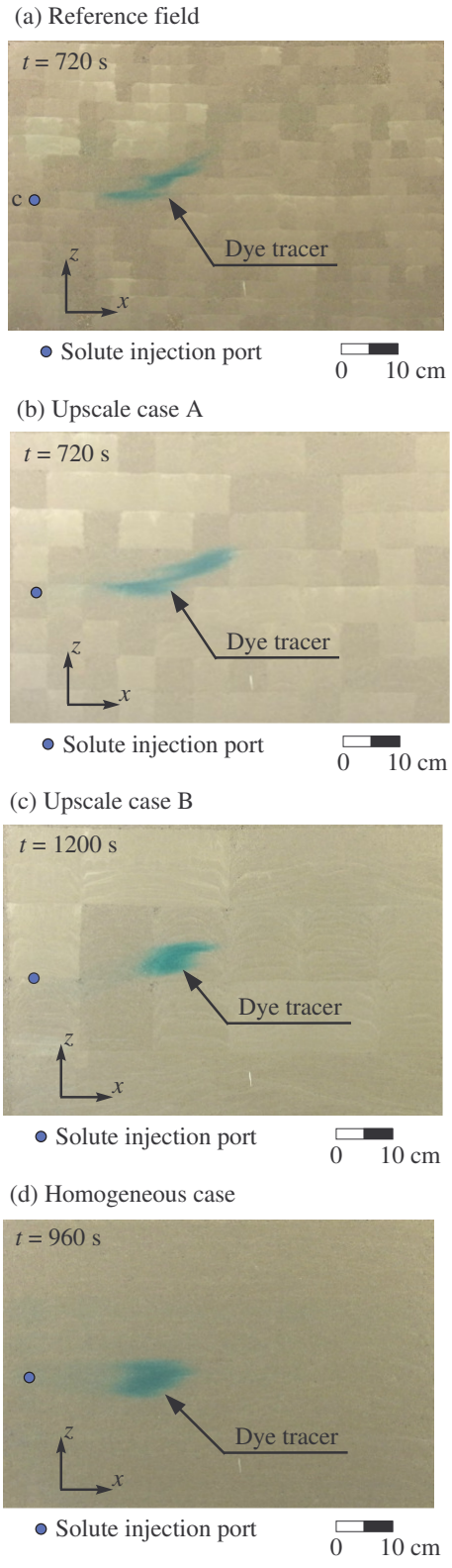

Figure 4.9: Images for the Reference field and three upscaled models from a point source (injection port c) at a displacement distance of approximately 33 cm. (a) Reference field, (b) Upscale A, (c) Upscale B, and (d) Homogeneous case.

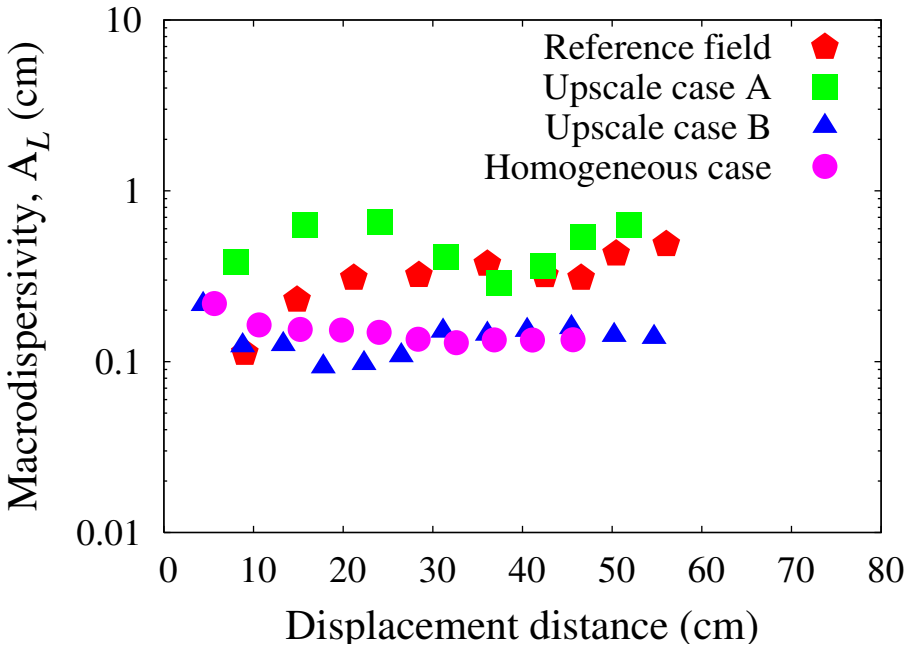

Figure 4.10: Longitudinal macrodispersivities obtained from a point source as a function of displacement distance for the Reference field and upscaled models.

depicts the spatial moment σ_{zz} from the line and point sources as a function of the displacement distance for the Reference field and upscaled models. The σ_{zz} values for the line source remained approximately constant at different displacement distances. Because the injection ports were aligned in the transverse direction (i.e., z-direction), the σ_{zz} values increased immediately after tracer injection. In contrast, compared with the longitudinal direction, velocity fluctuations in the transverse direction were relatively small and thus did not contribute significantly to σ_{zz}. As a result, σ_{zz} remained constant with distance. Therefore, estimates of A_T, which were calculated using equation (2.8), exhibited a decreasing trend.

In Figure 4.11, although the results of A_T from the point source for low-resolution cases (i.e., Upscale B and the Homogeneous case) were an order of magnitude smaller than those from the line source, they exhibited a similar decreasing trend with the displacement distance. In contrast, the estimates of A_T from the point source for high-resolution cases (i.e., Reference field and Upscale A) exhibited an increasing trend at distances between approximately 20 and 30 cm. As seen in Figure 4.9, which presents images of the solute plume at a displacement distance of 20 cm, the solute plume moved vertically in the positive z-direction except for in the Homogeneous case. Furthermore,

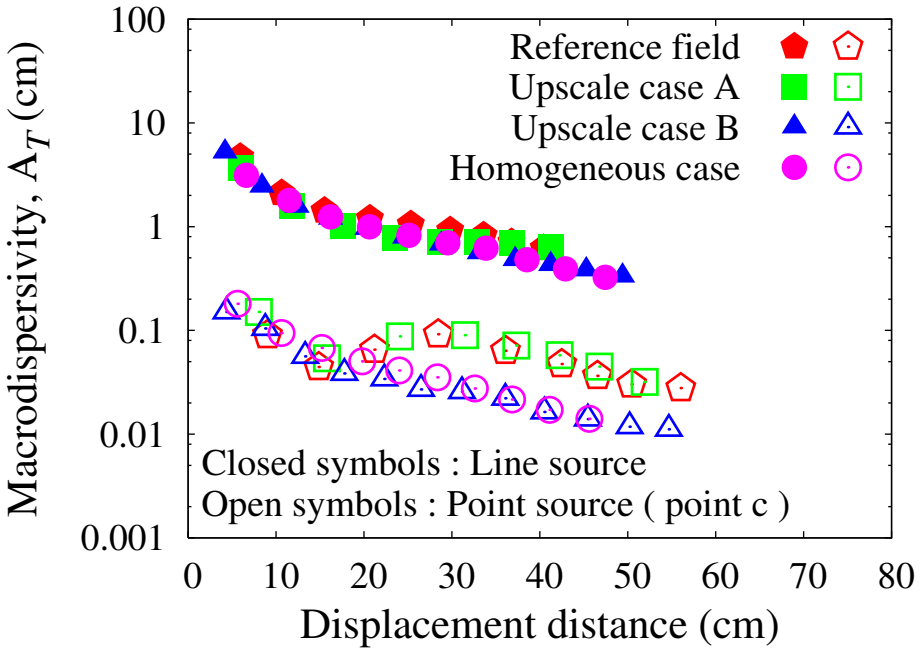

Figure 4.11: Transverse macrodispersivities obtained from line and point sources as a function of displacement distance for the Reference field and upscaled models.

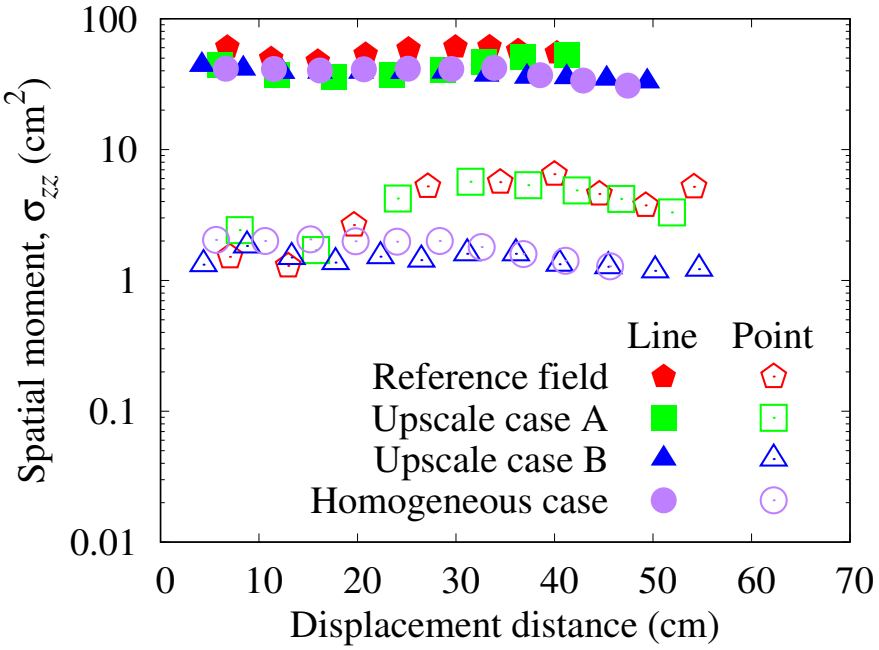

Figure 4.12: Spatial moment σ_{zz} from line and point sources as a function of displacement distance for the Reference field and upscaled models.

for the Reference field and Upscale A, the plume stretched due to local heterogeneity. Therefore, the spatial moment σ_{zz}, which represents the degree of solute spreading in the transverse direction, was relatively large at distances between approximately 20 and 30 cm, as can be seen in Figure 4.12, leading to the aforementioned relatively large A_T.

4.3.3 Ensemble Average of Transverse Macrodispersivity

As can be seen in Figure 4.11, for all cases, A_T values from the line source were approximately an order of magnitude larger than those from the point source. This is primarily due to the fact that five plumes were aligned in the transverse direction for the line source, whereas only a single port was used for the point source. Thus, tracer experiments using the line source led to an overestimation of the transverse macrodispersivity. Therefore, tracer experiments using small sources, such as a point source, may be ideal. However, a small tracer plume does not experience sufficient heterogeneity in the system; thus, the accuracy of the estimated results is not satisfactory. To solve this dilemma, we propose an ensemble averaging method, which consists of estimating the A_T value of each injection port (a–e) and averaging it for each displacement distance. Figure 4.13 presents a schematic diagram of the ensemble averaging method.

The results of transverse macrodispersivity estimated by the ensemble averaging method are presented in Figure 4.14 together with estimates from the point source of injection port c. Because there were no spatial fluctuations of the velocity in the Homogeneous case, we did not calculate the ensemble average; thus, only the result of the point source (injection port c) is displayed in the figure. The A_T values by ensemble averaging (see Figure 4.14) are approximately one order of magnitude smaller than those of the line source (see Figure 4.11). This result suggests that by using the ensemble averaging method, the effect of the spatial extent of the initial plume can be reduced. For Upscale B, A_T by ensemble averaging was similar to that from the point source (injection port c); however, for the Reference field and Upscale A, the fluctuations in A_T values were relatively small. While there were no significant differences in heterogeneity corresponding to the injection ports (a–e) for the low-resolution case (Upscale B), for high-resolution cases, such as the Reference field and Upscale A, the tracer plumes

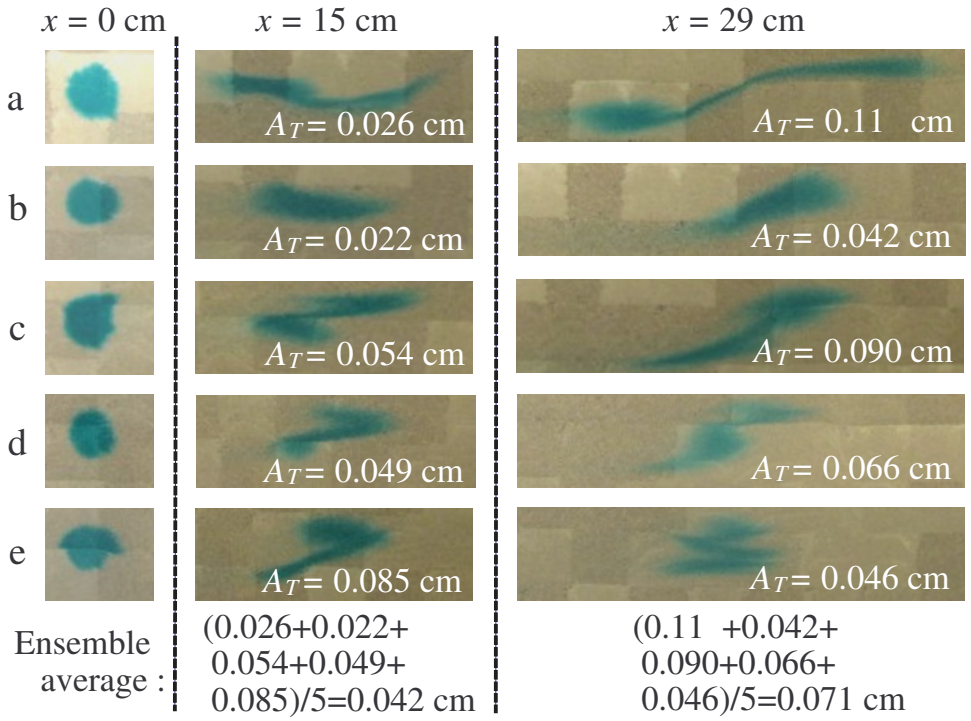

Figure 4.13: Schematic diagram of ensemble averaging method.

experienced different hydraulic conductivity fields depending on the injection port. By averaging the results of all injection ports, we can obtain estimates based on the overall structure of the K field, thereby reducing fluctuations in A_T.

4.3.4 Relationship Between Upscaling and Macrodispersivity

To further investigate the impact of upscaling on macrodispersivity, Figure 4.15 presents the relationship between the longitudinal and transverse macrodispersivities and heterogeneity. In this figure, A_L values corresponding to the maximal displacement distance from the line source are plotted. A_T values, which correspond to the maximal displacement distance obtained by ensemble averaging, are also plotted because they are relatively accurate compared with other values. It can be seen that for both A_L and A_T, the macrodispersivity decreased with decreasing heterogeneity (i.e., increased degree of upscaling). Thus, upscaling is closely related to the change in heterogeneity, which has been widely recognized as an important factor controlling solute dispersion (Gelhar and Axness, 1983; Fiori et al., 2010), resulting in changes in macrodispersivity. The values

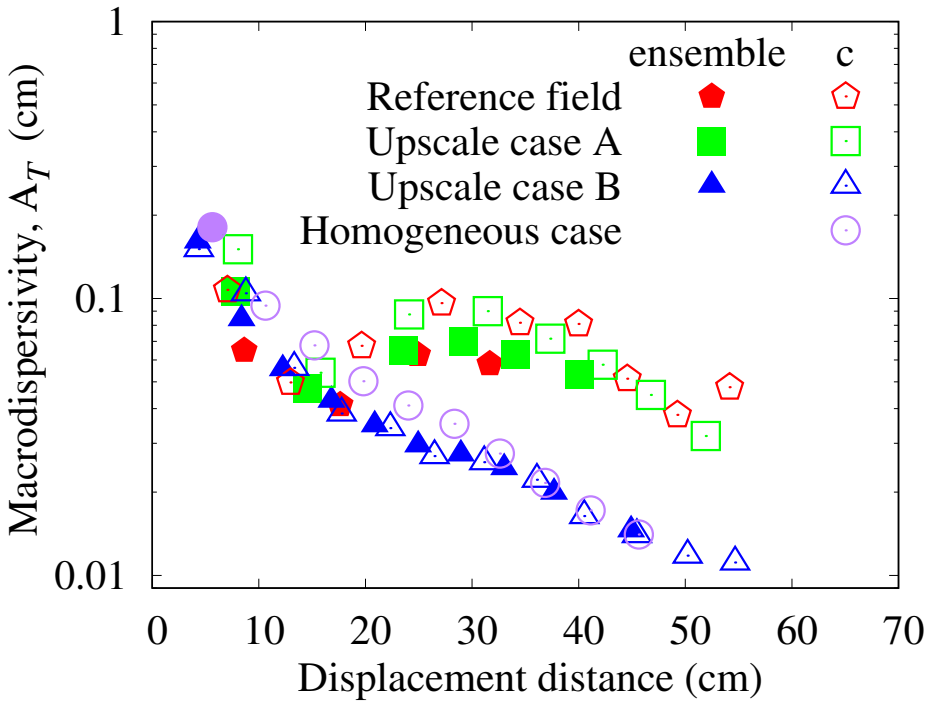

Figure 4.14: Results of transverse macrodispersivity estimated by the ensemble averaging method.

of longitudinal and transverse macrodispersivities obtained from laboratory-scale tracer experiments in the literature (Inoue et al., 2017; McNeil et al., 2006; Citarella et al., 2015; Greiner et al., 1997) are also plotted in Figure 4.15. The range of values in this study is in good agreement with values from previous studies obtained for similar heterogeneities.

Furthermore, the ratio of longitudinal to transverse macrodispersivity, A_L/A_T, was calculated using the A_L and A_T values in Figure 4.15. Table 4.2 displays the results of A_L/A_T. For the literature values, the ratio was only calculated when both the longitudinal and transverse macrodispersivities were reported. In addition, the range of A_L/A_T from field data reported by Gelhar et al. (1992) is presented in the table. Gelhar et al. (1992) accumulated dispersivity values from 59 different field sites and rated the data as having high, medium, or low reliability according to their criteria. Only dispersivities of high reliability are presented in Table 4.2.

As indicated in Table 4.2, in this study, A_L/A_T exhibits a decreasing trend with upscaling (i.e., reduced heterogeneity). There initially appears to be relationship between heterogeneity and A_L/A_T; however, although the heterogeneities of Inoue

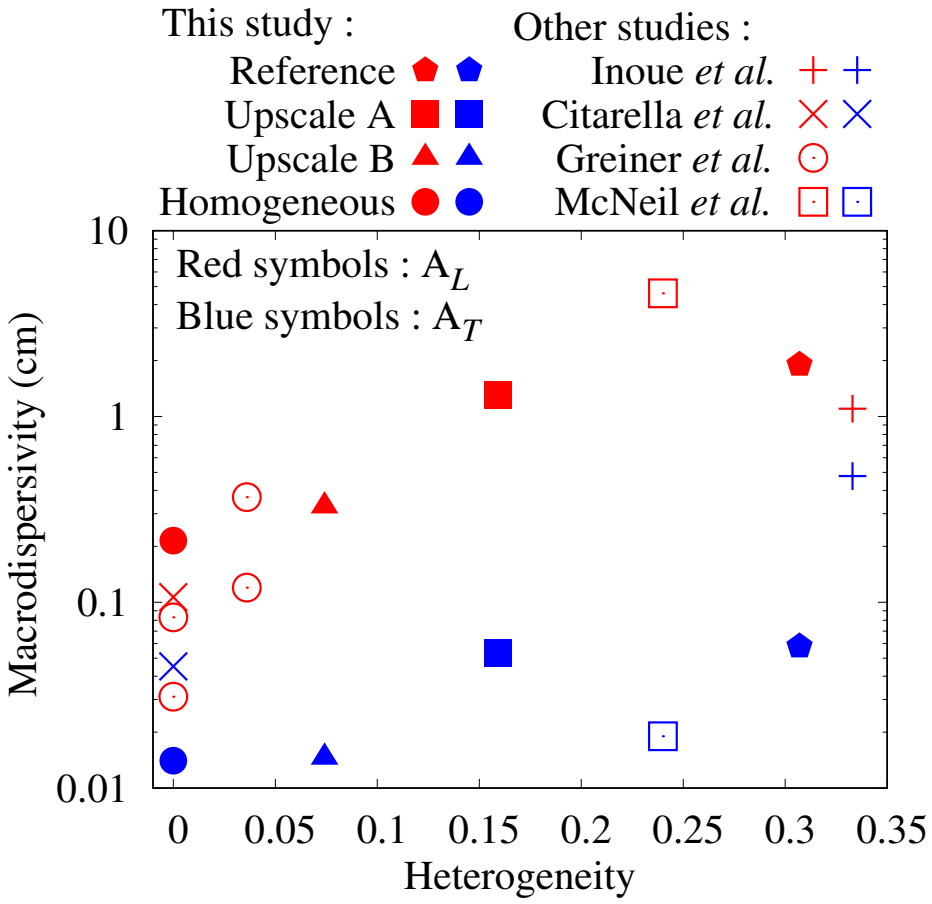

Figure 4.15: Longitudinal and transverse macrodispersivities versus heterogeneity.

Table 4.2: Ratio of longitudinal to transverse macrodispersivity (A_L/A_T) obtained in this study and previous studies.

	Heterogeneity	A_L/A_T
This study		
Reference field	0.307	32.8
Upscale A	0.159	24.6
Upscale B	0.0741	22.5
Homogeneous	0.0	15.3
Inoue et al. (2017)	0.333	2.30
Citarella et al. (2015)	0.0	2.36
McNeil et al. (2006)	0.24	242
Gelhar et al. (1992)	–	10–640

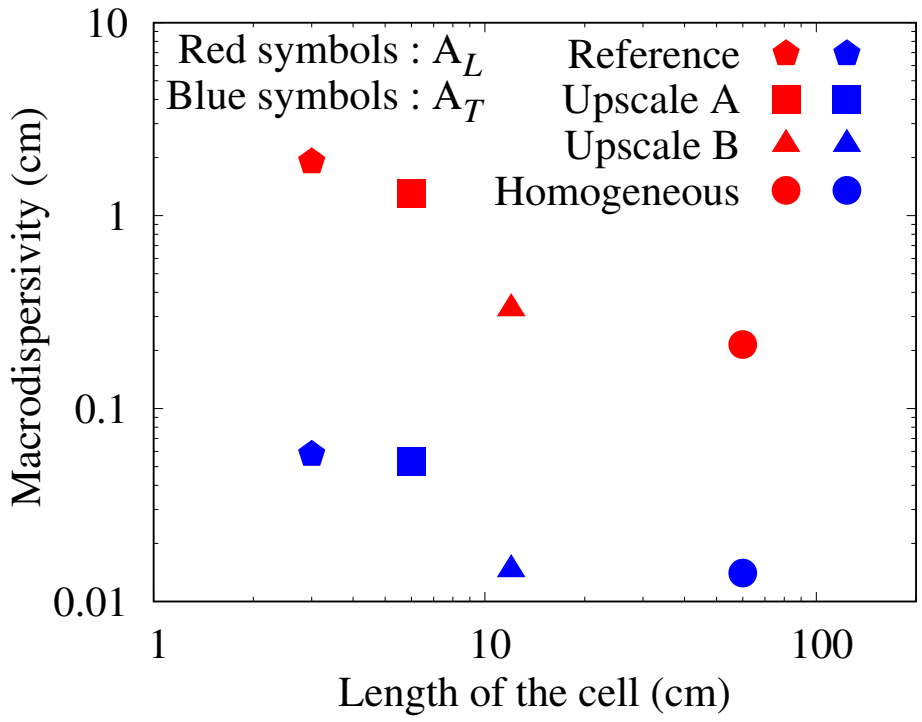

Figure 4.16: Longitudinal and transverse macrodispersivities versus length of the cell.

et al. (2017) and Citarella et al. (2015) are very different, the A_L/A_T values do not differ significantly. The results of Gelhar et al. (1992) also indicate that A_L/A_T values vary within a wide range. This suggests that the A_L/A_T value is affected by not only heterogeneity but also other factors. Further investigation is necessary to evaluate the dependency of the ratio of longitudinal to transverse macrodispersivity on other factors, such as the displacement distance and tracer injection conditions.

Here, we focus on the relationship between the macrodispersivity and the resolution of the hydraulic conductivity distribution. Figure 4.16 displays the relationship between the longitudinal and transverse macrodispersivities and the length of the cell. Because the size of the cells for the Homogeneous case was 72 cm $\times$ 48 cm (not square), the average length of the sides, which is equal to 60 cm, was selected. It can be seen that the values of A_L and A_T did not differ significantly between the Reference field and Upscale A. However, the values of A_L and A_T differed significantly between the Reference field and lower-resolution cases (i.e., Upscale B and the Homogeneous case). The correlation scale of the Reference field was set to 6 cm, which is equal to length of the cell for Upscale

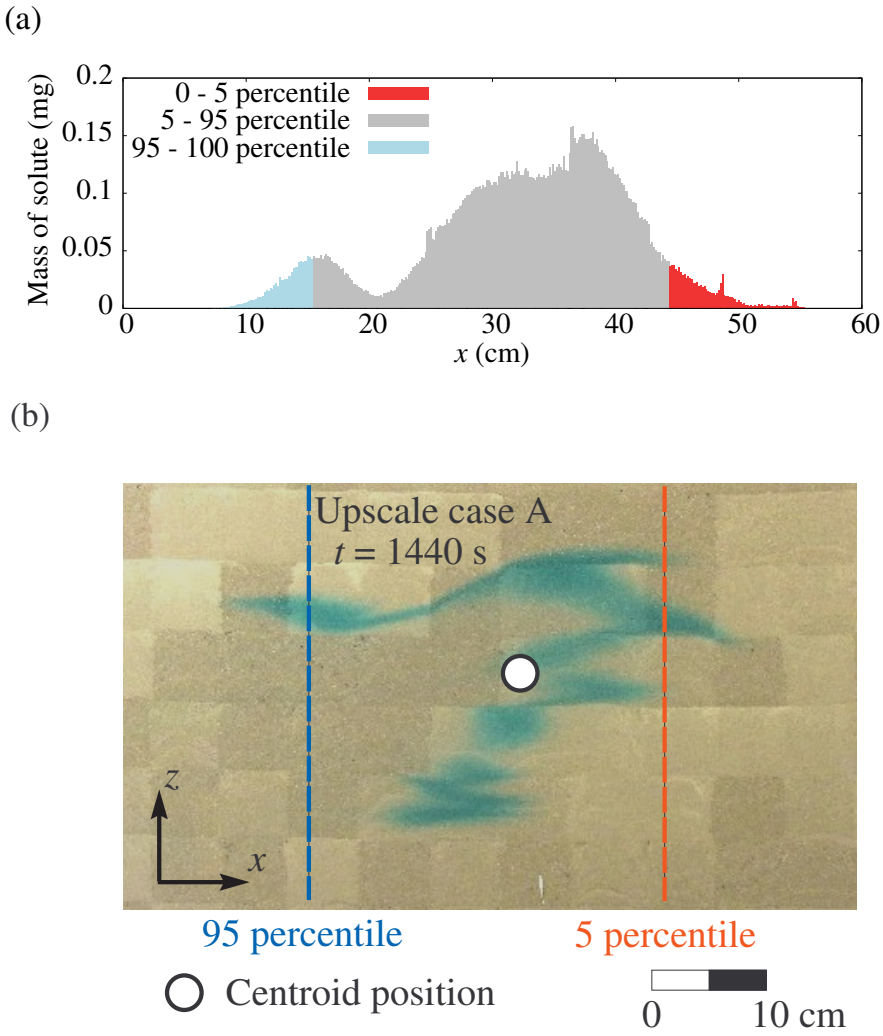

Figure 4.17: Schematic diagram of the forward and backward tails of a tracer plume. (a) Histogram of solute mass on the x-axis, (b) image of solute distribution.

A. These results suggest that when length of the cell is greater than the correlation scale of the Reference field, the macrodispersivities are largely underestimated.

4.3.5 Forward and Backward Tails

In this chapter, we estimate the forward and backward tails of a tracer plume using the same methodology applied in Section 2.3.4. A schematic diagram of forward and backward tails is presented in Figure 4.17. Figure 4.18 also displays the results of the calculated forward and backward tails.

The width of the gray region tends to decrease with a decreased resolution by upscaling. This signifies that the spatial extent of the plume in the longitudinal

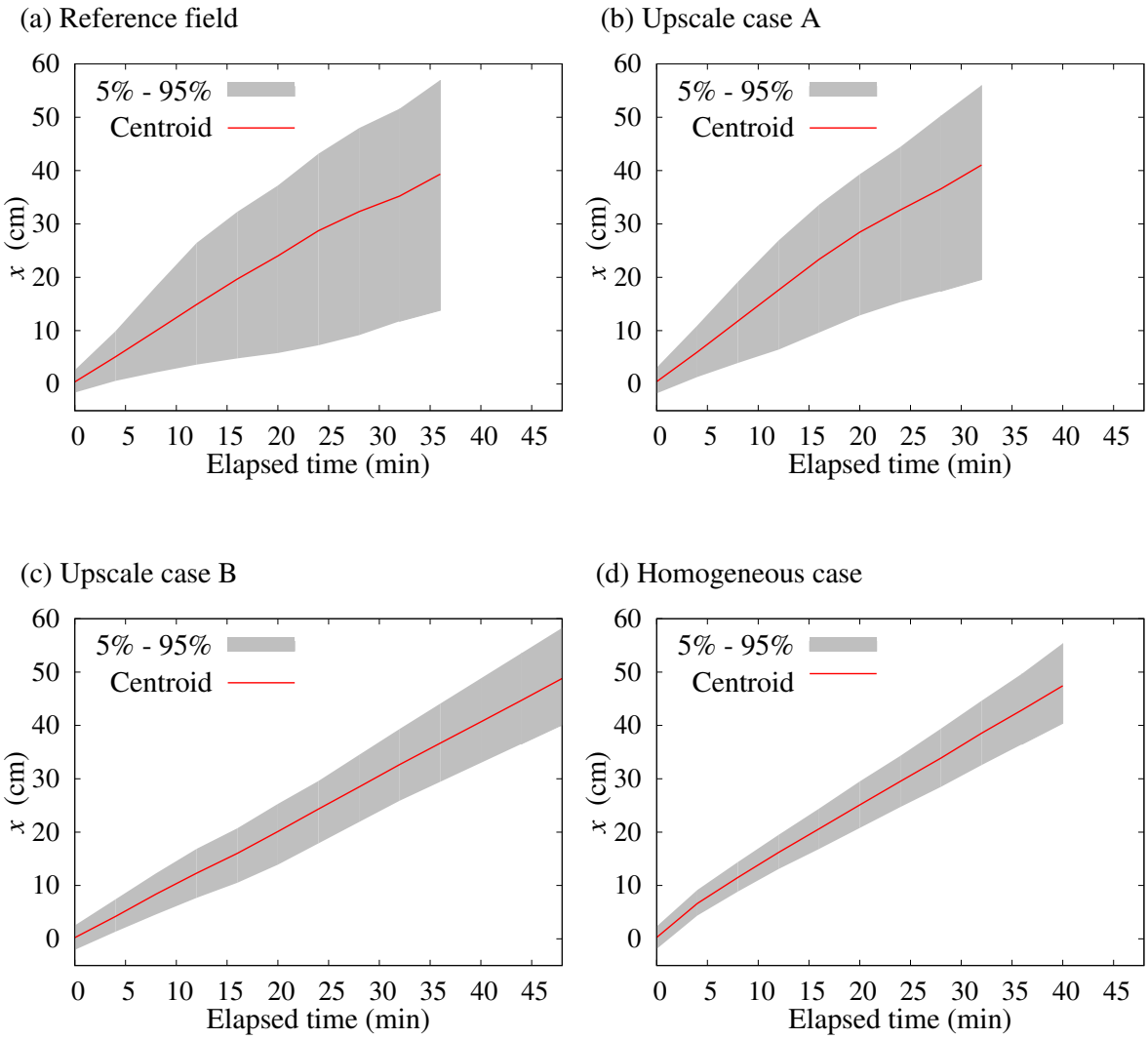

Figure 4.18: Results of forward and backward tails. (a) Reference field, (b) Upscale A, (c) Upscale B, (d) Homogeneous case. Red solid lines indicate the centroid locations of the solute plume, while gray regions denote x_{05}–x_{95}.

direction is underestimated after upscaling. In particular, there is a distinct difference between Upscale A and Upscale B, which is in agreement with the aforementioned findings in terms of macrodispersivities.

4.4 Conclusions

This chapter presented a study that investigated the effect of upscaling on solute dispersion in two-dimensional heterogeneous porous media. Laboratory-scale tracer experiments were conducted in a two-dimensional flow tank using line and point sources.

In addition, the degree of dispersion was quantified using a visualization technique. This study provided the following conclusions:

1. For a line source, the reduced heterogeneity due to upscaling reduced the longitudinal macrodispersivity. In addition, for a point source, the fluctuation of the longitudinal macrodispersivity was larger than that for a line source. This is because a small plume, such as that caused by a point source, is more affected by local heterogeneity.

2. In all cases, the transverse macrodispersivity exhibited a similar trend of decreasing with increasing the displacement distance. We suspect that tracer injection from the line source led to overestimation of the transverse macrodispersivity. To accurately evaluate the transverse dispersion, the ensemble averaging method was proposed. The estimates obtained by ensemble averaging were an order of magnitude smaller than the values obtained by the line source.

3. The relationship between the macrodispersivity and the length of the cell for porous formations indicated that when the length of the cell was greater than the correlation scale of the Reference field, the macrodispersivity was largely underestimated.

4. As in Chapter 3, we estimated the forward and backward tails of a tracer plume. The results indicated that the distance between the forward and backward tails (i.e., solute spreading) tended to decrease with decreasing resolution by upscaling.

5

Evaluation of Transport Parameters in a Ryukyu Limestone Aquifer

Contents

5.1 Introduction

Water shortages frequently occur on atoll islands located in Pacific Island countries because the islands often consist of limestone aquifers with high permeability such that precipitation rapidly infiltrates into the underground reservoirs. Moreover, the rise in sea level and changes in rainfall patterns caused by global warming may reduce

the volume of freshwater in the underground reservoirs of such islands. As a result, subsurface dams are planned and constructed to store and control groundwater for effective use and to ensure consistent extraction of freshwater by preventing the intrusion of seawater into coastal aquifers.

The success of subsurface dam projects depends on the detailed understanding of the physical nature of limestone aquifers, including the groundwater flow characteristics and porosity. Previous studies investigated the physical characteristics (e.g., compressive strength and pore structure) of Ryukyu limestone, which is widely distributed in islands in the southwest region of Japan (Kogure et al., 2005; Masuoka and Nakaya, 2021). Nakaya et al. (2018) measured the groundwater flow velocity and direction with a GFD3 (AREC) single-hole groundwater velocimeter using heat flow, which is commonly used in the evaluation of groundwater velocity in Japan. Other researchers also developed a measurement technique using the ultrasonic echo reflected from solid particle tracers suspended in groundwater, which makes it possible to measure a wide range of groundwater velocities (Saito et al., 2006; Toida et al., 2007). This technique enables the measurement of flow velocity even if the magnitude of the velocity is extremely low, such as in deep geological environments.

The above-mentioned techniques generally require expensive devices and an electric power source and are consequently difficult to implement. However, for large-scale field studies, a large number of observation wells are often utilized; therefore, low-cost and simple methods are typically preferred. To respond to this demand, Yamamoto et al. (2016) developed a single dot type paper disk groundwater velocimeter. This method is low-cost and easy to implement; however, only the shallow part of an aquifer can be measured. Therefore, this method cannot be used to measure groundwater velocity in deep sections of an aquifer.

In this chapter, we focus on single-borehole dilution tests (SBDTs), which are methods for evaluating transport parameters, including groundwater velocity and dispersivity, using wells or boreholes. These methods are based on tracer injection into the saturated zone and observation of the concentration over depth and time. SBDTs require little equipment and effort and thus have been widely used to estimate groundwater velocity. Maurice et al. (2012) and Yang et al. (2019) utilized SBDTs

to obtain the horizontal velocity in natural karst aquifers. In addition, Miller et al. (2018) and Montgomery et al. (2020) used SBDTs to measure the specific discharge of a firn aquifer in southeast Greenland and Antarctica, respectively. SBDTs were also used to evaluate the soundness of civil engineering structures. For example, Dong et al. (2016) investigated the leakage pathways of an earth-rockfill dam, while Andrade et al. (2017) used SBDTs to estimate seepage from a canal. In addition, Nakagawa et al. (2018) used SBDTs to evaluate the pore velocity, hydraulic conductivity, and dispersion coefficient at a nitrate pollution site.

Although there have been many practical applications of SBDTs, as mentioned above, to the best of our knowledge, there have been few studies on their validity. Fahrmeier et al. (2021) compared the results of SBDTs using different injection methods, such as the hosepipe method and permeable injection bag method, and found that both methods produced similar velocity profiles for wells of karst and alluvial aquifers. Gomo (2020) also evaluated the effect of molecular diffusion and density current on the estimation of groundwater velocity. Studies on their validity are, however, insufficient. Additionally, although many studies were conducted for karst aquifers, it is important to test the applicability of SBDTs to estimate the flow velocity for other types of aquifers.

As described in this chapter, by using SBDTs, we estimated the transport parameters, including the horizontal groundwater velocity (Darcy velocity) and dispersivity, of a Ryukyu limestone aquifer where the construction of a subsurface dam is planned. Then, by comparing the Darcy velocities estimated from the SBDTs and the ambient hydraulic gradient of the aquifer, the validity of the SBDTs was verified. Additionally, 93 core samples of Ryukyu limestone at the field were collected, and the porosity, which is important for determining the water storage capacity of a subsurface dam, was determined using the Archimedes buoyancy method.

5.2 Site Description

The test site was located southwest of Kikai Island in Japan. Figure 5.1 displays the location of the test site together with the cluster of wells installed. The Ryukyu limestone terrace in the study area, which overlaid the basement mudstone of the Shimajiri Group, was extensively distributed. The Shimajiri mudstone layer had an

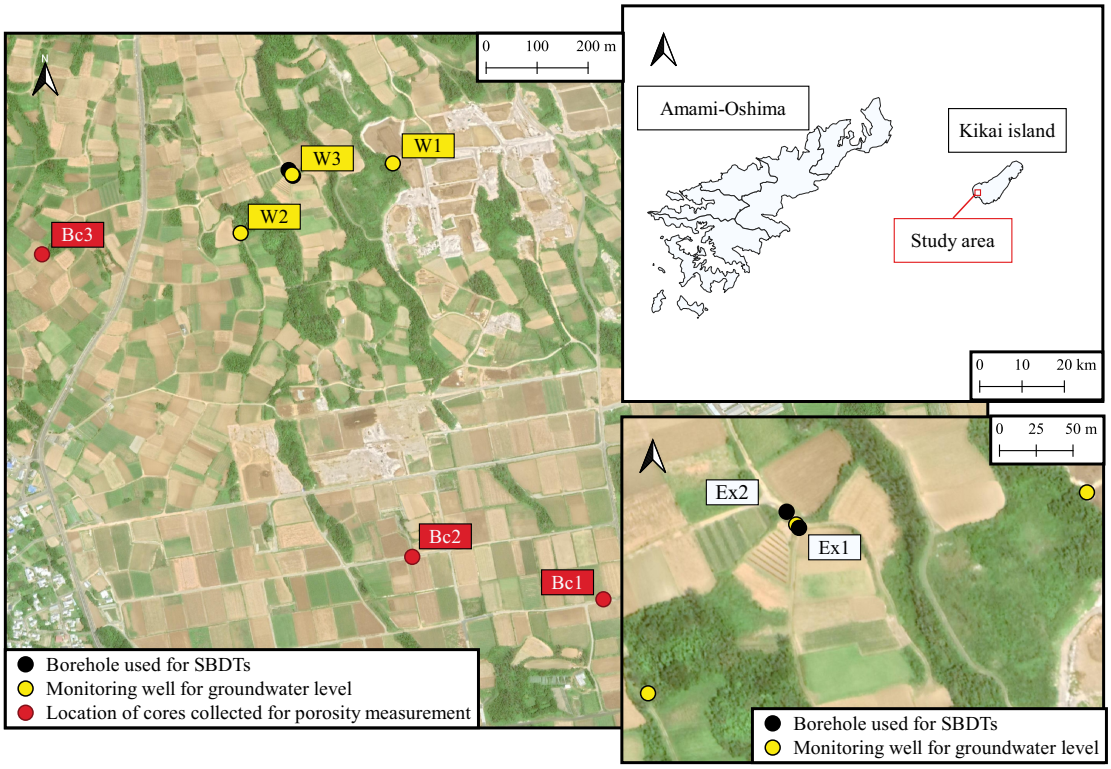

Figure 5.1: Location of test site on Kikai Island together with a cluster of wells.

impermeable basement, and the Ryukyu limestone layer, which was approximately 20 m thick, served as an aquifer. Two boreholes labeled Ex1 and Ex2 (see Figure 5.1) were employed to conduct the SBDTs. These boreholes were separated by a distance of only approximately 15 m. At the three boreholes labeled W1, W2, and W3, the groundwater level was observed over a one-month period between April 21, 2018 and May 21, 2018. Figure 5.2 presents the results of the groundwater level for W1, W2, and W3. It can be seen that in all boreholes, the groundwater level fluctuated with time, whereas the relative difference in groundwater level between the boreholes did not significantly change over time. This suggests that temporal changes in the hydraulic gradient in the field are relatively small. Moreover, at the three boreholes labeled Bc1, Bc2, and Bc3, 93 core samples of Ryukyu limestone were collected to estimate the porosity using the Archimedes buoyancy method, which is described later.

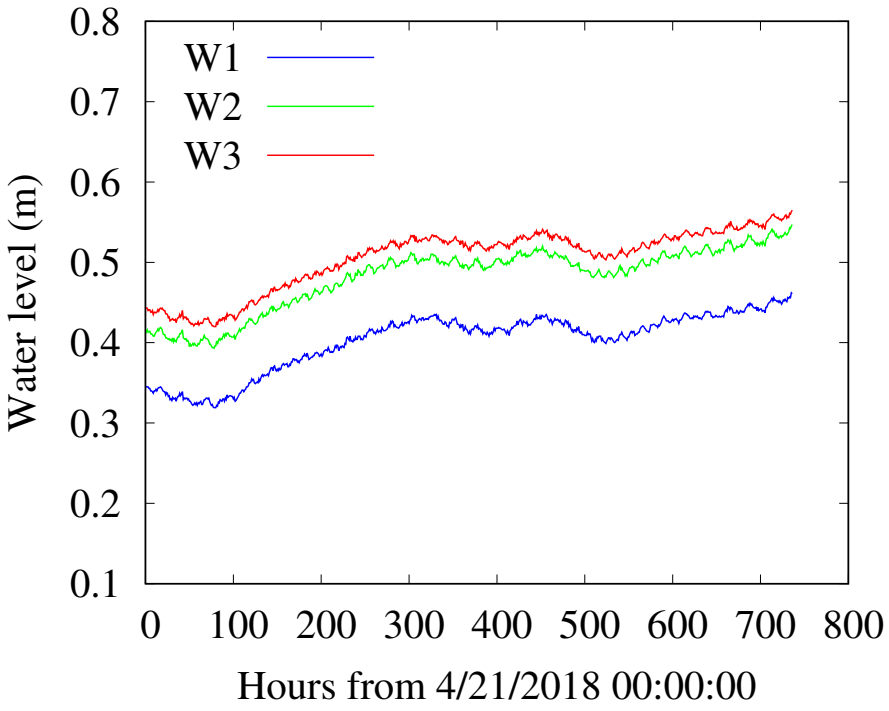

Figure 5.2: Groundwater level for boreholes W1, W2, and W3 over a one-month period between April 21, 2018 and May 21, 2018.

5.3 Single-Borehole Dilution Tests (SBDTs)

5.3.1 Design of Dilution Tests

A schematic diagram of the borehole design and geological logs for Ex1 and Ex2 is presented in Figure 5.3. As can be seen in the figure, for both boreholes, dune sand and Ryukyu limestone layers existed at depths of approximately > 12 m and $\leqq 12$ m, respectively, above sea level. The borehole casing was screened at depths from 1.0 m to -10 m above sea level, which were selected as the experimental interval of the SBDTs. Table 5.1 presents the specifications for the boreholes and experimental cases. The radius and opening ratio of Ex1 were four times greater and nearly three times greater than those of Ex2, respectively. For Ex1, there was also gravel pack in the borehole annulus. The experiment was repeated for each borehole to test reproducibility (i.e., three times for Ex1 and twice for Ex2). In the experiments, sodium chloride (NaCl) was used as a tracer (Nakagawa et al., 2018; Poulsen et al., 2019; Williams et al., 2006).

First, permeable bags with a given mass (see Table 5.1) of NaCl were attached to a rope every 1 m. Upward and downward movements of the rope with the permeable

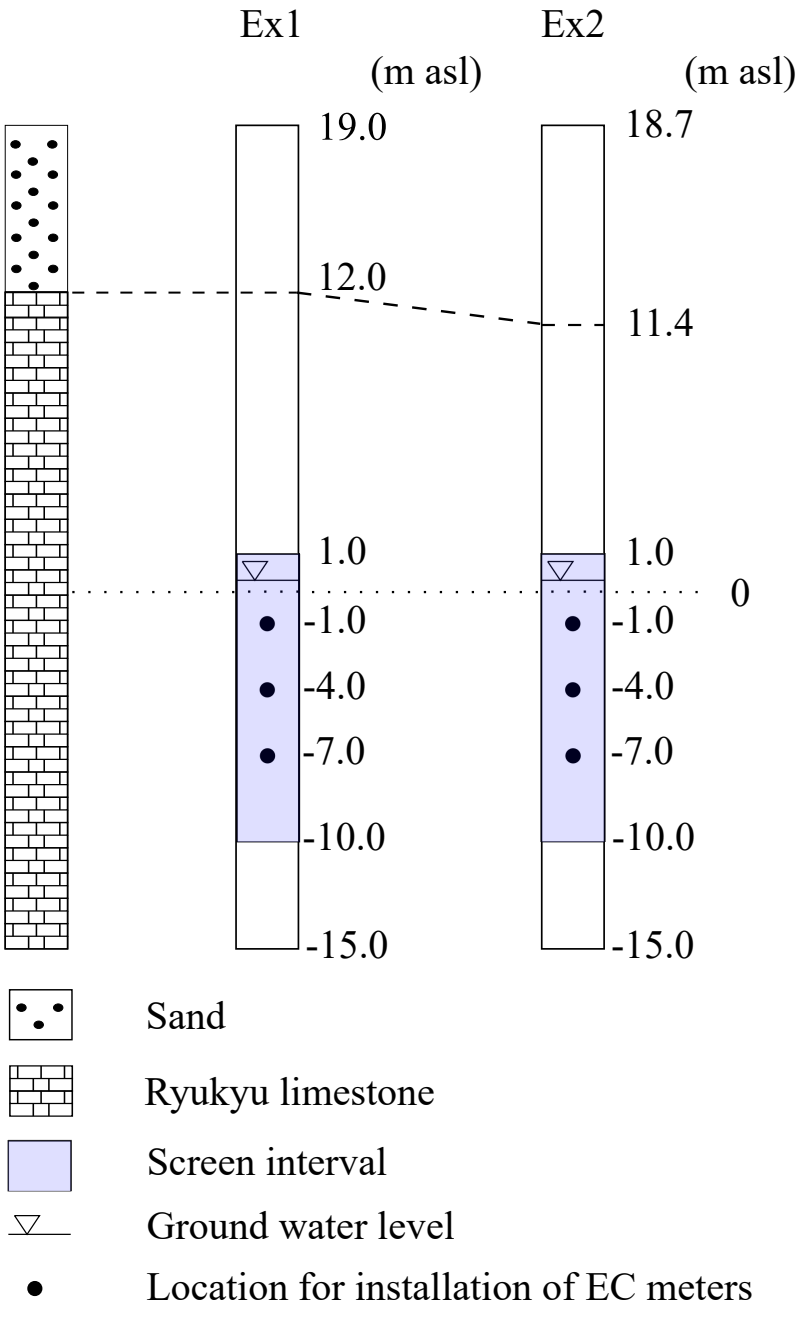

Figure 5.3: Borehole design and geological logs for boreholes Ex1 and Ex2.

Table 5.1: Specifications for boreholes and experimental cases.

Borehole	Radius of borehole (cm)	Opening ratio (%)	NaCl mass per bag (g)	Dissolution time (s)	Date	No. of tests
Ex1	10	30	90	600	Aug. 3, 2020	Ex1-1
···	···	···	···	···	Nov. 29, 2020	Ex1-2
···	···	···	···	···	May 22, 2021	Ex1-3
Ex2	2.5	9.8	5.6	180	Dec. 27, 2020	Ex2-1
···	···	···	···	···	May 23, 2021	Ex2-2

bags throughout the whole saturated length were repeated during a given time (see Table 5.1). By moving the bags at a constant speed, uniform distribution of NaCl concentration was achieved. After dilution of NaCl, electrical conductivity meters (HOBO U24-002, USA) were installed −1.0 m, −4.0 m, and −7.0 m above sea level (depicted in Figure 5.3 as black dots). The resulting breakthrough curves (BTCs) of the electrical conductivity were then converted to those of the NaCl concentration by using the calibration curve presented in Figure 5.4.

5.3.2 Estimation of Darcy Velocity

The dilution of a tracer in an interval with constant volume can be described as follows (Freeze and Cherry, 1979):

$$\frac{dC}{dt} = -\frac{A|v_a|C}{W}, \tag{5.1}$$

where dC/dt is the decrease in tracer concentration with time, C is the tracer concentration, A is the cross-sectional area of the dilution volume perpendicular to the flow, v_a is the apparent Darcy velocity, and W is the volume of the interval in which the dilution occurs. Rearrangement and integration lead to equation (5.2) (Freeze and Cherry, 1979):

$$\ln C = -\left(\frac{A|v_a|}{W}\right)t + \ln C_0, \tag{5.2}$$

where C_0 is the initial tracer concentration at $t = 0$. The length of the interval and radius of the borehole are defined as L and R, respectively, and A and W are then expressed as $A = 2RL$ and $W = \pi R^2 L$.

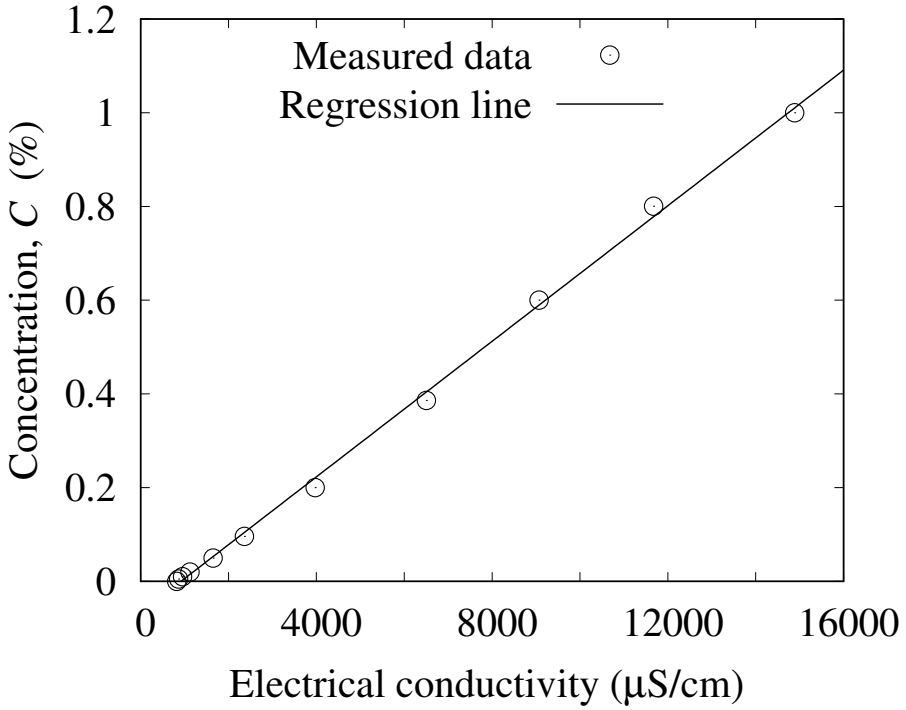

Figure 5.4: Calibration curve of NaCl concentration versus electrical conductivity.

Using these expressions, we can obtain equation (5.3) as follows (Bernstein et al., 2007; Pitrak et al., 2007):

$$\ln\left(\frac{C}{C_0}\right) = -\left(\frac{2|v_a|}{\pi R}\right)t. \tag{5.3}$$

In the experiments, only v_a was an unknown parameter; therefore, using equation (5.3) and the breakthrough curves obtained from the SBDTs, $|v_a|$ could be estimated by linear least-squares minimization using standard optimization techniques (i.e., fitting). However, flow field distortion was caused by the physical interference of the borehole, resulting in overestimation of the Darcy velocity. Thus, we used the borehole distortion factor α to compensate for the overestimation of the Darcy velocity as follows:

$$|v| = \frac{|v_a|}{\alpha}, \tag{5.4}$$

where α is commonly approximated to 2 to interpret SBDTs (Dong et al., 2016; Miller et al., 2018; Novakowski et al., 2006; Pitrak et al., 2007).

5.3.3 Data Processing

The breakthrough curve obtained from an elevation of −7.0 m for Ex1-1 is presented in Figure 5.5(a). Here, t' is the time after the tracer application, and C'_0 is the tracer concentration at $t' = 0$. As can be seen from equation (5.3), for SBDTs, the natural log of the relative concentration decreases linearly with time in theory. However, $\ln C/C'_0$ of the measured breakthrough curve (see Figure 5.5(a)) initially tended to decrease significantly, but later gradually approached a linear decreasing trend. Thus, at small times, $\ln C/C'_0$ exhibited a nonlinear trend, which is in disagreement with equation (5.3). According to Gomo (2020), this behavior of $\ln C/C'_0$ is due to the effect of tracer density convection and molecular diffusion. Therefore, using the nonlinear portion of the concentration data for fitting may lead to overestimation of the Darcy velocity. As can be seen in Figure 5.5(a), after $t' = 7200$, $\ln C/C'_0$ exhibited an approximately linear decreasing trend; therefore, $\ln C/C'_0$ values before $t' = 7200$ were excluded, and only data after $t' = 7200$ are displayed in Figure 5.5(b). Here, the horizontal and vertical axes display the time t ($t = t' - 7200$) and concentration at time $t = 0$. We used the same procedure for the data from other experiments, and the Darcy velocities at the three points (see Figure 5.3) were estimated.

5.3.4 Measurement of Porosity

we estimated the porosity of 93 core samples of Ryukyu limestone collected at three boreholes (Bc1, Bc2, and Bc3). Figure 5.6 presents an example of the Ryukyu limestone samples. The porosity of rock samples is usually measured by the Archimedes buoyancy method. In this method, three quantities, namely, the weight of a saturated sample suspended and fully immersed in water (M_1), the weight of a sample fully saturated with water in air (M_2), and the weight of a dry sample (M_3), are measured for a single sample. From these quantities, the bulk density ρ_b, solid density ρ_s, and porosity n can be calculated by the following equations:

$$\rho_b = \frac{M_1 \rho_w}{M_2 - M_3}, \tag{5.5}$$

$$\rho_s = \frac{M_1 \rho_w}{M_1 - M_3}, \tag{5.6}$$

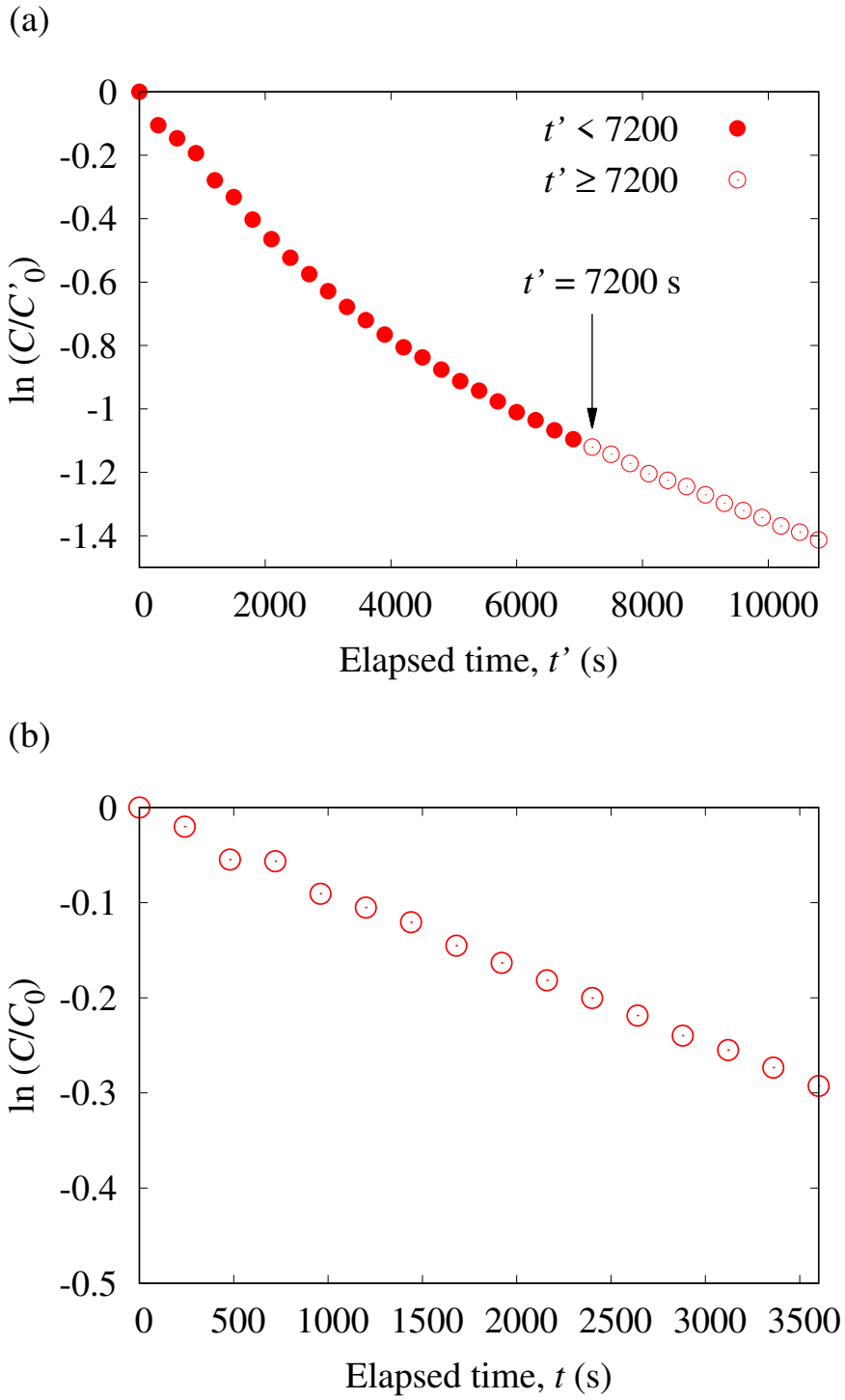

Figure 5.5: Breakthrough curve obtained from an elevation of −7.0 m for test Ex1-1. (a) All data, (b) data after 7200 s.

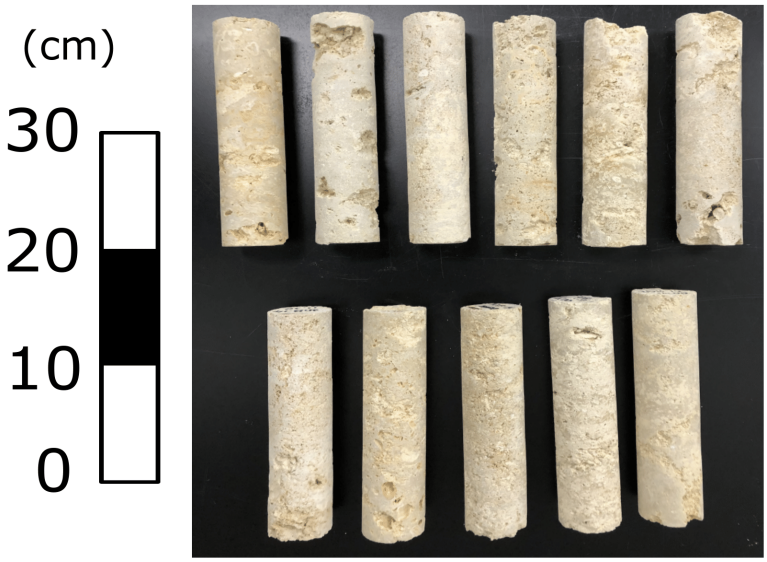

Figure 5.6: Example of Ryukyu limestone samples.

$$n = \frac{M_2 - M_3}{M_1 - M_3}, \tag{5.7}$$

where ρ_w is the density of water.

5.4 Results and Discussion

5.4.1 Estimation of Darcy Velocity from the Hydraulic Gradient and Hydraulic Conductivity in the Field

To verify the reliability of SBDTs, we compared the results of the SBDTs with the results obtained by another method based on Darcy's law. To use Darcy's law, the required quantities are the hydraulic gradient and hydraulic conductivity in the field. First, we assumed that the groundwater level is represented by the plane depicted in Figure 5.7 to estimate the hydraulic gradient. The equation of a plane is as follows:

$$ax + by + cz + d = 0, \tag{5.8}$$

where, if the plane represents a groundwater table, x and y are the horizontal coordinates defining the location of a borehole, and z is the groundwater table elevation. If the coordinates of the three points (i.e., W1, W2, and W3) are known, then the coefficients a, b, c, and d, can be determined. The hydraulic gradient vector can then be calculated as

$$\mathbf{i} = \left(\frac{\partial z}{\partial x}, \frac{\partial z}{\partial y}\right). \tag{5.9}$$

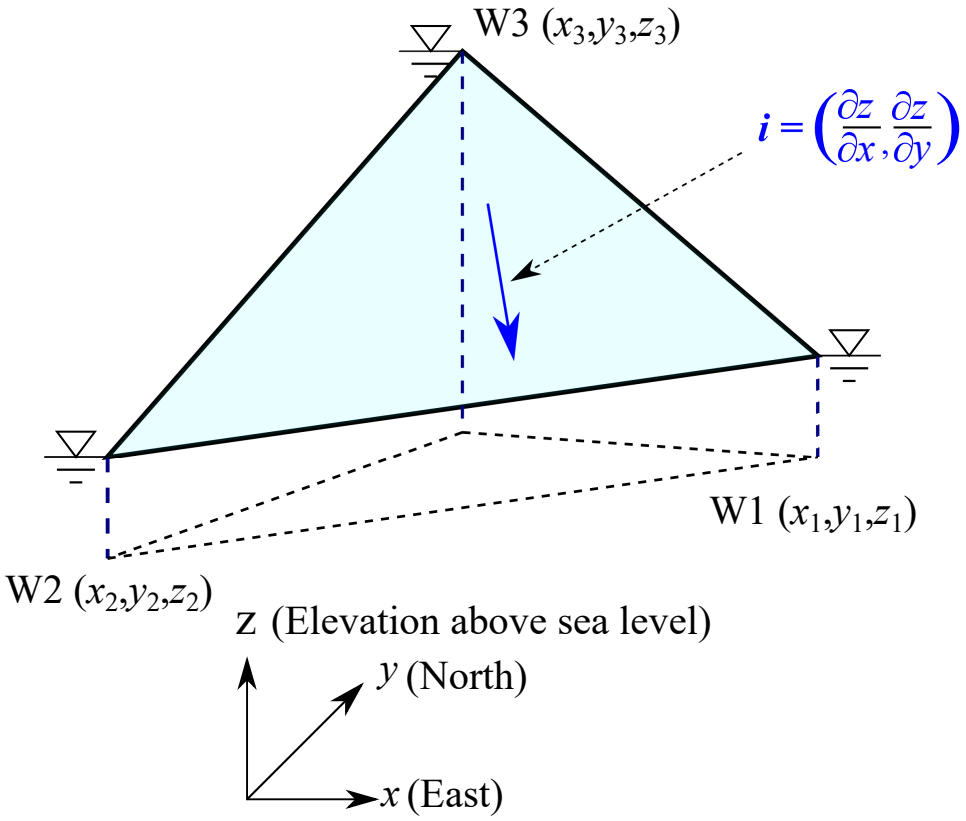

Figure 5.7: Method for calculating the hydraulic gradient. x and y are the horizontal coordinates (East and North, respectively) defining the location of a borehole, and z is the groundwater table elevation.

The horizontal Darcy velocities in the x- and y-directions are calculated as follows (Bear and Verruijt, 1987):

$$v_x = -K\frac{\partial z}{\partial x}, \tag{5.10}$$

$$, v_y = -K\frac{\partial z}{\partial x}, \tag{5.11}$$

where K is the hydraulic conductivity, which is assumed to be isotropic. The magnitude of the Darcy velocity can then be estimated as

$$|v| = \sqrt{v_x^2 + v_y^2}. \tag{5.12}$$

Table 5.2 presents the groundwater level (z) at three boreholes, W1, W2, and W3. Here, the origin (i.e., $(x, y) = (0, 0)$) is at (33°0′0E, 129°30′0N). We also used the average values over a one-month period between April 21, 2018 and May 21, 2018 (see Figure 5.2) as the groundwater level z. A pumping test was conducted in the field

Table 5.2: Groundwater level at boreholes W1, W2, and W3.

Borehole	x (m)	y (m)	z (m)
W1	42173.02	−520112.87	0.402
W2	41874.76	−520267.86	0.481
W3	41975.59	−520138.44	0.504

Table 5.3: Results of the pumping test.

Borehole	Horizontal distance between pumping and observation wells	Groundwater level under steady-state conditions
W3	$r_1 = 2.97$	$h_1 = 24.42$
Ex2	$r_2 = 15.0$	$h_2 = 24.46$

(pumping in Ex1 and observation in W3 and Ex2), and the hydraulic conductivity K was estimated using the following analytical solution (Ishibashi and Hazarica, 2015):

$$K = \frac{Q}{\pi(h_2^2 - h_1^2)} \ln\left(\frac{r_2}{r_1}\right), \tag{5.13}$$

where Q is the pumping rate at the borehole, h_1 and h_2 are the radii of W3 and Ex2, respectively, and h_1 and h_2 are the groundwater levels under steady-state conditions in W3 and Ex2, respectively. The results of the pumping test are provided in Table 5.3. Using these results, we found that the value of K was 3.01×10^{-3} m/s. Using the values in Tables 5.2 and K value (i.e., 3.01×10^{-3} m/s), we determined the Darcy velocity, namely, $v = 0.265 \times 10^{-5}$ m/s, as presented in Table 5.4. This value is reasonably close to that estimated by Nakaya et al. (2018) ($K = 1.68 \times 10^{-7}$–1.15×10^{-5}) for an underground dammed limestone aquifer.

5.4.2 Darcy Velocity Estimates Obtained from SBDTs

Figures 5.8 and 5.9 present the BTCs and fitting results for Ex1 and Ex2, respectively. As can be seen from these figures, for all cases, our fitting procedure provided results that were well fitted to the BTCs. In addition, the magnitude of the slope of the BTCs increased with the elevation above sea level for both boreholes. This suggests that lower layers of the aquifer had relatively low values of K.

Table 5.4: Calculation results of Darcy velocity.

Hydraulic gradient	
$\partial z/\partial x$	-6.00×10^{-4}
$\partial z/\partial y$	-6.45×10^{-4}
Hydraulic conductivity	3.01×10^{-3} m/s
Direction of flow	S42.9°E
Darcy velocity	0.265×10^{-5} m/s

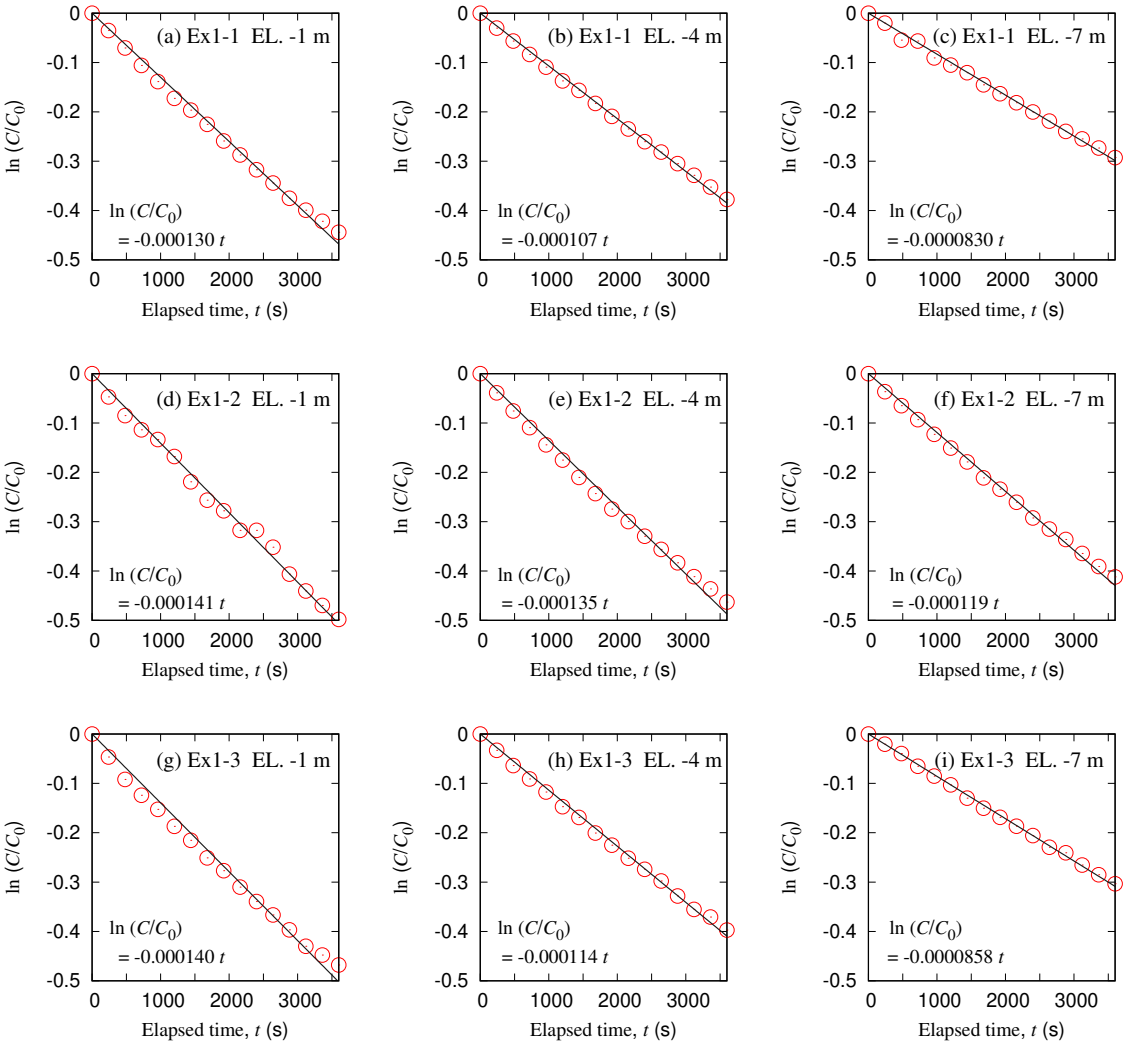

Figure 5.8: Breakthrough curves and fitting results for Ex1. (a)–(c) Ex1-1, (d)–(f) Ex1-2, (g)–(i) Ex1-3.

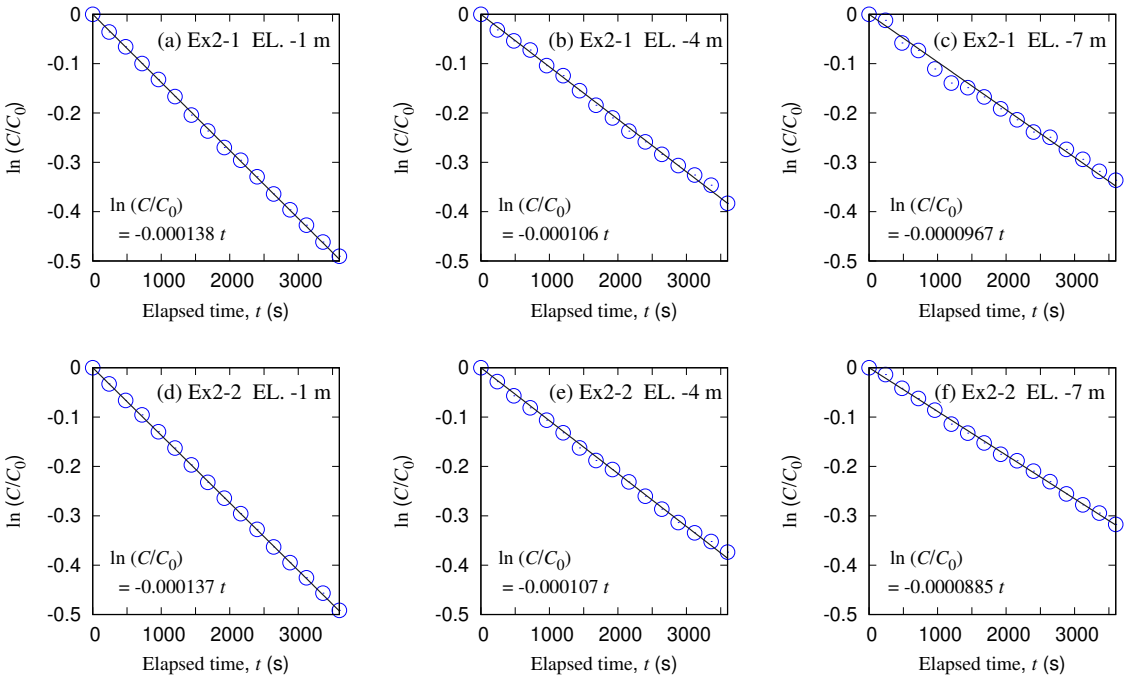

Figure 5.9: Breakthrough curves and fitting results for Ex2. (a)–(c) Ex2-1, (d)–(f) Ex2-2.

The results of the Darcy velocity calculated from the data in Figures 5.8 and 5.9 are presented in Table 5.5. This table indicates that for the same borehole and elevation, the Darcy velocity did not vary significantly with changes in season; thus, the reproducibility of the experimental results of the SBDTs was excellent. In addition, the average Darcy velocity of Ex1 was approximately 4 times larger than that of Ex2. This may be attributed to the different opening ratio and the presence of gravel pack within the borehole annulus; however, the cause is not clear in our study. Thus, further investigation is needed to evaluate the dependency of the Darcy velocity estimate on the borehole design.

For both boreholes (i.e., Ex1 and Ex2), the lower layers had lower Darcy velocities. As mentioned above, this suggests that the lower layers had relatively low values of K. However, the Darcy velocity did not vary dramatically with elevation since there was no change in the geological material over the experimental interval (see Figure 5.3). Moreover, for both Ex1 and Ex2, the $|v|$ values obtained from the SBDTs were in reasonable agreement with the results based on Darcy's law, which demonstrates the validity of estimating the Darcy velocity from SBDTs.

Table 5.5: Results of the Darcy velocity obtained from single-borehole dilution tests.

Borehole	No.	Darcy velocity $\|v\|$ m/s $\times 10^{-5}$				
		EL. −1 m	EL. −4 m	EL. −7 m	Test avg.	Borehole avg.
Ex1	1	2.04	1.68	1.30	1.67	1.84
	2	2.21	2.13	1.87	2.07	
	3	2.19	1.79	1.35	1.78	
Ex2	1	0.542	0.418	0.380	0.447	0.442
	2	0.538	0.421	0.348	0.436	

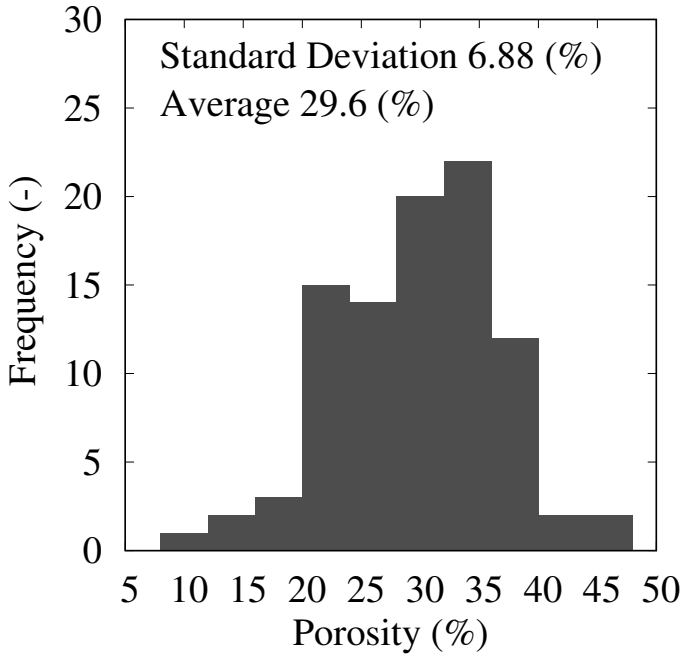

Figure 5.10: Histogram of porosity of Ryukyu limestone cores.

5.4.3 Porosity Results

Figure 5.10 presents a histogram of the porosity estimates. The average, minimum, and maximum porosity was 29.6%, 10.6%, and 46.7%, respectively. In addition, the standard deviation of the porosity was 6.88%. Miyagi and Komiya (2003) reported that the porosity of Ryukyu limestone samples from Miyako Island, Japan, was in the range of 5 to 40%, which is a similar range to that in our experiments. However, the average porosity obtained in this study is slightly larger than that obtained by Miyagi and Komiya (2003). According to Noma (1977), Ryukyu limestone is

Table 5.6: Conditions of the additional experiment.

Borehole	Ex2
Radius of borehole	2.5 cm
NaCl mass	1.4 g
Dissolution time	180 s

Table 5.7: Darcy velocities obtained from the additional experiment.

EL. (cm)	$\|v\|$(m/s) $\times 10^{-5}$
-1	0.481
-4	0.145
-7	0.127

topographically and hydrogeologically divided into three classes: Higher, Middle, and Lower Ryukyu limestone. Lower Ryukyu limestone, which is less consolidated than other classes of limestone, was widely distributed in our field site, resulting in a larger porosity value in our study.

5.4.4 Estimation of Macrodispersivities

To estimate the longitudinal and transverse macrodispersivities, we conducted an additional experiment with lower NaCl concentrations to avoid the effects of molecular diffusion and density current. Table 5.6 presents the conditions of this experiment. BTCs were observed at -1.0 m, -4.0 m, and -7.0 m above sea level. The procedure for estimating the macrodispersivities involved the following steps:

1. Using equation (5.3), the $|v|$ values were estimated by linear least-squares minimization without excluding the initial data, as illustrated in Figure 5.5, since a lower NaCl concentration was used. The estimated Darcy velocities are presented in Table 5.7.

2. For SBDTs in a borehole with a square cross section, Fujinawa (1983) provided the following analytical solution of breakthrough curve:

$$\frac{C}{C_0} = \frac{1}{2}\left(\mathrm{erf}\left(\frac{a-(|v|/n)t}{2\sqrt{D_L t}}\right)+\mathrm{erf}\left(\frac{a+(|v|/n)t}{2\sqrt{D_L t}}\right)\right)\mathrm{erf}\left(\frac{a}{2\sqrt{D_T t}}\right), \qquad (5.14)$$

Table 5.8: Estimated values of longitudinal (A_L) and transverse (A_T) macrodispersivities at -1.0 m, -4.0 m, and -7.0 m above sea level.

EL. (m)	A_L (m)	A_T (m)	A_L/A_T $(-)$
-1	4.84×10^{-2}	8.71×10^{-4}	55.6
-4	2.71×10^{-2}	2.41×10^{-4}	112.0
-7	2.67×10^{-2}	2.16×10^{-4}	123.0

where n is the porosity, $D_L = A_L|v|$ is the longitudinal dispersion coefficient, A_L is the longitudinal macrodispersivity, $D_T = A_T|v|$ is the transverse dispersion coefficient, A_T is the transverse macrodispersivity, and a is half the side of the square borehole cross section. The radius R of borehole Ex2 was converted to a using the following relationship between R and a:

$$a = \frac{1}{2} R\sqrt{\pi}. \tag{5.15}$$

The longitudinal and transverse macrodispersivities (A_L, A_T) were determined by fitting equation (5.14) to the BTCs, where n and R were set to 29.6% (see Figure 5.10) and 2.5 cm (see Table 5.1), respectively.

The estimated parameters (A_L, A_T) are listed in Table 5.8. Figure 5.11 also presents the measured and fitted BTCs at -1.0 m, -4.0 m, and -7.0 m above sea level. The A_L values are one or two orders of magnitude larger than the A_T values, which is in agreement with the results provided in Chapter 2, 3, and 4. Gelhar et al. (1992) collected the values of longitudinal and transverse macrodispersivities in the field from various studies. Figures 5.12 and 5.13 display the relationship between the longitudinal and transverse macrodispersivity, respectively, and the observation scale. As can be seen from these figures, A_L and A_T exhibit scale dependence, which is also in agreement with the results of Chapters 2, 3, and 4. The scale dependence of dispersivity has been reported in many studies. However, a comparison indicated that the values of A_L and A_T obtained in this study are smaller than those obtained by Gelhar et al. (1992). This can be attributed to the fact that the observation scale of SBDTs is extremely small.

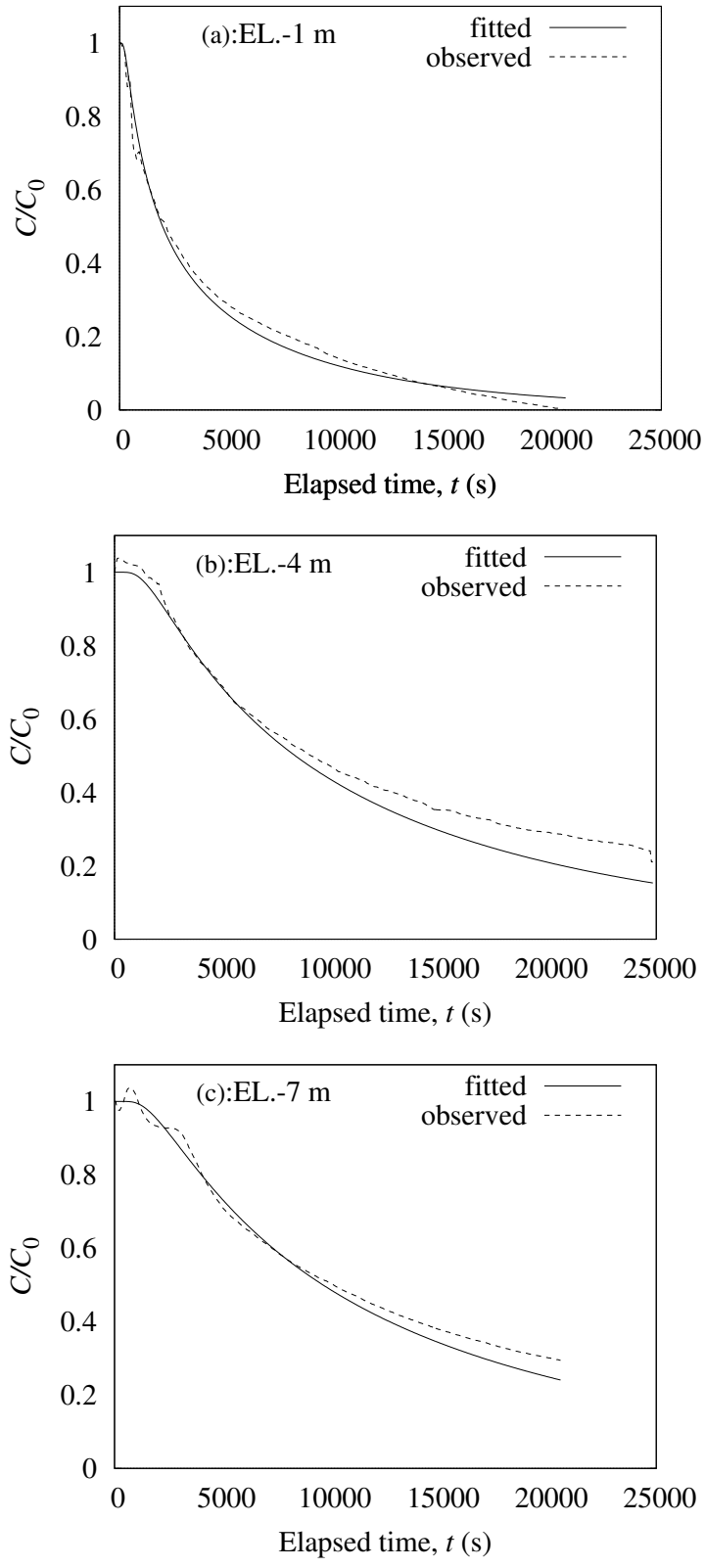

Figure 5.11: Breakthrough curves fitted using equation (5.14). (a) −1.0 m, (b) −4.0 m, (c) −7.0 m.

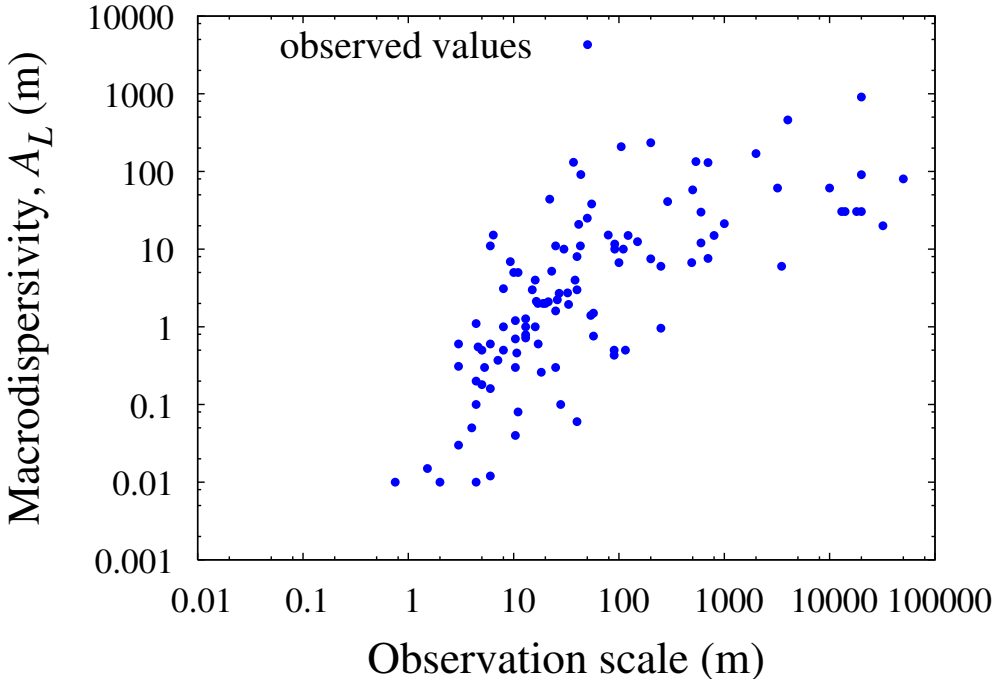

Figure 5.12: Relationship between longitudinal macrodispersivity and observation scale. Source: Gelhar et al., 1992.

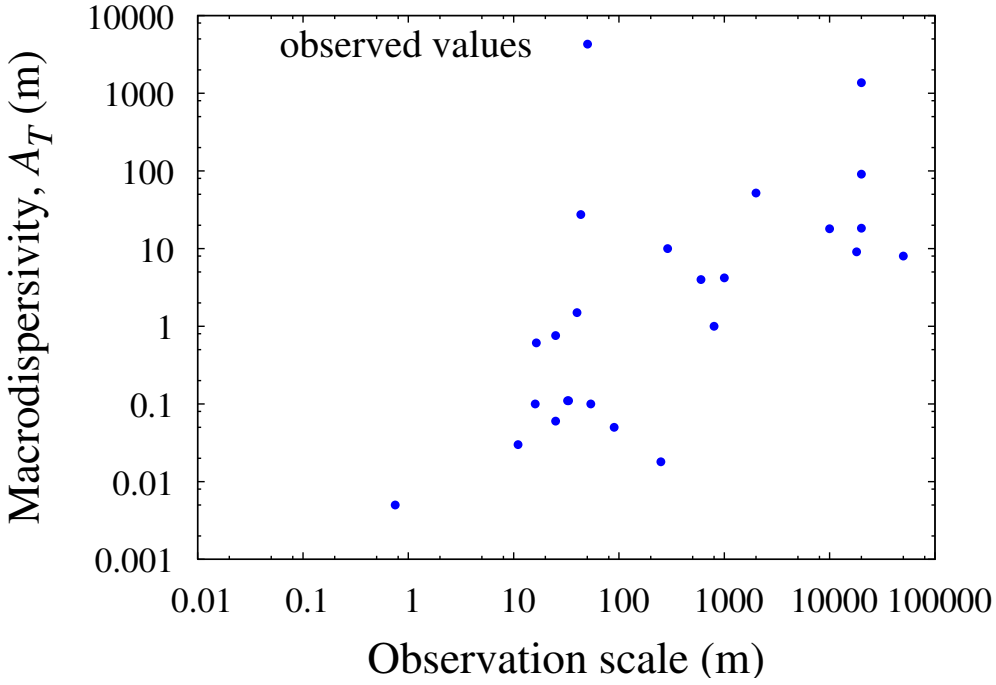

Figure 5.13: Relationship between transverse macrodispersivity and observation scale. Source: Gelhar et al., 1992.

5.5 Conclusions

In this study, we conducted SBDTs using two different boreholes in a Ryukyu limestone aquifer and estimated the transport parameters, including the Darcy velocity and dispersivity, at several elevations. In addition, 93 core samples of Ryukyu limestone at the field were collected, and their porosities were determined using the Archimedes buoyancy method. Estimates of the Darcy velocity obtained from the SBDTs were in reasonably good agreement with the results based on Darcy's law (i.e., based on the ambient hydraulic gradient and the hydraulic conductivity of the aquifer). These results indicate the validity of estimating the Darcy velocity from SBDTs. The average porosity obtained from 93 core samples was 29.6%, which was slightly larger than that of a previous study. This was because Lower Ryukyu limestone, which is less consolidated than other classes of limestone, was distributed in our field site. Moreover, the longitudinal and transverse macrodispersivities were determined using the analytical solution provided by Fujinawa (1983). By comparing the dispersivities obtained in this study with literature values, we found that the macrodispersivities of our experiments were relatively small. This is due to the fact that the observation scale of SBDTs is extremely small.

6 Conclusions

Contents

6.1 Conclusions

The aim of this research project was to improve our fundamental understanding of solute transport in heterogeneous aquifers and to quantify transport parameters. Four objectives were set to meet this aim.

In Chapter 2, we investigated the relationship between solute dispersion and heterogeneous structure with simple heterogeneity patterns, namely, step-function models where the heterogeneity consisted of a succession of two porous materials in serial order. Four laboratory-scale tracer experiments were conducted. We also employed an image analysis technique that was non-invasive and made it possible to map the concentration distribution of dye tracers without disturbing the plume dynamics. In agreement with a previous study, the longitudinal macrodispersivity increased with travel distance in stratified porous media. In contrast, the transverse macrodispersivity decreased with travel distance. This is because transverse macrodispersivity strongly depends on the initial source size in the transverse direction (i.e., perpendicular to

the flow direction). We also defined the travel distances x_{05} and x_{95} corresponding to the 5th and 95th percentiles of the cumulative concentrations in the longitudinal direction, which reflect the travel distances of the fastest and slowest portions of the tracer plume, respectively. It was found that in the step-function models, forward and backward tails spread out linearly in the longitudinal direction.

In Chapter 3, a laboratory experiment and numerical simulations were conducted to assess the impact of upscaling the hydraulic conductivity on solute dispersion in a stratified heterogeneous formation. To obtain three upscaled models, we used a geometric averaging technique, which is frequently used to upscale hydraulic conductivities. To model solute movement through porous media, we employed the random walk particle tracking (RWPT) method, which simulates solute transport by partitioning the solute mass into a large number of representative particles. It was found that the smoothing effect of upscaling reduced the degree of heterogeneity. However, the correlation length was not dependent on layer coarsening (i.e., upscaling). The longitudinal and transverse macrodispersivities obtained from numerical simulation by RWPT were in good agreement with the experimental values. The use of coarse layers in the upscaled models led to underestimation of the longitudinal macrodispersivity; however, it did not affect the transverse macrodispersivity. Moreover, we found that the degree of longitudinal dispersion was affected by the increase in layer thickness as well as changes in the heterogeneity and correlation length due to upscaling.

In practice, natural sandy aquifers often exhibit geological stratification; therefore, it is important to assess the effect of upscaling for stratified formations. However, natural soils and aquifers generally have a more complex structure. In this context, Chapter 4 presented laboratory tracer experiments that evaluated the effect of upscaling on solute dispersion in two-dimensional randomly heterogeneous media. The results demonstrated that for the upscaling process, when the length of the cell was greater than the correlation scale of the reference field, the macrodispersivity was largely underestimated. We also estimated the forward and backward tails of a tracer plume. The results indicated that the distance between the forward and backward tails (i.e., solute spreading) tended to decrease with decreasing resolution by upscaling.

Chapter 5 focused on the field evaluation of transport parameters using two different boreholes in a Ryukyu limestone aquifer. The construction of a subsurface dam is planned for this aquifer; therefore, determining the flow characteristics is important. We employed SBDTs, which are methods for evaluating transport parameters using boreholes. By comparing the Darcy velocities estimated from the SBDTs and Darcy's law (i.e., the ambient hydraulic gradient and hydraulic conductivity of the aquifer), the validity of using SBDTs to estimate transport parameters was verified. Furthermore, the longitudinal and transverse macrodispersivities estimated from the SBDTs were smaller than those reported in the literature. In addition, 93 core samples of Ryukyu limestone in the field were collected, and the porosity, which is important for determining the water storage capacity of a subsurface dam, was determined using the Archimedes buoyancy method. The average porosity obtained was 29.6%, which was slightly larger than that obtained in a previous study. This can likely be attributed to the fact that Lower Ryukyu limestone, which is poorly consolidated, was distributed at our field site.

6.2 Future work

Several interesting topics were outside the scope of this thesis; however, their study would be of considerable scientific and engineering importance. One of these topics is to evaluate the relationship between solute dispersion and upscaling in three-dimensional heterogeneous media. In this thesis, the discussion was limited to a two-dimensional system; however, real aquifers are three-dimensional systems. Therefore, further investigation of solute dispersion in three-dimensional systems would be valuable.

Chapters 3 and 4 addressed the effects of upscaling on solute transport characteristics, particularly the degree of spreading. In future work, upscaling methodologies should be developed using the results of this thesis to achieve more accurate modeling of solute transport. Chapter 5 also focused on the estimation of transport parameters using SBDTs. SBDTs are some of the simplest methods to determine transport parameters, although it is difficult to evaluate scale-dependent parameters, such as longitudinal and transverse macrodispersivities, since the observation scale of SBDTs is extremely small. However, field experiments designed to assess this scale dependence are costly, time-consuming, and relatively difficult to execute. For instance, LeBlanc et al.

(1991) measured solute concentrations using 656 multilevel samplers (i.e., monitoring wells), while Sudicky (1986) used 275 installed multilevel sampling devices. Therefore, in future work, simpler methods should be proposed to estimate scale-dependent solute transport parameters.

Appendices

A

Fundamentals of Flow and Solute Transport in Porous Media

A.1 Steady-State Flow Equation

Consider a control volume in the shape of a rectangular parallelepiped box of dimensions $\Delta x \times \Delta y \times \Delta z$ inside the flow domain in an aquifer (Figure A.1). Referring to Figure A.1, we can obtain an expression for the total excess of mass inflow over outflow during a short time interval Δt:

$$\begin{aligned}&\left(\rho v_x - \left(\rho v_x + \frac{\partial \rho v_x}{\partial x}\Delta x\right)\right)\Delta y \Delta z \Delta t \\ +&\left(\rho v_y - \left(\rho v_y + \frac{\partial \rho v_y}{\partial y}\Delta y\right)\right)\Delta x \Delta z \Delta t \\ +&\left(\rho v_z - \left(\rho v_z + \frac{\partial \rho v_z}{\partial z}\Delta z\right)\right)\Delta x \Delta y \Delta t,\end{aligned} \tag{A.1}$$

where ρ is the mass density of water, and v_x, v_y, and v_z are components of the Darcy velocity. Formula (A.1) can be rewritten as follows:

$$\left(-\frac{\partial \rho v_x}{\partial x} - \frac{\partial \rho v_y}{\partial y} - \frac{\partial \rho v_z}{\partial z}\right)\Delta x \Delta y \Delta z \Delta t. \tag{A.2}$$

For steady-state conditions, formula (A.1) is equal to zero, and the equation of continuity becomes

$$-\frac{\partial \rho v_x}{\partial x} - \frac{\partial \rho v_y}{\partial y} - \frac{\partial \rho v_z}{\partial z} = 0. \tag{A.3}$$

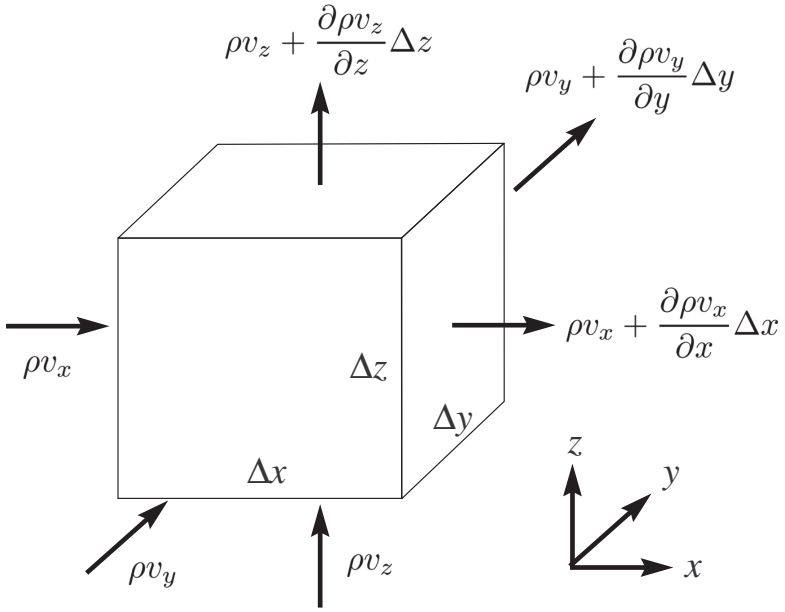

Figure A.1: Elemental control volume.

For an incompressible fluid, ρ is constant and can be divided out of equation (A.3) as follows:

$$-\frac{\partial v_x}{\partial x} - \frac{\partial v_y}{\partial y} - \frac{\partial v_z}{\partial z} = 0. \tag{A.4}$$

If a porous medium is characterized by three principal axes of hydraulic conductivity, and these principal axes are aligned with the coordinate axes, then using Darcy's law, the components of the Darcy velocity (v_x, v_y and v_z) can be expressed as

$$\begin{aligned} v_x &= -K_x \frac{\partial h}{\partial x}, \\ v_y &= -K_y \frac{\partial h}{\partial y}, \\ v_z &= -K_z \frac{\partial h}{\partial z}, \end{aligned} \tag{A.5}$$

where h is the head, and K_x, K_y, and K_z are the components of hydraulic conductivity in the respective coordinate directions. By substituting equation (A.5) into equation (A.4), we obtain an expression of the equation of continuity:

$$\frac{\partial}{\partial x}\left(K_x \frac{\partial h}{\partial x}\right) + \frac{\partial}{\partial y}\left(K_y \frac{\partial h}{\partial y}\right) + \frac{\partial}{\partial z}\left(K_z \frac{\partial h}{\partial z}\right) = 0. \tag{A.6}$$

For an isotropic medium (i.e., $K_x = K_y = K_z = K$), equation (A.6) can be simply expressed as

$$\nabla \cdot (K \nabla h) = 0. \tag{A.7}$$

For a homogeneous isotropic medium, equation (A.6) can also be expressed as

$$\frac{\partial^2 h}{\partial x^2} + \frac{\partial^2 h}{\partial y^2} + \frac{\partial^2 h}{\partial z^2} = \nabla^2 h = 0. \tag{A.8}$$

Equation (A.8) is called the Laplace equation and is one of the most commonly used partial differential equations.

A.2 Advection–Dispersion Equation

Conservative solute transport in porous media is dominated by advection, which causes the movement of a solute in a flowing fluid according to the average seepage velocity, and by hydrodynamic dispersion, which is caused by the combined action of molecular diffusion (resulting from concentration gradients) and mechanical dispersion (resulting from velocity variations at the pore scale). Figure A.2 presents a diagram illustrating the factors causing mechanical dispersion. For a pulse source, the solute concentration distribution in time and space is displayed in Figure A.3. The concentration distribution is initially sharp and is smoothed out as the concentration is diluted by hydrodynamic dispersion. The center of mass is advected at an average linear velocity.

Consider a control volume in the shape of a rectangular parallelepiped box, as illustrated in Figure A.1. The mass of solute transported in the x-direction by advection and hydrodynamic dispersion can be represented as

$$\begin{aligned} \text{Mass transported by advection} &= v'_x n C \; dA, \\ \text{Mass transported by hydrodynamic dispersion} &= n D_x \frac{\partial C}{\partial x} \; dA, \end{aligned} \tag{A.9}$$

where n is the porosity, dA is the elemental cross-sectional area, $D_x = \alpha_x v'_x + D_d$ is the hydrodynamic dispersion coefficient in the x-direction, α_x is the dispersivity in the x-direction, v'_x is the pore velocity in the x-direction, and D_d is the effective molecular diffusion coefficient in porous media. Thus, the expression for flux in the x-direction can be written as

$$F_x = v'_x n C + n D_x \frac{\partial C}{\partial x}, \tag{A.10}$$

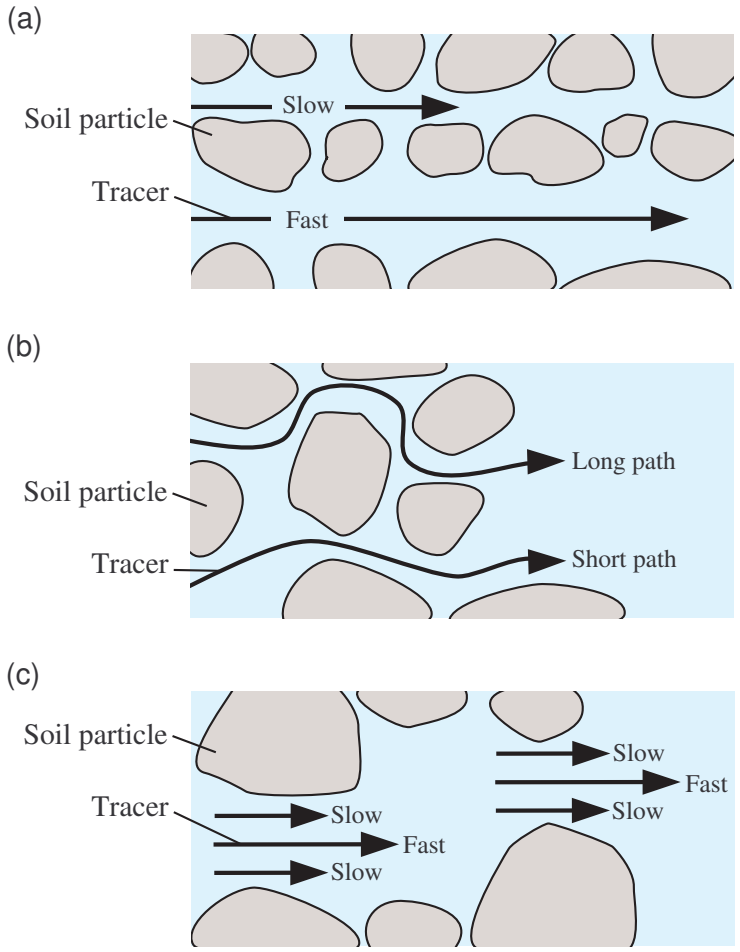

Figure A.2: Factors causing mechanical dispersion.

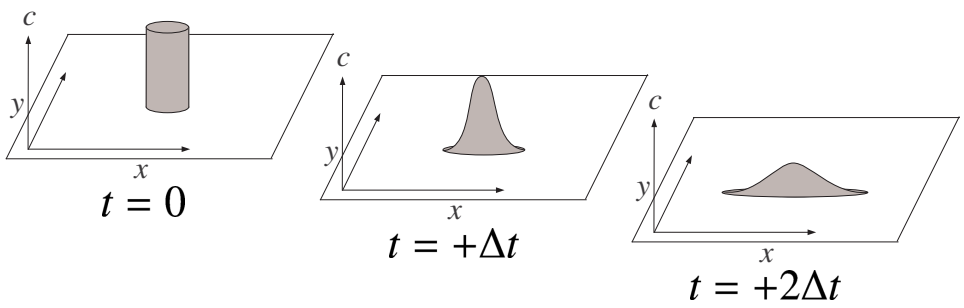

Figure A.3: Spatial distribution of conservative solute concentration from a pulse source.

where F_x is the total mass of solute per unit cross-sectional area transported in the x-direction per unit time. Similarly, F_y and F_z can be expressed as

$$\begin{aligned} F_y &= v'_y nC + nD_y \frac{\partial C}{\partial y}, \\ F_z &= v'_z nC + nD_z \frac{\partial C}{\partial z}. \end{aligned} \tag{A.11}$$

The difference in the amount entering and leaving the control volume can be written as

$$\begin{aligned} &- (F_x\ dz\ dy + F_y\ dz\ dx + F_z\ dx\ dy) \\ &+ \left(F_x + \frac{\partial F_x}{\partial x}\ dx\right) dz\ dy + \left(F_y + \frac{\partial F_y}{\partial y}\ dy\right) dz\ dx + \left(F_z + \frac{\partial F_z}{\partial z}\ dz\right) dx\ dy \\ &= \left(\frac{\partial F_x}{\partial x} + \frac{\partial F_y}{\partial y} + \frac{\partial F_z}{\partial z}\right) dx\ dy\ dz. \end{aligned} \tag{A.12}$$

In addition, the rate of change of solute mass in the control volume is written as

$$-n\frac{\partial C}{\partial t}\ dx\ dy\ dz. \tag{A.13}$$

Using formulas (A.12) and (A.13), we obtain the complete conservation of mass expression as follows:

$$\frac{\partial F_x}{\partial x} + \frac{\partial F_y}{\partial y} + \frac{\partial F_z}{\partial z} = -n\frac{\partial C}{\partial t}. \tag{A.14}$$

Substituting equations (A.10) and (A.11) into equation (A.14) yields

$$\begin{aligned} &\left(\frac{\partial}{\partial x}\left(D_x\frac{\partial C}{\partial x}\right) + \frac{\partial}{\partial y}\left(D_y\frac{\partial C}{\partial y}\right) + \frac{\partial}{\partial z}\left(D_z\frac{\partial C}{\partial z}\right)\right) \\ &\quad - \left(\frac{\partial}{\partial x}(v'_x C) + \frac{\partial}{\partial y}(v'_y C) + \frac{\partial}{\partial z}(v'_z C)\right) = \frac{\partial C}{\partial t}. \end{aligned} \tag{A.15}$$

For a homogeneous medium that is steady and uniform, and for hydrodynamic dispersion coefficients D_x, D_y, and D_z that do not vary spatially, equation (A.15) can be rewritten as

$$\begin{aligned} &\left(D_x\frac{\partial^2 C}{\partial x^2} + D_y\frac{\partial^2 C}{\partial y^2} + D_z\frac{\partial^2 C}{\partial z^2}\right) \\ &\quad - \left(v'_x\frac{\partial C}{\partial x} + v'_y\frac{\partial C}{\partial y} + v'_z\frac{\partial C}{\partial z}\right) = \frac{\partial C}{\partial t}. \end{aligned} \tag{A.16}$$

For one-dimensional problems, such as laboratory soil columns, we obtain the following equation:

$$D_x\frac{\partial^2 C}{\partial x^2} - v'_x\frac{\partial C}{\partial x} = \frac{\partial C}{\partial t}. \tag{A.17}$$

B

Images from Experiments

B.1 Temporal Evolution of Tracer Plume in Experiments in Chapter 2

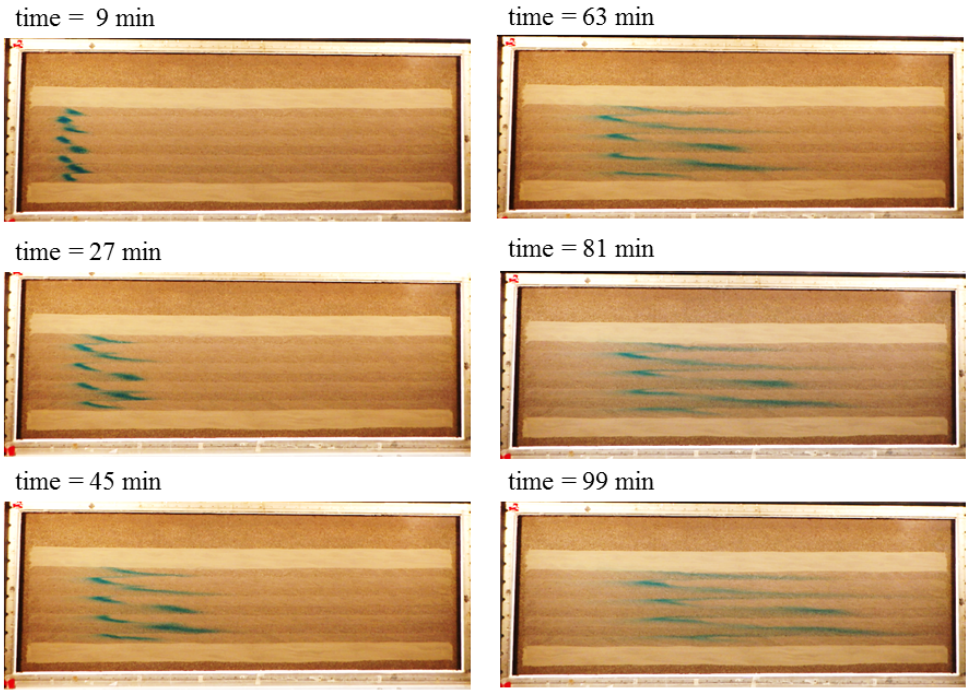

Figure B.1: Temporal evolution of the tracer plume for case A-4 in Chapter 2.

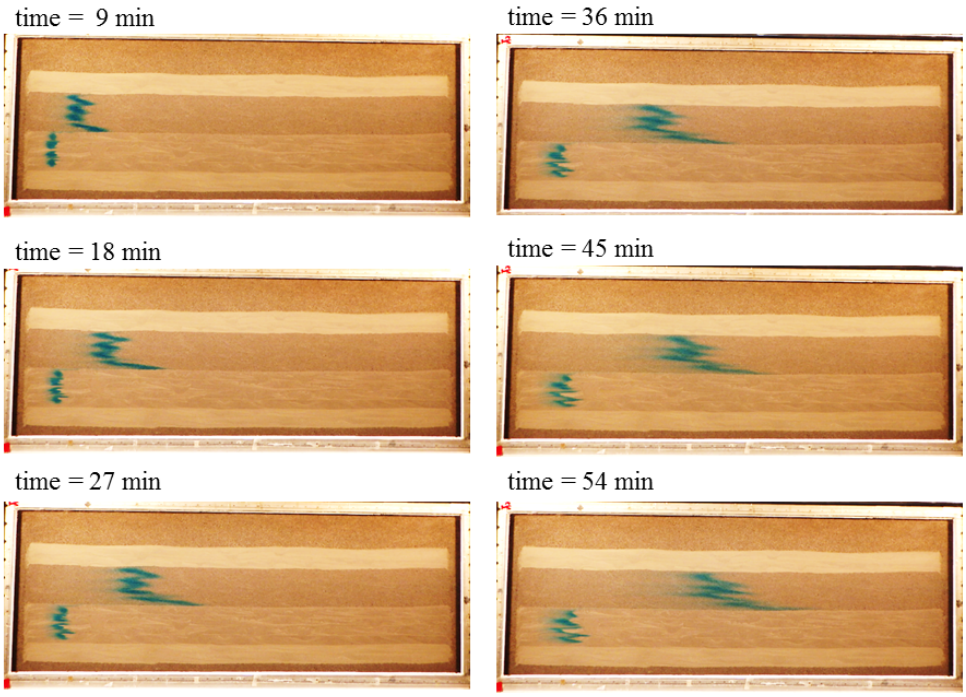

Figure B.2: Temporal evolution of the tracer plume for case A-16 in Chapter 2.

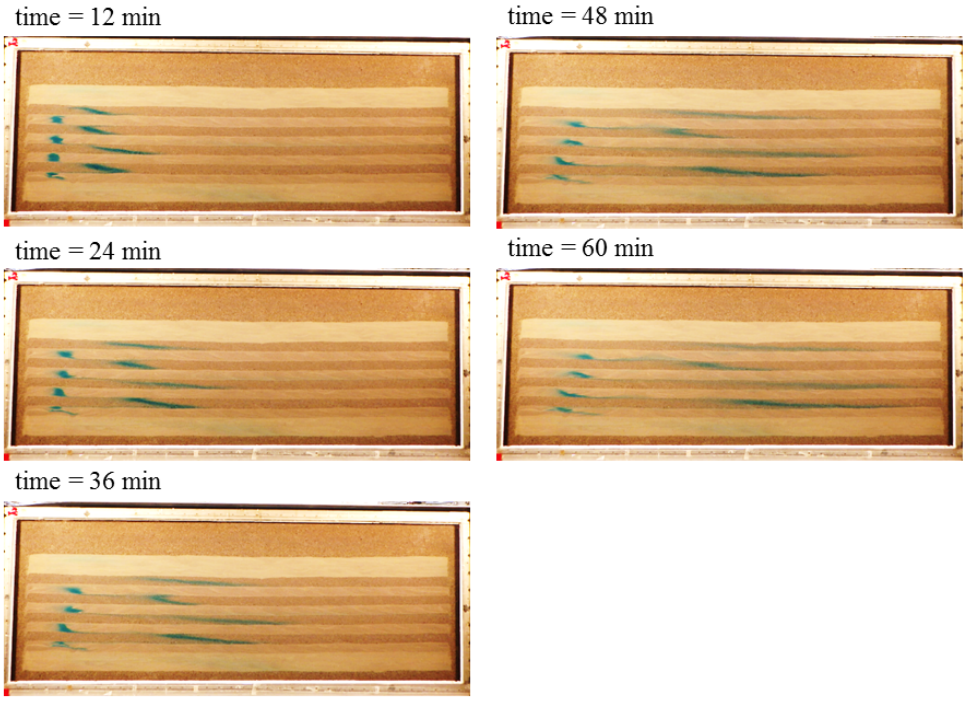

Figure B.3: Temporal evolution of the tracer plume for case B-4 in Chapter 2.

B.2 Temporal Evolution of Tracer Plume in Experiment in Chapter 3

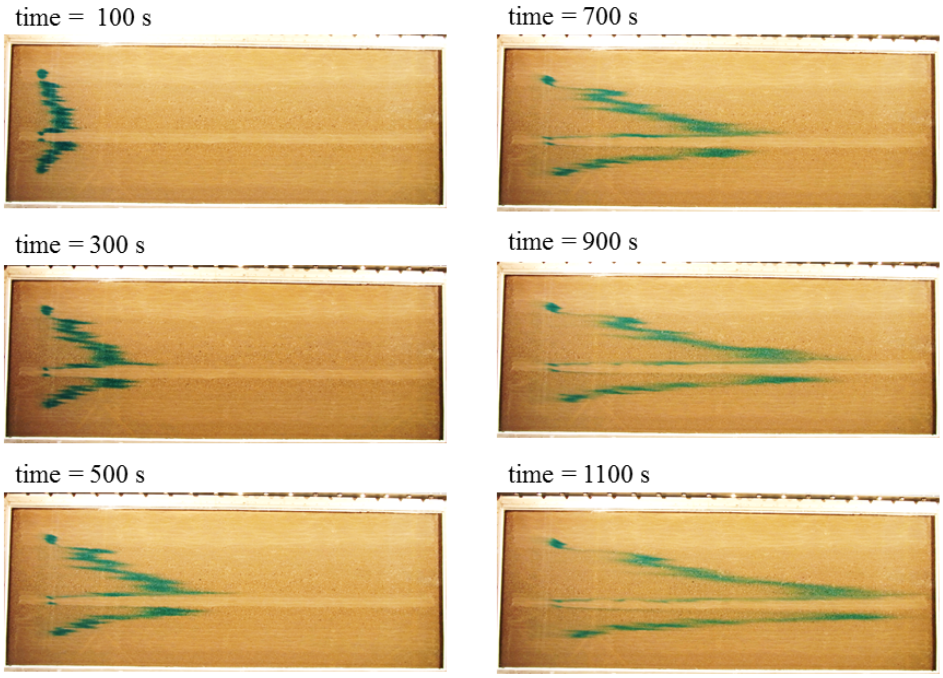

Figure B.4: Temporal evolution of the tracer plume for the stratified formation in Chapter 3.

B.3 Temporal Evolution of Tracer Plume in Experiments in Chapter 4

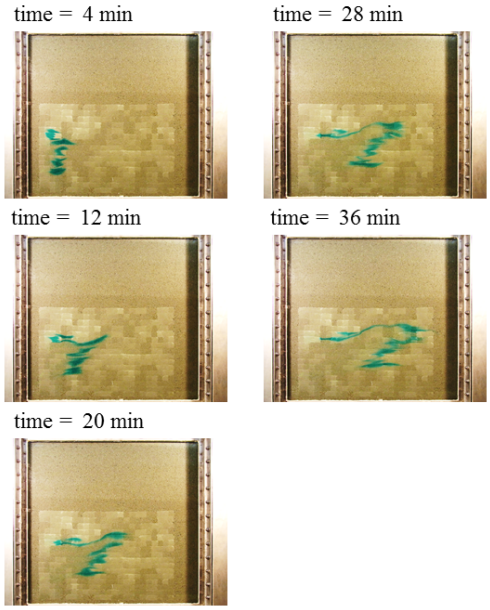

Figure B.5: Temporal evolution of the tracer plume for the Reference field from a line source in Chapter 4.

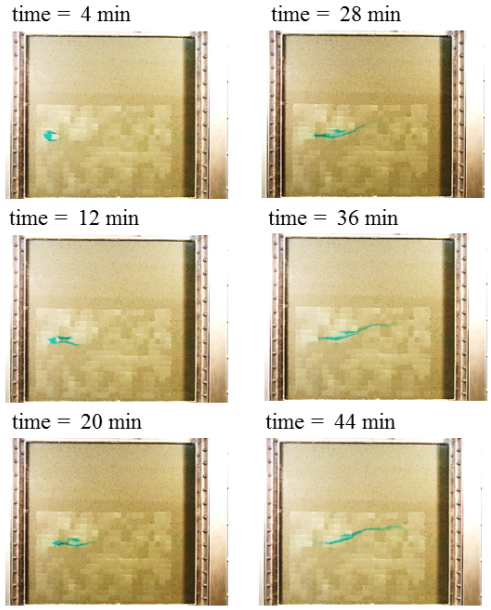

Figure B.6: Temporal evolution of the tracer plume for the Reference field from injection port a in Chapter 4.

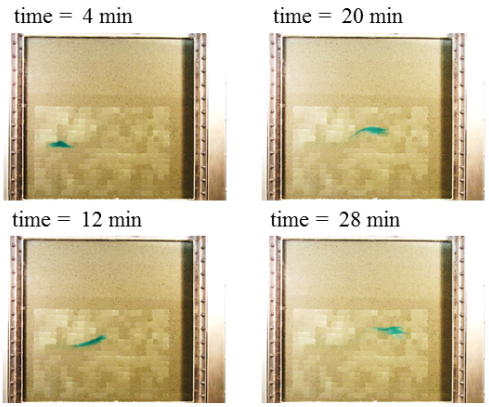

Figure B.7: Temporal evolution of the tracer plume for the Reference field from injection port b in Chapter 4.

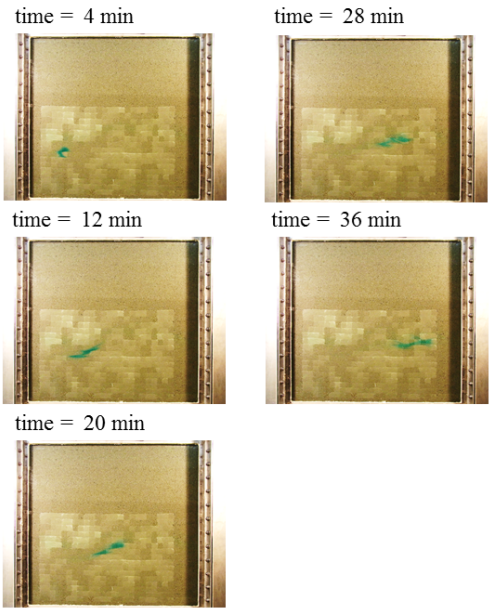

Figure B.8: Temporal evolution of the tracer plume for the Reference field from injection port c in Chapter 4.

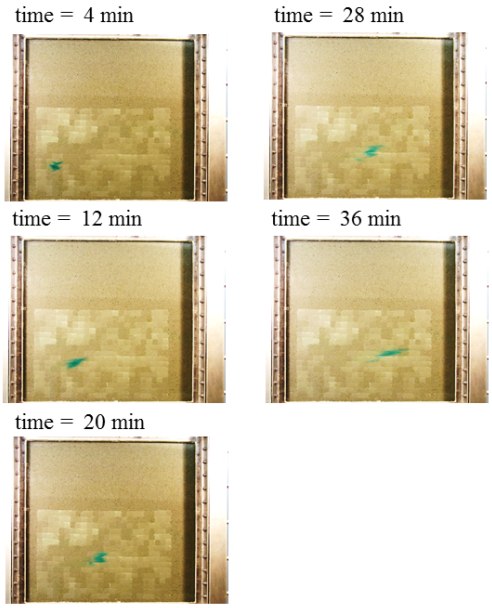

Figure B.9: Temporal evolution of the tracer plume for the Reference field from injection port d in Chapter 4.

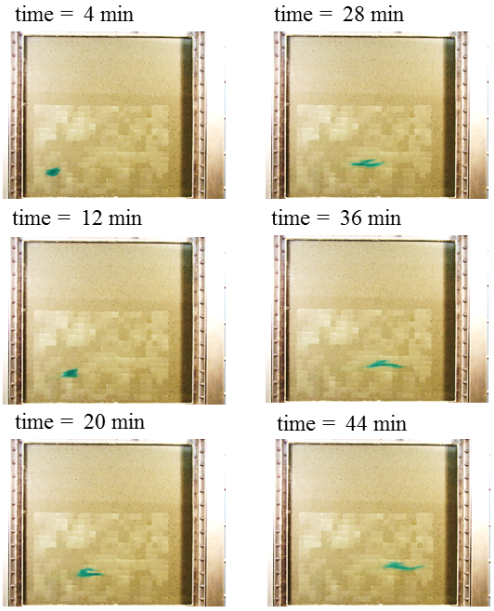

Figure B.10: Temporal evolution of the tracer plume for the Reference field from injection port e in Chapter 4.

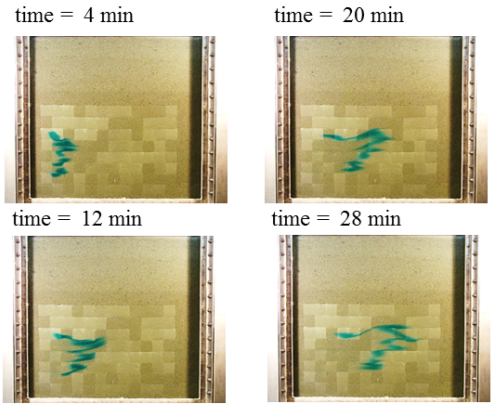

Figure B.11: Temporal evolution of the tracer plume for Upscale A from a line source in Chapter 4.

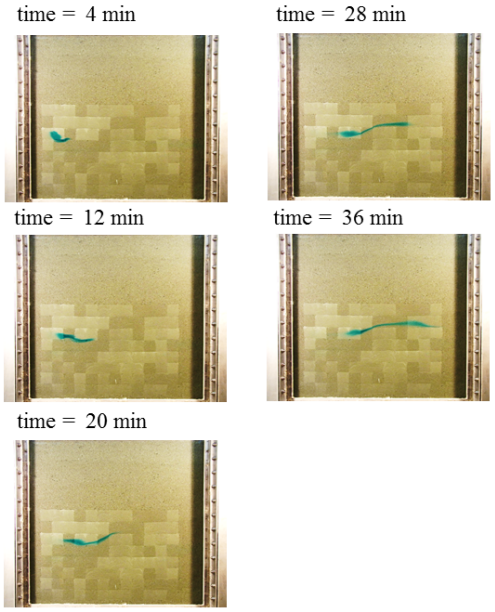

Figure B.12: Temporal evolution of the tracer plume for Upscale A from injection port a in Chapter 4.

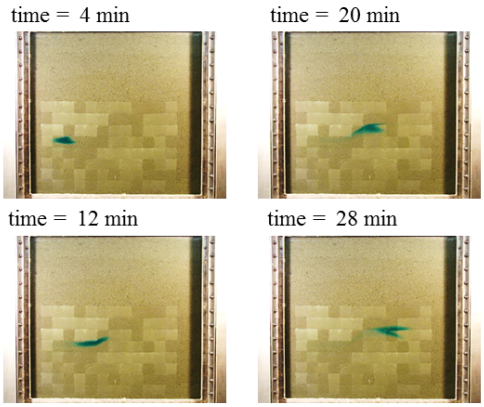

Figure B.13: Temporal evolution of the tracer plume for Upscale A from injection port b in Chapter 4.

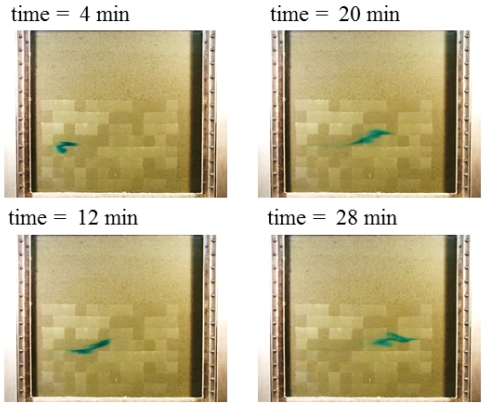

Figure B.14: Temporal evolution of the tracer plume for Upscale A from injection port c in Chapter 4.

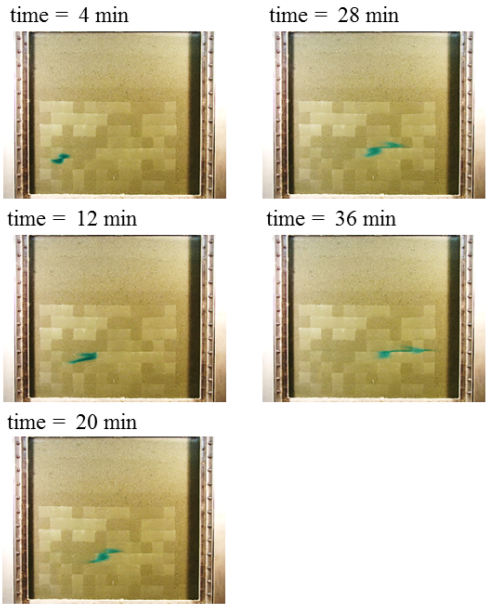

Figure B.15: Temporal evolution of the tracer plume for Upscale A from injection port d in Chapter 4.

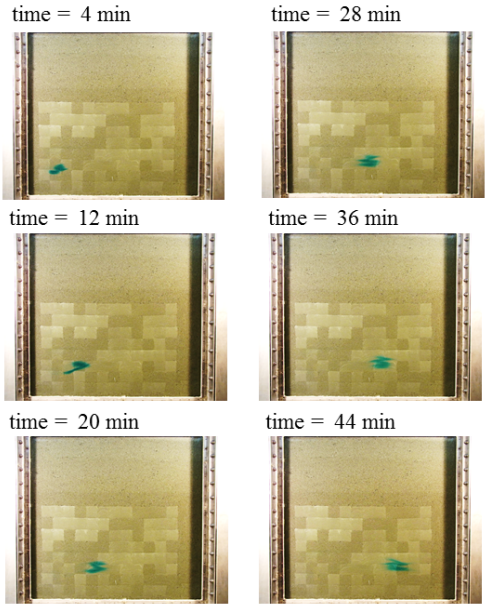

Figure B.16: Temporal evolution of the tracer plume for Upscale A from injection port e in Chapter 4.

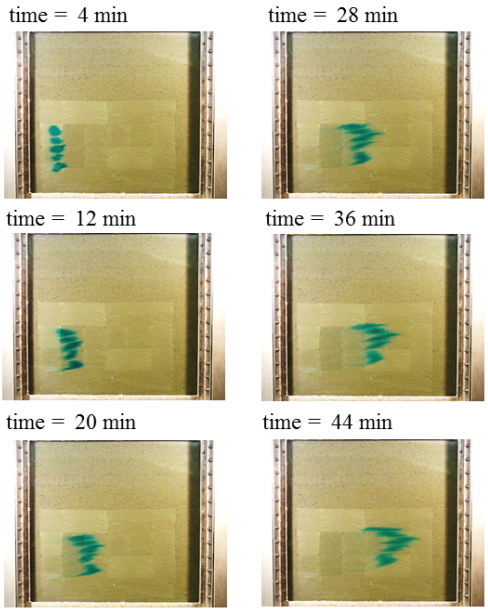

Figure B.17: Temporal evolution of the tracer plume for Upscale B from a line source in Chapter 4.

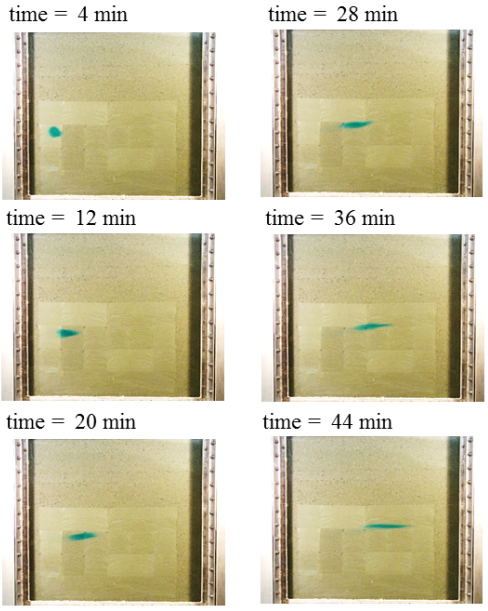

Figure B.18: Temporal evolution of the tracer plume for Upscale B from injection port a in Chapter 4.

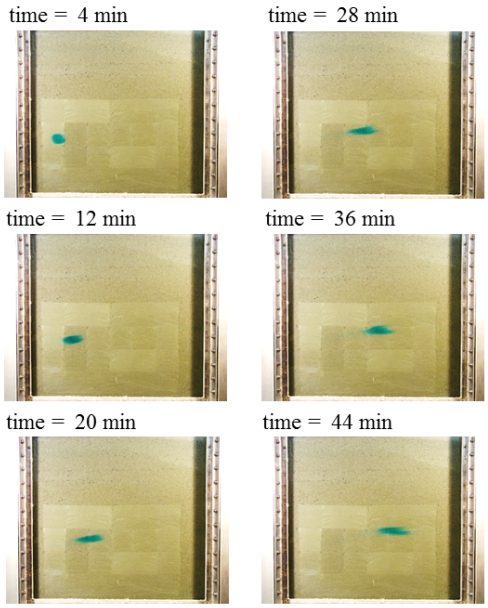

Figure B.19: Temporal evolution of the tracer plume for Upscale B from injection port b in Chapter 4.

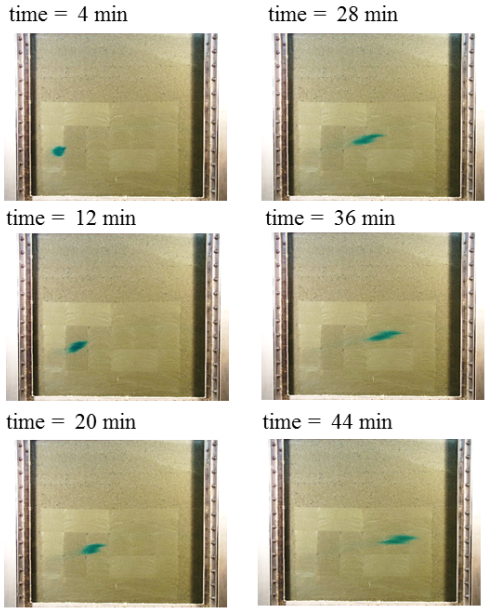

Figure B.20: Temporal evolution of the tracer plume for Upscale B from injection port c in Chapter 4.

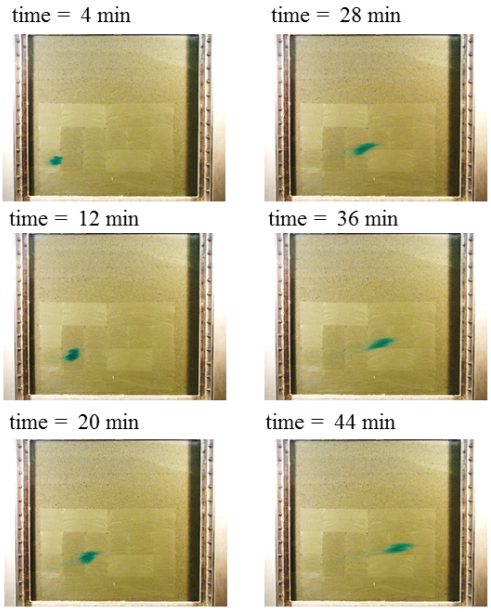

Figure B.21: Temporal evolution of the tracer plume for Upscale B from injection port d in Chapter 4.

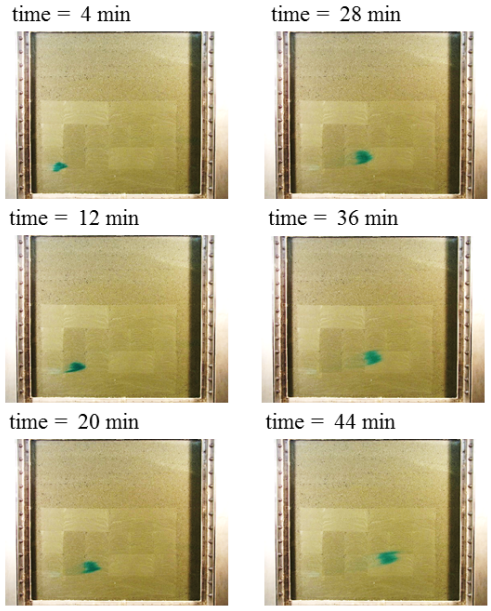

Figure B.22: Temporal evolution of the tracer plume for Upscale B from injection port e in Chapter 4.

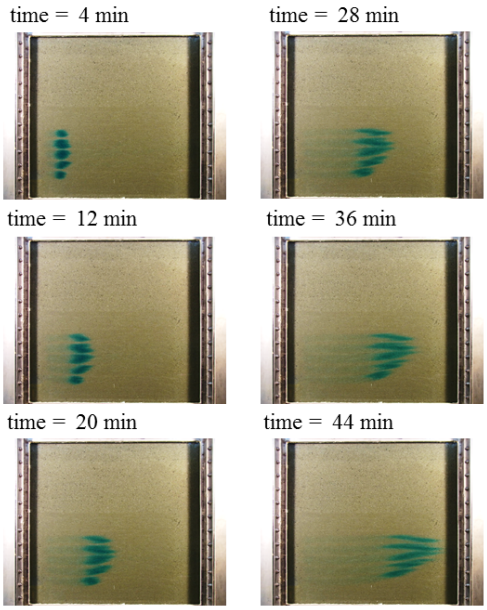

Figure B.23: Temporal evolution of the tracer plume for the Homogeneous case from a line source in Chapter 4.

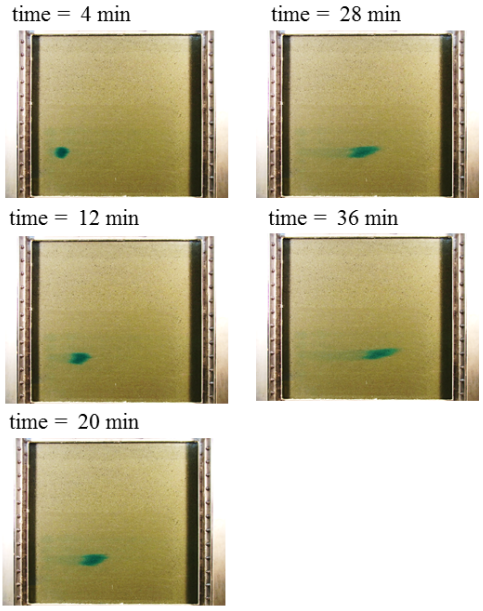

Figure B.24: Temporal evolution of the tracer plume for the Homogeneous case from injection port c in Chapter 4.

B.4 Images for Single-Borehole Dilution Tests in Chapter 5

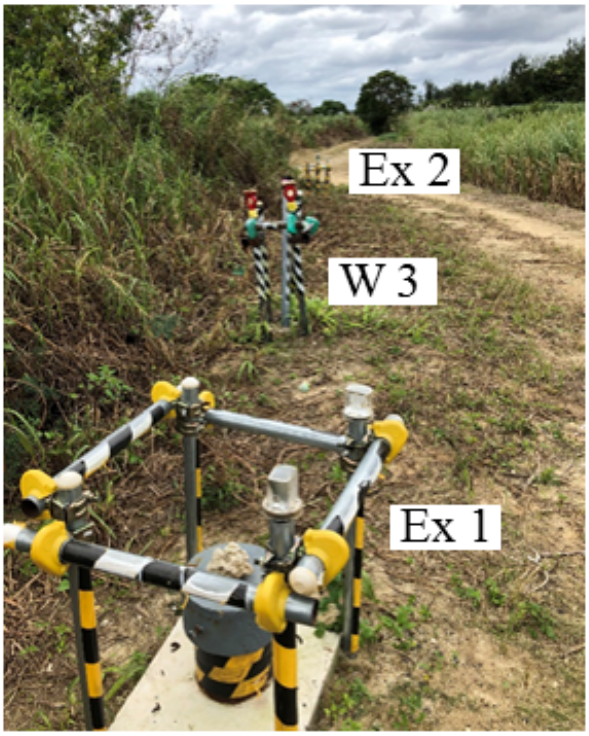

Figure B.25: View of study area in Chapter 5, including three boreholes, Ex1, Ex2, and W3.

Figure B.26: Boreholes used for single-borehole dilution tests. (a) Ex1, (b) Ex2.

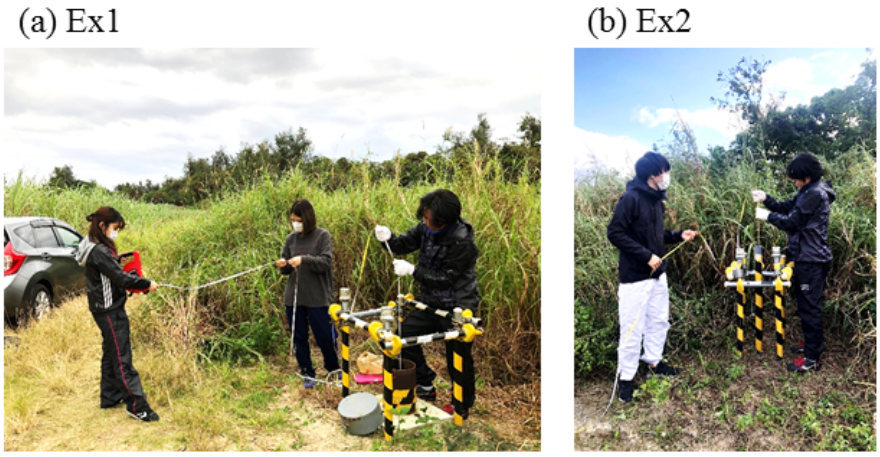

Figure B.27: Photographs of single-borehole dilution tests for boreholes (a) Ex1 and (b) Ex2.

References

Abdoulhalik, A., & Ahmed, A. A. (2017). How does layered heterogeneity affect the ability of subsurface dams to clean up coastal aquifers contaminated with seawater intrusion? *Journal of Hydrology*, *553*, 708–721.

Adams, E. E., & Gelhar, L. W. (1992). Field study of dispersion in a heterogeneous aquifer: 2. spatial moments analysis. *Water Resources Research*, *28*(12), 3293–3307.

Agency, E. P. (1977). *The report to congress: Waste disposal practices and their effects on ground water*. USEPA Office of Water Supply, Office of Solid Waste Management Programs.

Andrade, R., Bhowmick, S., & Pund, A. (2017). Tracer an effective tool in detecting canal seepage: Case studies from northern india. *Sustainable Water Resources Management*, *3*(1), 25–31.

Bear, J. (1972). *Dynamics of fluids in porous media*. American Elsevier Publishing Company.

Bear, J., & Verruijt, A. (1987). *Modeling groundwater flow and pollution*. D. Reidel Publishing Company.

Beaudoin, A., & Dreuzy, J.-R. d. (2013). Numerical assessment of 3-d macrodispersion in heterogeneous porous media. *Water Resources Research*, *49*(5), 2489–2496.

Benson, D. A., Wheatcraft, S. W., & Meerschaert, M. M. (2000). Application of a fractional advection-dispersion equation. *Water Resources Research*, *36*(6), 1403–1412.

Berkowitz, B., Cortis, A., Dentz, M., & Scher, H. (2006). Modeling non-fickian transport in geological formations as a continuous time random walk. *Reviews of Geophysics*, *44*(2).

Bernstein, A., Adar, E., Yakirevich, A., & Nativ, R. (2007). Dilution tests in a low-permeability fractured aquifer: Matrix diffusion effect. *Groundwater*, *45*(2), 235–241.

Boggs, J. M., Young, S. C., Beard, L. M., Gelhar, L. W., Rehfeldt, K. R., & Adams, E. E. (1992). Field study of dispersion in a heterogeneous aquifer: 1. overview and site description. *Water Resources Research*, *28*(12), 3281–3291.

Böhlke, J.-K. (2002). Groundwater recharge and agricultural contamination. *Hydrogeology Journal*, *10*(1), 153–179.

Bolster, D., Valdés-Parada, F. J., LeBorgne, T., Dentz, M., & Carrera, J. (2011). Mixing in confined stratified aquifers. *Journal of Contaminant Hydrology*, *120-121*, 198–212.

Chao, H.-C., Rajaram, H., & Illangasekare, T. (2000). Intermediate-scale experiments and numerical simulations of transport under radial flow in a two-dimensional heterogeneous porous medium. *Water Resources Research*, *36*(10), 2869–2884.

Citarella, D., Cupola, F., Tanda, M. G., & Zanini, A. (2015). Evaluation of dispersivity coefficients by means of a laboratory image analysis. *Journal of Contaminant Hydrology*, *172*, 10–23.

Dagan, G. (1994). Upscaling of dispersion coefficients in transport through heterogeneous porous formations. *Computational Methods in Water Resources X, edited by A. Peters et al.*, 431–439.

Dagan, G. (1984). Solute transport in heterogeneous porous formations. *Journal of Fluid Mechanics*, *145*, 151–177.

Danquigny, C., Ackerer, P., & Carlier, J. P. (2004). Laboratory tracer tests on three-dimensional reconstructed heterogeneous porous media. *Journal of Hydrology*, *294*(1), 196–212.

Dentz, M., Le Borgne, T., Englert, A., & Bijeljic, B. (2011). Mixing, spreading and reaction in heterogeneous media: A brief review. *Journal of Contaminant Hydrology*, *120-121*, 1–17.

Desbarats, A. J. (1992). Spatial averaging of hydraulic conductivity in three-dimensional heterogeneous porous media. *Mathematical Geology*, *24*(3), 249–267.

Dong, H., Chen, J., & Li, X. (2016). Delineation of leakage pathways in an earth and rockfill dam using multi-tracer tests. *Engineering Geology*, *212*, 136–145.

Fahrmeier, N., Goeppert, N., & Goldscheider, N. (2021). Comparative application and optimization of different single-borehole dilution test techniques. *Hydrogeology Journal*, *29*(1), 199–211.

Fernàndez-Garcia, D., & Gómez-Hernández, J. J. (2007). Impact of upscaling on solute transport: Traveltimes, scale dependence of dispersivity, and propagation of uncertainty. *Water Resources Research*, *43*(2).

Fernàndez-Garcia, D., Illangasekare, T. H., & Rajaram, H. (2005). Differences in the scale-dependence of dispersivity estimated from temporal and spatial moments in chemically and physically heterogeneous porous media. *Advances in Water Resources*, *28*(7), 745–759.

Fernàndez-Garcia, D., Rajaram, H., & Illangasekare, T. H. (2005). Assessment of the predictive capabilities of stochastic theories in a three-dimensional laboratory test aquifer: Effective hydraulic conductivity and temporal moments of breakthrough curves. *Water Resources Research*, *41*(4).

Fernàndez-Garcia, D., Sánchez-Vila, X., & Illangasekare, T. H. (2002). Convergent-flow tracer tests in heterogeneous media: Combined experimental–numerical analysis for determination of equivalent transport parameters. *Journal of Contaminant Hydrology*, *57*(1), 129–145.

Fiori, A., Boso, F., Barros, F. P. J. d., Bartolo, S. D., Frampton, A., Severino, G., Suweis, S., & Dagan, G. (2010). An indirect assessment on the impact of connectivity of conductivity classes upon longitudinal asymptotic macrodispersivity. *Water Resources Research*, *46*(8).

Fletcher, T. (2002). Neighborhood change at love canal: Contamination, evacuation and resettlement. *Land Use Policy*, *19*(4), 311–323.

Flury, M., & Flühler, H. (1994). Brilliant blue FCF as a dye tracer for solute transport studies—a toxicological overview. *Journal of Environmental Quality*, *23*(5), 1108–1112.

Freeze, R., & Cherry, J. (1979). *Groundwater*. Prentice-Hall, Englewood Cliffs.

Freyberg, D. L. (1986). A natural gradient experiment on solute transport in a sand aquifer: 2. spatial moments and the advection and dispersion of nonreactive tracers. *Water Resources Research*, *22*(13), 2031–2046.

Fujinawa, K. (1983). Asymptotic solutions to the convection-dispersion equation and powell's optimization method for evaluating groundwater velocity and dispersion coefficients from observed data of single dilution tests. *Journal of Hydrology*, *62*(1), 333–353.

Gelhar, L. W., & Axness, C. L. (1983). Three-dimensional stochastic analysis of macrodispersion in aquifers. *Water Resources Research*, *19*(1), 161–180.

Gelhar, L. W., Gutjahr, A. L., & Naff, R. L. (1979). Stochastic analysis of macrodispersion in a stratified aquifer. *Water Resources Research*, *15*(6), 1387–1397.

Gelhar, L. W., Welty, C., & Rehfeldt, K. R. (1992). A critical review of data on field-scale dispersion in aquifers. *Water Resources Research*, *28*(7), 1955–1974.

Gomo, M. (2020). Effects of artefacts on natural gradient single-borehole tracer dilution tests. *Natural Resources Research*, *29*(3), 2227–2235.

Greiner, A., Schreiber, W., Brix, G., & Kinzelbach, W. (1997). Magnetic resonance imaging of paramagnetic tracers in porous media: Quantification of flow and transport parameters. *Water Resources Research*, *33*(6), 1461–1473.

Gu, B., Ge, Y., Chang, S. X., Luo, W., & Chang, J. (2013). Nitrate in groundwater of china: Sources and driving forces. *Global Environmental Change*, *23*(5), 1112–1121.

Gun, J. v. d. (2012). *Groundawter and global change: Trends, opportunities and challenges.* United Nations Educational, Scientific; Cultural Organization.

Güven, O., Molz, F. J., & Melville, J. G. (1984). An analysis of dispersion in a stratified aquifer. *Water Resources Research*, *20*(10), 1337–1354.

Hallberg, G. R. (1987). The impacts of agricultural chemicals on ground water quality. *GeoJournal*, *15*(3), 283–295.

Hamilton, P. A., & Helsel, D. R. (1995). Effects of agriculture on ground-water quality in five regions of the united states. *Groundwater*, *33*(2), 217–226.

Harleman, D. R. F., & Rumer, R. R. (1963). Longitudinal and lateral dispersion in an isotropic porous medium. *Journal of Fluid Mechanics*, *16*(3), 385–394.

Heidari, P., & Li, L. (2014). Solute transport in low-heterogeneity sandboxes: The role of correlation length and permeability variance. *Water Resources Research*, *50*(10), 8240–8264.

Hess, K. M., Wolf, S. H., & Celia, M. A. (1992). Large-scale natural gradient tracer test in sand and gravel, cape cod, massachusetts: 3. hydraulic conductivity variability and calculated macrodispersivities. *Water Resources Research*, *28*(8), 2011–2027.

Indelman, P., & Dagan, G. (1993). Upscaling of permeability of anisotropic heterogeneous formations: 1. the general framework. *Water Resources Research*, *29*(4), 917–923.

Inoue, K., Kobi, Y., Hamada, R., Kiyono, M., & Tanaka, T. (2017). Intermediate-scale solute transport experiments for assessing the impact of correlation length and heterogeneity on macrodispersion phenomena. *Journal of Japan Society of Civil Engineers, Ser. A2 (Applied Mechanics (AM))*, *73*(2), I_85–I_96.

Inoue, K., Kurasawa, T., & Tanaka, T. (2016a). Quantification of macrodispersion in laboratory-scale heterogeneous porous formations. *International Journal of GEOMATE*, *10*(21), 1854–1861.

Inoue, K., Kurasawa, T., & Tanaka, T. (2016b). Spatial and temporal moment approaches to quantify laboratory-scale macrodispersion in stratified porous formations. *Journal of Rainwater Catchment Systems*, *22*(1), 15–22.

Inoue, K., Shimada, H., & Tanaka, T. (2011). Impact of upscaling on macrodispersion and traveltimes of solute in stratified aquifers. *Journal of Japan Society of Civil Engineers, Ser. A2 (Applied Mechanics (AM))*, *67*(2), I_521–I_532.

Ishibashi, I., & Hazarica, H. (2015). *Soil mechanics fundamentals and applications* (Second edition). CRC Press.

Jaeger, S., Ehni, M., Eberhardt, C., Rolle, M., Grathwohl, P., & Gauglitz, G. (2009). CCD camera image analysis for mapping solute concentrations in saturated porous media. *Analytical and Bioanalytical Chemistry*, *395*(6), 1867.

Jensen, J. L. (1991). Use of the geometric average for effective permeability estimation. *Mathematical Geology*, *23*(6), 833–840.

Johnson, P. T. J., Townsend, A. R., Cleveland, C. C., Glibert, P. M., Howarth, R. W., McKenzie, V. J., Rejmankova, E., & Ward, M. H. (2010). Linking environmental nutrient enrichment and disease emergence in humans and wildlife. *Ecological Applications: A Publication of the Ecological Society of America*, *20*(1), 16–29.

Klotz, D., Seiler, K. .-., Moser, H., & Neumaier, F. (1980). Dispersivity and velocity relationship from laboratory and field experiments. *Journal of Hydrology*, *45*(3), 169–184.

Kogure, T., Aoki, H., Maekado, A., & Matsukura, Y. (2005). Effect of specimen size and rock properties on the uniaxial compressive strength of ryukyu limestone. *Journal of the Japan Society of Engineering Geology*, *46*(1), 2–8.

Kurasawa, T., & Inoue, K. (2019). Effects of upscaling of physically heterogeneous porous media on solute macrodispersion phenomena. *Journal of Japan Society of Civil Engineers, Ser. A2 (Applied Mechanics (AM))*, *75*(2), I_93–I_104.

Kurasawa, T., Suzuki, M., & Inoue, K. (2020a). Effects of truncation on transport parameters estimated from spatial and temporal moments in homogeneous porous media. *Proceedings of the Seventh Asian-Pacific Symposium on Structural Reliability and Its Applications*, 283–288.

Kurasawa, T., Suzuki, M., & Inoue, K. (2020b). Experimental assessment of solute dispersion in stratified porous media. *Hydrological Research Letters*, *14*(4), 123–129.

Kurasawa, T., Suzuki, M., & Inoue, K. (2020c). Relationship between spatial distribution characteristic of hydraulic conductivity and solute dispersion for upscaled stratified porous formations. *Journal of Japan Society of Civil Engineers, Ser. A2 (Applied Mechanics (AM))*, *76*(2), I_45–I_56.

Kurasawa, T., Suzuki, M., & Inoue, K. (2021). Truncation effect on transport parameter estimation for slug tracer test in a porous medium. *Proceedings of the Thirsty-first International Ocean and Polar Engineering Conference*, 1087–1092.

Kurasawa, T., Takahashi, Y., Maeno, I., Suzuki, M., & Inoue, K. (2022). Evaluation of the darcy velocity and porosity in a ryukyu limestone aquifer. *Journal of Groundwater Hydrology*.

LeBlanc, D. R., Garabedian, S. P., Hess, K. M., Gelhar, L. W., Quadri, R. D., Stollenwerk, K. G., & Wood, W. W. (1991). Large-scale natural gradient tracer test in sand and gravel, cape cod, massachusetts: 1. experimental design and observed tracer movement. *Water Resources Research*, *27*(5), 895–910.

Levy, M., & Berkowitz, B. (2003). Measurement and analysis of non-fickian dispersion in heterogeneous porous media. *Journal of Contaminant Hydrology*, *64*(3), 203–226.

Liang, X., Zhan, H., Liu, J., Dong, G., & Zhang, Y.-K. (2018). A simple method of transport parameter estimation for slug injecting tracer tests in porous media. *Science of The Total Environment*, *644*, 1536–1546.

Luyun, R., Momii, K., & Nakagawa, K. (2009). Laboratory-scale saltwater behavior due to subsurface cutoff wall. *Journal of Hydrology*, *377*(3), 227–236.

Mackay, D. M., Freyberg, D. L., Roberts, P. V., & Cherry, J. A. (1986). A natural gradient experiment on solute transport in a sand aquifer: 1. approach and overview of plume movement. *Water Resources Research*, *22*(13), 2017–2029.

Masuoka, K., & Nakaya, S. (2021). Pore structure evaluation of quaternary highly vuggy limestone by a combination of x-ray CT images of differently sized cores. *Rock Mechanics and Rock Engineering*, *54*(4), 1919–1936.

Maurice, L. D., Atkinson, T. C., Barker, J. A., Williams, A. T., & Gallagher, A. J. (2012). The nature and distribution of flowing features in a weakly karstified porous limestone aquifer. *Journal of Hydrology*, *438-439*, 3–15.

McNeil, J. D., Oldenborger, G. A., & Schincariol, R. A. (2006). Quantitative imaging of contaminant distributions in heterogeneous porous media laboratory experiments. *Journal of Contaminant Hydrology*, *84*(1), 36–54.

Mercado, A. (1967). The spreading pattern of injected water in a permeability stratified aquifer. *IASH Publ.*, *72*, 23–36.

Miller, O., Solomon, D. K., Miège, C., Koenig, L., Forster, R., Schmerr, N., Ligtenberg, S. R. M., & Montgomery, L. (2018). Direct evidence of meltwater flow within a firn aquifer in southeast greenland. *Geophysical Research Letters*, *45*(1), 207–215.

Miyagi, N., & Komiya, Y. (2003). Effective porosity and compression strength of ryukyu limestone in pleistocene epoch in the quaternary period. *The Science Bulletin of the Faculty of Agriculture, University of the Ryukyus*, *50*, 131–135.

Montgomery, L., Miège, C., Miller, J., Scambos, T. A., Wallin, B., Miller, O., Solomon, D. K., Forster, R., & Koenig, L. (2020). Hydrologic properties of a highly permeable firn aquifer in the wilkins ice shelf, antarctica. *Geophysical Research Letters*, *47*(22), e2020GL089552.

Nakagawa, K., Amano, H., & Saito, M. (2018). Multi-level dilution test and numerical evaluation of the hydraulic parameters distribution. *Journal of Japan Society of Civil Engineers, Ser. B1 (Hydraulic Engineering)*, *74*(4), I_19–I_24.

Nakagawa, K., Saito, M., & Berndtsson, R. (2012). On the importance of hysteresis and heterogeneity in the numerical simulation of unsaturated flow. *Hydrological Research Letters*, *6*, 59–64.

Nakaya, S., Yasumoto, J., Ha, P. M., Aoki, H., Kohara, F., Masuda, H., & Masuoka, K. (2018). Hydrochemical behaviour of an underground dammed limestone aquifer in the subtropics. *Hydrological Processes*, *32*(23), 3529–3546.

Noma, Y. (1977). Groundwater in kikai-jima: Hydrogeology of the amami islands (1). *Bulletin of the Geological Survey of Japan*, *29*(3), 145–157.

Novakowski, K., Bickerton, G., Lapcevic, P., Voralek, J., & Ross, N. (2006). Measurements of groundwater velocity in discrete rock fractures. *Journal of Contaminant Hydrology*, *82*(1), 44–60.

Pickens, J. F., & Grisak, G. E. (1981). Scale-dependent dispersion in a stratified granular aquifer. *Water Resources Research*, *17*(4), 1191–1211.

Pitrak, M., Mares, S., & Kobr, M. (2007). A simple borehole dilution technique in measuring horizontal ground water flow. *Groundwater*, *45*(1), 89–92.

Poulsen, D. L., Cook, P. G., Simmons, C. T., McCallum, J. M., Noorduijn, S. L., & Dogramaci, S. (2019). A constant rate salt tracer injection method to quantify pumped flows in long-screened or open borehole wells. *Journal of Hydrology*, *574*, 408–420.

Qian, J., Wu, Y., Zhang, Y., Liu, Y., Lu, Y., & Yu, Z. (2015). Evaluating differences in transport behavior of sodium chloride and brilliant blue FCF in sand columns. *Transport in Porous Media*, *109*(3), 765–779.

Saito, H., Ohe, T., Shinyashiki, N., Yagihara, S., Umino, Y., Toida, M., Tanaka, M., Sato, M., Suzuki, T., Nagai, S., & Nishigaki, M. (2006). Stability of solid particle tracer suspended in groundwater as a marker for determining three dimensional flow

using ultrasonic reflection echo. *Journal of Nuclear Fuel Cycle and Environment*, *13*(1), 23–30.

Sánchez-Vila, X., Girardi, J. P., & Carrera, J. (1995). A synthesis of approaches to upscaling of hydraulic conductivities. *Water Resources Research*, *31*(4), 867–882.

Silliman, S. E., & Simpson, E. S. (1987). Laboratory evidence of the scale effect in dispersion of solutes in porous media. *Water Resources Research*, *23*(8), 1667–1673.

Spalding, R. F., & Exner, M. E. (1993). Occurrence of nitrate in groundwater—a review. *Journal of Environmental Quality*, *22*(3), 392–402.

Stiros, S. C. (2006). Accurate measurements with primitive instruments: The "paradox" in the qanat design. *Journal of Archaeological Science*, *33*(8), 1058–1064.

Sudicky, E. A. (1986). A natural gradient experiment on solute transport in a sand aquifer: Spatial variability of hydraulic conductivity and its role in the dispersion process. *Water Resources Research*, *22*(13), 2069–2082.

Toida, M., Tanaka, M., Sugimoto, E., Hishiya, T., Nishigaki, M., Ohe, T., Sato, M., & Komai, M. (2007). Groundwater flow estimation of the measurement area for vector seepage probe. *Journal of Groundwater Hydrology*, *49*(4), 309–326.

Uffink, G. J. M. (1990). Analysis of dispersion by the random walk method. *Doctoral Dissertation, Delft University of Technology*. Retrieved August 30, 2021, from https://repository.tudelft.nl/islandora/object/uuid%3Acef0af43-fda7-4ce4-907a-87027ccb67be

Ursino, N., Gimmi, T., & Flühler, H. (2001). Combined effects of heterogeneity, anisotropy, and saturation on steady state flow and transport: A laboratory sand tank experiment. *Water Resources Research*, *37*(2), 201–208.

Vanderborght, J., Vanclooster, M., Mallants, D., Diels, J., & Feyen, J. (1996). Determining convective lognormal solute transport parameters from resident concentration data. *Soil Science Society of America Journal*, *60*(5), 1306–1317.

van Genuchten, M. T., & Wierenga, P. J. (1977). Mass transfer studies in sorbing porous media: II. experimental evaluation with tritium (3h2o). *Soil Science Society of America Journal*, *41*(2), 272–278.

Velis, M., Conti, K. I., & Biermann, F. (2017). Groundwater and human development: Synergies and trade-offs within the context of the sustainable development goals. *Sustainability Science*, *12*(6), 1007–1017.

Wen, X.-H., & Gómez-Hernández, J. J. (1996). Upscaling hydraulic conductivities in heterogeneous media: An overview. *Journal of Hydrology*, *183*(1), ix–xxxii.

Williams, A., Bloomfield, J., Griffiths, K., & Butler, A. (2006). Characterising the vertical variations in hydraulic conductivity within the chalk aquifer. *Journal of Hydrology*, *330*(1), 53–62.

Xu, M., & Eckstein, Y. (1997). Statistical analysis of the relationships between dispersivity and other physical properties of porous media. *Hydrogeology Journal*, *5*(4), 4–20.

Yamamoto, K., Ono, F., Kanno, A., & Sekine, M. (2016). Development of the single dot type paper disk groundwater velocimeter. *Journal of Japan Society of Civil Engineers, Ser. B1 (Hydraulic Engineering)*, *72*(4), I_907–I_912.

Yang, M., Yaquian, J. A., Annable, M. D., & Jawitz, J. W. (2019). Karst conduit contribution to spring discharge and aquifer cross-sectional area. *Journal of Hydrology*, *578*, 124037.

Ye, Y., Chiogna, G., Cirpka, O. A., Grathwohl, P., & Rolle, M. (2015). Experimental evidence of helical flow in porous media. *Physical Review Letters*, *115*(19), 194502.

Yoshimoto, S., Tsuchihara, T., Ishida, S., & Imaizumi, M. (2013). Development of a numerical model for nitrates in groundwater in the reservoir area of the komesu subsurface dam, okinawa, japan. *Environmental Earth Sciences*, *70*(5), 2061–2077.

Zavala-Sanchez, V., Dentz, M., & Sanchez-Vila, X. (2009). Characterization of mixing and spreading in a bounded stratified medium. *Advances in Water Resources*, *32*(5), 635–648.

Zhang, C., Suekane, T., Minokawa, K., Hu, Y., & Patmonoaji, A. (2019). Solute transport in porous media studied by lattice boltzmann simulations at pore scale and x-ray tomography experiments. *Physical Review E*, *100*(6), 063110.

Zhang, R., Huang, K., & Xiang, J. (1994). Solute movement through homogeneous and heterogeneous soil columns. *Advances in Water Resources*, *17*(5), 317–324.

Zinn, B., Meigs, L. C., Harvey, C. F., Haggerty, R., Peplinski, W. J., & von Schwerin, C. F. (2004). Experimental visualization of solute transport and mass transfer processes in two-dimensional conductivity fields with connected regions of high conductivity. *Environmental Science & Technology*, *38*(14), 3916–3926.